2013

Analysis of microtopography, vegetation, and active-layer thickness using terrestrial LIDAR and kite photography, Barrow, AK

Julia Smith
The University of Montana

ANALYSIS OF MICROTOPOGRAPHY, VEGETATION, AND ACTIVE-LAYER THICKNESS USING TERRESTRIAL LIDAR AND KITE PHOTOGRAPHY, BARROW, AK

by

Julia J. Smith

B.A., Bowdoin College, Brunswick, Maine, 2007

Thesis

presented in partial fulfillment of the requirements
for the degree of

Master of Science
in Geography

The University of Montana
Missoula, MT

May 2013

Approved by:

Sandy Ross, Associate Dean of The Graduate School
Graduate School

Anna E. Klene, Chair
Department of Geography

Kevin McManigal
Department of Geography

Carl Seielstad
Department of Forest Management

Smith, Julia, M.S., Spring 2013 Geography

Analysis of microtopography, vegetation, and active-layer thickness using terrestrial LIDAR and kite photography, Barrow, AK

Chairperson: Anna E. Klene

Arctic regions underlain by permafrost are among the most vulnerable to impacts from climate change. This study examined changes in the active layer of permafrost near Barrow, Alaska at very fine scale to capture subtle changes related to microtopography and landcover. In 2010, terrestrial LIDAR was used to collect high-resolution elevation data for four 10 m × 10 m plots where maximum active-layer thickness (ALT) and elevation have been monitored on an annual basis since the mid-1990s and had been monitored in the 1960s as well. The raw LIDAR point cloud was analyzed and processed into four 10 cm resolution digital elevation models (DEMs). Elevation data, collected using differential global positioning system (DGPS) to assess heave and subsidence, has been gathered annually since 2004 and was used to assess the accuracy of the DEMs generated for August 2010. Higher-resolution DEMs did not have higher accuracy compared to the DGPS control points due to artifacts inherent in the LIDAR data.

The four DEMs were used to classify each plot based on microtopographical variations derived from terrain attributes including elevation, slope, and Melton's Ruggedness Number (MRN). Landcover at each plot was classified using the Visible Vegetation Index (VVI), calculated from a series of high-resolution (~10 cm) kite photographs obtained in August 2012 by researchers from the University of Texas – El Paso. The microtopography and land-cover classifications were then used to analyze ALT and elevation data from a range of years. Analysis revealed little difference in either dataset based upon microtopography and landcover. The high amount of interclass and interannual variation made it difficult to draw any conclusions about temporal trends. The results suggest that while microtopography and vegetation are important factors within the complex interaction which determines ALT, the scale of analysis made possible by the high-resolution data utilized in this study did not significantly enhance understanding of the main controlling mechanisms. While terrestrial LIDAR is excellent for many applications, particularly those with substantial vertical variability, for future research at this scale on relatively flat topography, airborne LIDAR may be more suitable.

ACKNOWLEDGEMENTS

As with any endeavor in academia, this thesis was far from a solitary effort. Many people contributed countless hours of time and invaluable knowledge to help shape and improve this project. First and foremost, I would like to thanks my adviser Anna Klene, who made use of every available connection and resource to help guide me through somewhat uncharted research territory, and then persevered to guide me through the much more familiar but still very stressful writing process.

Many research associates of the CALM initiative also helped to advance and improve this project. Thanks to Nikolay Shiklomanov for facilitating my visit to Barrow in the summer of 2011 and to Dmitry Streletskiy for assisting with the interpretation of the DGPS records. Sergio Vargas was also instrumental in providing photographs from his ongoing research. Thanks also to Marianne Okal at UNAVCO and John Gale at Overwatch for their technical expertise and guidance in LIDAR data analysis.

My thesis committee members, Kevin McManigal and Carl Seielstad, also deserve many thanks for their contributions to and facilitation of the final stages of the thesis process.

To my family and friends, thank you for encouraging me every step of the way but also knowing when to make me focus on other things in life as well.

And finally I would like to acknowledge Nancy Forman-Ebel for being such a constant, calm, and positive presence amidst all the chaos of academia – thank you for the all the smiles and encouragement, the home-grown garden vegetables, and the beautiful plant that added that little bit of brightness to my dull windowless office.

TABLE OF CONTENTS

TABLE OF FIGURES ..... **vi**

TABLE OF TABLES ..... **xi**

1 INTRODUCTION **1**

2 BACKGROUND **3**

2.1 PERMAFROST AND CLIMATE CHANGE 3

2.2 CALM MEASUREMENTS AND PROTOCOLS 5

2.3 LIDAR TECHNOLOGY 8

3 STUDY AREA **12**

4 METHODOLOGY **16**

4.1 DATA COLLECTION & PROCESSING 16

4.1.1 DGPS Data *16*
4.1.2 Active-Layer Data *19*
4.1.3 Historical Elevation Data *20*
4.1.4 Kite Photography *21*
4.1.5 LIDAR Data *23*

4.2 DEM INTERPOLATION AND ANALYSIS 29

4.2.1 Thinning the Point Clouds and DEM Generation *30*
4.2.2 Assessing DEM Accuracy *31*

4.3 MICROTOPOGRAPHY CLASSIFICATION 34

4.4 VEGETATION CLASSIFICATION 38

4.5 STATISTICAL ANALYSIS 45

5 RESULTS AND DISCUSSION **47**

5.1 LIDAR POINT CLOUD ANALYSIS 47

5.2 DEM INTERPOLATION 57

5.3 DEM ANALYSIS 62

5.3.1 Assessment with DGPS Data *62*
5.3.2 Assessment with LIDAR Control Points *68*

5.4 MICROTOPOGRAPHY CLASSIFICATION 74

5.5 VEGETATION CLASSIFICATION 81

5.6 STATISTICAL ANALYSIS 87

5.6.1 Active Layer Thickness *87*
5.6.2 DGPS *95*

6 CONCLUSIONS AND RECOMMENDATIONS **100**

6.1 TERRESTRIAL LIDAR DATA 100

6.2 ALT AND DGPS ANALYSIS 104

7 FURTHER RESEARCH OPPORTUNITIES 108
7.1 HISTORICAL ELEVATION DATA 108
7.2 OTHER LIDAR-BASED INITIATIVES 109
7.3 RADAR-BASED INITIATIVES 113
REFERENCES 114

TABLE OF FIGURES

Figure 1. Frost action manifested as patterned ground, presented as both low-centered (upper-left) and high-centered ice wedge polygons (Photo: Sergio Vargas). 4

Figure 2. Distribution of CALM monitoring sites in the Northern Hemisphere (Reproduced from http://www.udel.edu/Geography/calm/about/map.html). 6

Figure 3. Multiple LIDAR returns generated as a result of the various layers of vegetation between the laser source and the ground (Reprinted from Lefsky et al. 2002)..8

Figure 4. Map of the study site, the UIC-NARL research complex, and the Barrow Environmental Observatory near Barrow, AK. 12

Figure 5. Locations of CALM sites (ARCSS 1 km^2 grid [U1] and CRREL plots [U2]) looking south from the Chukchi Sea, with the Air Force Radar site in the foreground (Photo: Nikolay Shiklomanov). 12

Figure 6. Overview of the study area showing the four CRREL plots analyzed in this study in relation to the entire CRREL transect, the 1 km^2 ARCSS grid, and general landscape features (Original illustration from Nelson et al. 1998). 13

Figure 7. Aerial photograph of the study area overlain by the individual LIDAR scan sites and positions of the LIDAR targets used for georeferencing in the context of other research initiatives including the CALM active-layer measurements and DGPS sites. 14

Figure 8. Aerial photo showing the locations of annual DGPS measurements in the study area. Points labeled "FB" indicate frost boils. 17

Figure 9. Sampling design employed by CALM researchers to monitor active-layer thickness at each CRREL plot. 19

Figure 10. Wooden posts marking the exterior nodes of the ALT sampling grid at CRREL Plot 44 (Photo: Nikolay Shiklomanov). 19

Figure 11. Sergio Vargas and the kite used to collect high-resolution aerial imagery of the study area, August of 2012 (Photo: Kelsey Nyland). 21

Figure 12. Georeferenced high-resolution kite photograph of the entire study area, overlain with cropped and independently georeferenced images of the individual study plots. 22

Figure 13. Terrestrial LIDAR system used to collect data at the study sites, August 2010 (Photo: Marianne Okal). 23

Figure 14. Detail map showing the loss of accuracy which could be caused by rounding during data projection. Original data points are shown in green; red points represent the same dataset rounded to two decimal places in UTM coordinates. 25

Figure 15. Individual scans merged together to display the entire raw LIDAR dataset, rendered using RGB values. 26

Figure 16. Last returns from plot C34, colored using elevation. The streaking pattern in the first returns is also visible in the last returns, most noticeably on the tops of the ice-wedge polygons (left side of image). 28

Figure 17. High resolution (2.4 m multispectral, pan-sharpened to 0.7 m resolution) land-cover image derived from Quickbird satellite imagery collected on August 1, 2002. Data provided by NCAR/EOL under sponsorship of the National Science Foundation: http://data.eol.ucar.edu. 39

Figure 18. Calculation of the VVI for plot C34. Three visible bands make up the original image, of which individual bands were used in the calculation of the VVI and other indices. The original aerial image and DEM are shown for reference. 43

Figure 19. Photographs of the four study plots, August 2012. Each photograph was taken from the northeastern corner of the plot, facing southwest. Photos: Nikolay Shiklomanov. 44

Figure 20. Point density of the entire original LIDAR point cloud, expressed as number of points per 10 cm^2. Study plots are demarcated with dashed lines with black dots representing the locations of DGPS measurements. Point density decreases dramatically within 20 m of the scanner. 50

Figure 21. Point density maps of each of the four study plots. Density is expressed as number of points per 10 cm^2. The highest point density recorded in the plots was 5,305 points/10 cm2. Inset diagrams show the relative locations of the scanner around each plot. Point density noticeably decreased with increasing distance from the scanner. 53

Figure 22. Point density maps of each of the four study plots. Density is expressed as number of points per 1 cm^2. The highest point density recorded in the plots was 522 points/cm^2. Flagging due to obstruction by the wooden posts used to demarcate the active layer sapling grid (Figure 10) can be seen to some degree in all plots at this resolution. Inset diagrams show the relative locations of the scanner around each plot. .54

Figure 23. LIDAR intensity maps for each of the four study plots. Uncalibrated values ranged from a minimum of 0 (C34) to a maximum of 4,277 (C40). Intensity generally decreased with increased distance from the scanner. Inset diagrams show the relative locations of the scanner around each plot. 56

Figure 24. DEMs for plot C34 generated from point clouds thinned out to resolutions of 1, 2, 5, and 10 cm. Thinned point clouds were made by taking the lowest point in each grid cell of specified size. Steaks in the LIDAR data manifested as small ridges on the DEM can be seen clearly in the 1, 2, and 5 cm DEMs and to a lesser extent in the 10 cm DEM, where they appear somewhat smoothed out. Inset diagrams show scanner positions 58

Figure 25. Elevation profile graphs for a variety of transects in plot C34. Profile graphs revealed that small ridges resulting from streaks in the original data were 2-5 cm and did not vary in magnitude between the polygon centers and troughs, even though vegetation is both denser and taller in the troughs. 59

Figure 26. Raised, unvegetated frost boil, typical in appearance to those scattered throughout the study area (Photo: Anna Klene). 60

Figure 27. Elevation profile graphs comparing vegetated areas to unvegetated frost boils overlain on the aerial imagery of plots 34 and 37. Streaks in the data manifested as ridges on the DEMs were not affected by the presence or absence of vegetation, presenting in the same patterns (~2-5 cm in height) on both vegetated and unvegetated ground. 61

Figure 28. Final digital elevation models (DEMs) for each of the four study plots using color ramps stretched over the range of elevations within each plot. 65

Figure 29. DEMs for each study plot, symbolized first based only on the range of values present in the individual plot and second based upon the entire range of values between all four plots. Most of the microtopographical relief in plot C34 (the lowest) and C44 (the highest) is lost in the second symbolization due to overall elevation differences. Aerial photos of each plot are shown for reference. 66

Figure 30. Comparison of the accuracy of the both the LIDAR point cloud data and the derived DEM using in situ DGPS data as ground truth. All elevations are given as height above ellipsoid (HAE) in meters 67

Figure 31. Scatterplots comparing the interpolated heights of the DEMs to the actual heights of the withheld LIDAR control points for each plot, showing strong correlation between the two datasets. All values represent heights above ellipsoid in meters. 70

Figure 32. Residual maps for each of the four plots. Red points represent locations where the heights of the original LIDAR data were below those of the interpolated DEM; green points represent locations where the LIDAR heights were above those of the DEM. Average residual values for all plots were less than 0.1 cm. 72

Figure 33. Simplified residual maps for each plot, showing only those points where residual values were greater than 1 cm (in red) 73

Figure 34. Surface derivative maps for plot C34. Red areas indicate higher values where there is greater variation in terrain surface. The aerial photo and DEM for plot C34 are provided for reference. Input specifications, including resolution and cell neighborhood size, used to create each map can be found in Table 3. 75

Figure 35. Topographic index maps for plot C34. Red areas indicate higher values where there is greater variation in terrain surface. Input specifications, including optimal resolution and cell neighborhood size, used to create each map can be found in Table 3.76

Figure 36. Maps of the final terrain calculations used in the microtopographical classification of the DEMs. The calculated layers for each plot are all symbolized with the same color ramp stretched to the same values in order to facilitate accurate visual comparison between plots.....78

Figure 37. Construction of the binary maps used in the final microtopography classification of the DEMs for each plot. Break values were determined using both the DEM and aerial imagery as ground truth.....79

Figure 38. Final classification steps to produce the microtopography classification maps for each plot. Final maps were divided into three classes: troughs, sides, and centers. ...80

Figure 39. Vegetation index maps for plot C34. Aerial imagery of the site is provided for reference. The most informative index (the VVI) is shown in the upper-right.....82

Figure 40. Maps of the three experimental vegetation classifications derived from the VVI for each study site. Legends indicate how many of the 144 ALT monitoring plots were represented by each class. Frost boils were classified on all maps, but none of the ALT monitoring plots fell within that category. Black boxes on each map represent the boundaries of each plot. The final classification used in analysis was the “4 Classes”, which contained one class for frost boils and three for vegetation types. 83

Figure 41. Box-and-whisker plots of active-layer thickness based upon each of the three experimental vegetation classifications. The final classification defined wet, mesic, and dry categories.....84

Figure 42. Maps of the final microtopographic and vegetation classifications as well as the aerial imagery for each study plot.....85

Figure 43. Illustration of the clipping operation used to classify the 144 ALT and 18 DGPS sites within the four study plots. Polygons used to clip ALT sites (shown in Figure 10) were ~30 cm (12 in) diameter circles to represent the sampling radius, and polygons used to clip the DGPS sites were ~5 cm diameter circles to account for the size of the target and rover antennae. Clipped areas that contained more than one class were classified based on whatever class occupied the majority of the area. 86

Figure 44. Box-and-whisker plot for ALT based upon microtopography class. Lines represent the general trend from 1962-2012, with the two breaks in the x-axis and trend lines signifying the lack of available data for the years 1967-1991 and 1994-1996. 91

Figure 45. Box-and-whisker plot for ALT based upon vegetation class. Lines represent the general trend from 1962-2012 with the two breaks in the x-axis and trend lines signifying the lack of available data for the years 1967-1991 and 1994-1996. 94

Figure 46. Scatterplot of DGPS measured heights from 2003-2012 grouped by plot. Lines indicate the general 10-year trend of subsidence at each plot. 95

Figure 47. Scatterplot of DGPS measured heights from 2003-2012 grouped by microtopography class. Lines indicate the general 10-year trend of subsidence for each class. 97

Figure 48. Scatterplot of DGPS measured heights from 2003-2012 grouped by vegetation class. Lines indicate the general 10-year trend of subsidence for each class..99

Figure 49. Experimental elevation diagrams for plot C34, comparing elevations recorded in the 1960s (upper-left) to those in 2010 (upper-right). Elevations for 2010 were calculated from the DEM heights using the GEOID99 conversion model. Due to an undocumented datum in the early data, absolute values for change could not be determined, but the bottom diagram reflects the relative amount of change between two dates (areas in red represent the most change). 109

Figure 50. Terrestrial LIDAR point cloud from summer 2011 collection, ~2 km south of the CRREL sites. Points are rendered by RGB value but not projected or classified. ...110

Figure 51. High-resolution DEM and hillshade generated from airborne LIDAR scans of an area ~2 km S-SW of the CRREL sites. Data was acquired by AeroMetric on October 4, 2005. The horizontal and vertical accuracies of the DEM are 0.30 m and 0.15 m, respectively. The small scale inset map shows the location of the aerial DEM coverage relative to the site of the 2010 terrestrial LIDAR acquisition (CRREL plots). The larger scale inset map shows the locations of the 2011 terrestrial LIDAR acquisition control points, as well as the landscape detail captured in the aerial LIDAR DEM. Data provided by NCAR/EOL under sponsorship of the National Science Foundation: http://data.eol.ucar.edu. 112

TABLE OF TABLES

Table 1. Summary of the LIDAR files defining the four CRREL plots. 27

Table 2. Descriptive statistics of LIDAR and DEM elevations and summary of errors (DEM-LIDAR) for plot C34 using four different methods of withholding points from the LIDAR datasets. Units are cm above ellipsoid. Residuals – max is the absolute value of the maximum residual of the dataset. 33

Table 3. Terrain calculations and corresponding input specifications. 36

Table 4. Vegetation indices which can be calculated using bands in visible wavelengths showing equations and corresponding raster calculations. 41

Table 5. LIDAR points contained within a 20 cm^2 circular area clipped from raw point cloud at each DGPS location. The clipped area represents the space occupied by the DGPS target and receiver. Units are cm above ellipsoid. 48

Table 6. Residual statistics between the DGPS sites and the LIDAR point cloud. Units are cm above ellipsoid. 49

Table 7. Frost boil sites clipped from LIDAR point cloud. Units are cm above ellipsoid.51

Table 8. Differences between DGPS height measurements and LIDAR-derived DEM elevations, (DGPS-DEM) expressed as Mean Bias Error (MBE) and Mean Absolute Error (MAE). The DEM-generation software and tool is indicated: LAStools® blast2dem, LIDAR Analyst® LAS file to Raster with Filtering, and LIDAR Analyst® Extract Bare Earth All values are cm above ellipsoid. 63

Table 9. Differences as in Table 8, but for the remaining 16 DGPS points after the 2 outliers were removed. 63

Table 10. Summary of the original AOI point clouds and the 10 cm-resolution thinned point clouds used to derive the best performing DEMs. 67

Table 11. Summary statistics for the comparison of DEM elevations to DGPS measurements. All units are cm above ellipsoid. 68

Table 12. Summary statistics comparing the lowest LIDAR point within each 50 cm cell to the DEM elevations (LIDAR-DEM). All units are cm above ellipsoid. 69

Table 13. Number of observations and percentages of the ALT and DGPS measurement points located within each microtopography and vegetation category. 87

Table 14. Summary statistics by plot of ALT for 2010 and 2003-2012. 88

Table 15. Descriptive statistics for 2010 active layer thickness, based upon microtopography classes. 88

Table 16. Descriptive statistics for 2010 active-layer thickness, based upon vegetation class. 89

Table 17. Comparison of descriptive statistics for 2010, 2003-2012 and 1962-1966 ALT based upon microtopography classifications. 90

Table 18. Rate of increase in ALT for each microtopography class. 92

Table 19. Comparison of descriptive statistics for 2010, 2003-2012 and 1962-1966 ALT based upon vegetation classifications. 92

Table 20. Rate of increase in ALT for each vegetation class. 95

Table 21. Summary of linear regressions for DGPS points by plot. 96

Table 22. Summary of linear regressions for DGPS points by microtopography class. ..98

Table 23. Summary of linear regressions for DGPS points by vegetation class. 99

1 INTRODUCTION

Polar regions are expected to be among the first environments to respond to climate change and to have some of the most dramatic impacts. In the past few decades, mean Arctic temperatures have risen at nearly twice the rate of those in the rest of the world (ACIA, 2004), resulting in the widespread melting of glaciers and sea ice. A major concern is the effect that climate change will have on areas of perennially frozen ground (permafrost) which have gradually decreased in geographical extent over the last few decades (Brown et al. 2000). Recent climate models indicate that areas of permafrost will continue to decrease in volume and extent and that the thickness of the active layer (the layer above permafrost which freezes and thaws annually) in these regions will increase (Brown et al. 2000). The threat of increasing permafrost degradation on a global scale presents a number of scenarios including the migration of forests poleward, destabilization of buildings, roads, and other infrastructure constructed on permafrost soils, exacerbation of coastal erosion, major shifts in hydrological regimes, as well as the mobilization of contaminants and carbon previous confined to the permafrost layer (Hassol 2004). It is important to understand the response of permafrost landscapes to these environmental changes in order to better predict and plan for regional shifts that may occur.

Complex interactions of variables influence the freezing and thawing processes of permafrost, and these interactions are often manifested at very fine scales on the landscape. Previous studies of permafrost microtopographic processes have been limited in the scale at which they can observe changes by the speed and reliability of their methods and the accuracy of their equipment. However, as technology advances,

researchers are able to study these interactions on increasingly finer spatial and temporal scales with greatly improved accuracy.

This project involved two phases, 1) construction and evaluation of high-resolution DEMs from terrestrial LIDAR point clouds, and 2) use of those DEMs, in conjunction with high-resolution kite photography, to examine time-series data of active-layer thickness and elevation by microtopographic and land-cover categories at four plots near Barrow, Alaska. The raw LIDAR data obtained in August 2010 was used to generate four high-resolution digital elevation models (DEMs) that were evaluated for accuracy using filtered reference data and DGPS data collected in the field in August 2010 as ground truth and part of on-going annual monitoring. In an attempt to detect changes in the permafrost landscape at very fine (cm) scales, the 2010 DEMs were then used to classify the landscape based on variations in microtopography. These classifications were used in conjunction with land-cover categorizations derived from high-resolution aerial kite photography (obtained in August 2012 by researchers at the University of Texas – El Paso) to qualitatively and quantitatively describe spatial and temporal differences in time-series data of active layer thickness (ALT) and DGPS-based elevations across the local permafrost landscape.

2 BACKGROUND

2.1 Permafrost and Climate Change

Permafrost is generally defined as ground material that remains below 0°C for at least two years (Muller 1947). Permafrost can be described as consisting of three layers: the active layer, the transient layer, and the permafrost layer (Shur 1988). The permafrost layer consists of perennially frozen ground, while the transient layer is characterized by "high and quasi-uniform ice content" that freezes and thaws at decadal to century scales, thus providing a sort of "thermal inertia" which helps to insulate the permafrost from the thawing active layer (Streletskiy 2010). The active layer is defined as "the top layer of ground subject to annual thawing and freezing in areas underlain by permafrost" (Harris et al. 1988). This layer, influenced by surface temperature, surface cover, substrate, soil moisture, and snow cover, is important in arctic ecosystems because it is the site of nearly all ecological, hydrological, and biogeochemical activity (Brown et al. 2000). In light of climate change, scientists are increasing scrutinizing the role that permafrost plays in global carbon cycling. There is a large amount of carbon and methane stored in permafrost that is not presently involved in the carbon cycle (Schuur & Abbott 2011). If the active layer continues to thaw deeper into the perennial permafrost, the organic soils once trapped in the frozen ground will be available for decomposition, resulting in a positive feedback cycle in arctic regions shift from an atmospheric carbon sink into a carbon source (Schuur & Abbott 2011).

While permafrost by definition does not necessarily contain ice, when sub-surface ice is present, it occurs in many forms including "nearly-vertical ice wedges, lenses, irregular masses, small grains and crystals, irregular particles, stringer, and films on the soil particles" (Hussey et al. 1966). Certain permafrost areas are considered ice-rich, meaning that the ground is supersaturated with ice. Such landscapes are characterized by the presence of a number of distinctive landforms, produced as a result of frost action (Washburn 1973). Some of the most striking and common of these landforms are ice-wedge polygons (Figure 1), which arise as a result of the current or past presence of ice wedges beneath the ground surface. Ice wedges form when water and snow collect in cracks that form from contraction of the ground during extreme low winter temperatures (Hussey et al. 1966). The water and snow inside the cracks subsequently freezes, and the ice wedge gradually grows downward and in width over time as cracks deepen and reform year after year (Hussey et al. 1966).

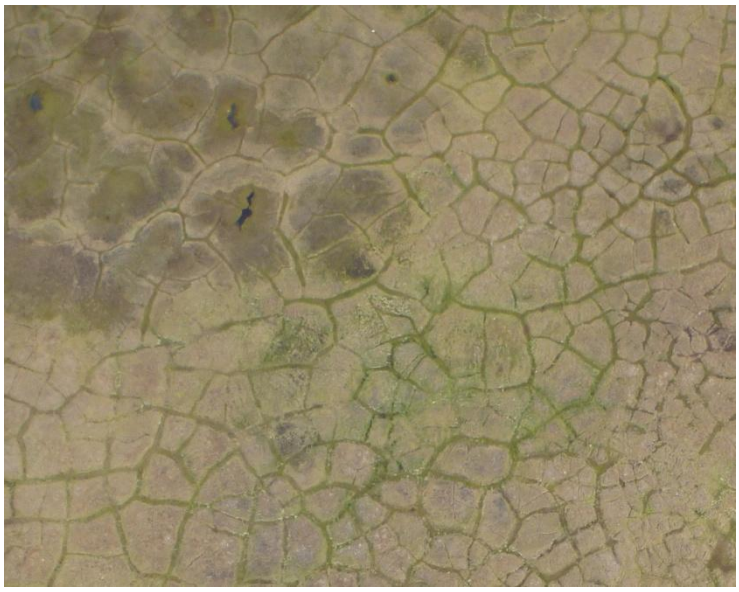

Figure 1. Frost action manifested as patterned ground, presented as both low-centered (upper-left) and high-centered ice wedge polygons (Photo: Sergio Vargas).

While ice-wedges and other fine-scale cryological processes are often responsible for microtopographical variations in thermokarst landscapes, there are other processes that can cause small amounts of vertical displacement over significantly larger horizontal

scales. During the winter, when moist ground is subject to extreme freezing, heaving of the ground surface may occur as a result of ice lens formation, a process commonly referred to as *frost heave* (Harris et al. 1986). When the temperature increases again in spring, the ice starts melting, the soil becomes soft and saturated, and as a result soil strength decreases and the ground surface subsides, a process referred to as *thaw weakening* (Harris et al. 1986). Over time, steady ground subsidence may result from thawing (and subsequent run-off) of ice within the active layer, particularly of ground ice in the transient layer near the permafrost table (Shiklomanov et al. 2010). Interferometric Synthetic Aperture Radar (InSAR) processing has been used to detect annual subsidence rates on the scale of 2-7 mm on the North Slope of Alaska across large regions (Wahr et al. 2008). This kind of gradual ground-surface deformation has drastic implications for structural engineering projects in arctic environments, as well as for regional ecological and hydrological regimes (Brown et al. 2000).

2.2 CALM Measurements and Protocols

As evidence of climate change grows, monitoring changes in Arctic regions has become increasingly important. To observe and record the response of the active layer and near-surface permafrost to climate change over time, the Circumpolar Active Layer Monitoring (CALM) program was initiated in 1998, funded by the Arctic System Science (ARCSS) Program of the National Science Foundation (NSF; Brown et al. 2000). CALM currently monitors Arctic and alpine permafrost at over 260 sites in 14 participating countries spanning both the northern and southern hemispheres (Figure 2; Shiklomanov et al. 2011). The minimum observation required under CALM protocol is a late-season mechanical probing of the thickness of the active layer, which is

accomplished by inserting a 1-cm diameter steel rod into the soil to the "depth of resistance" (Brown et al. 2000). The active layer typically reaches its maximum thickness and begins freezing upward from the bottom one to two weeks before the air temperature cools sufficiently to allow freezing from the surface (Romanovsky & Osterkamp 1997). In order to maintain interannual consistency, active-layer thicknesses are recorded as close to the time of maximum thaw as can be arranged (Shiklomanov et al. 2010). It is recommended that thermal measurements are also taken to confirm the depth and timing of maximum active layer thickness.

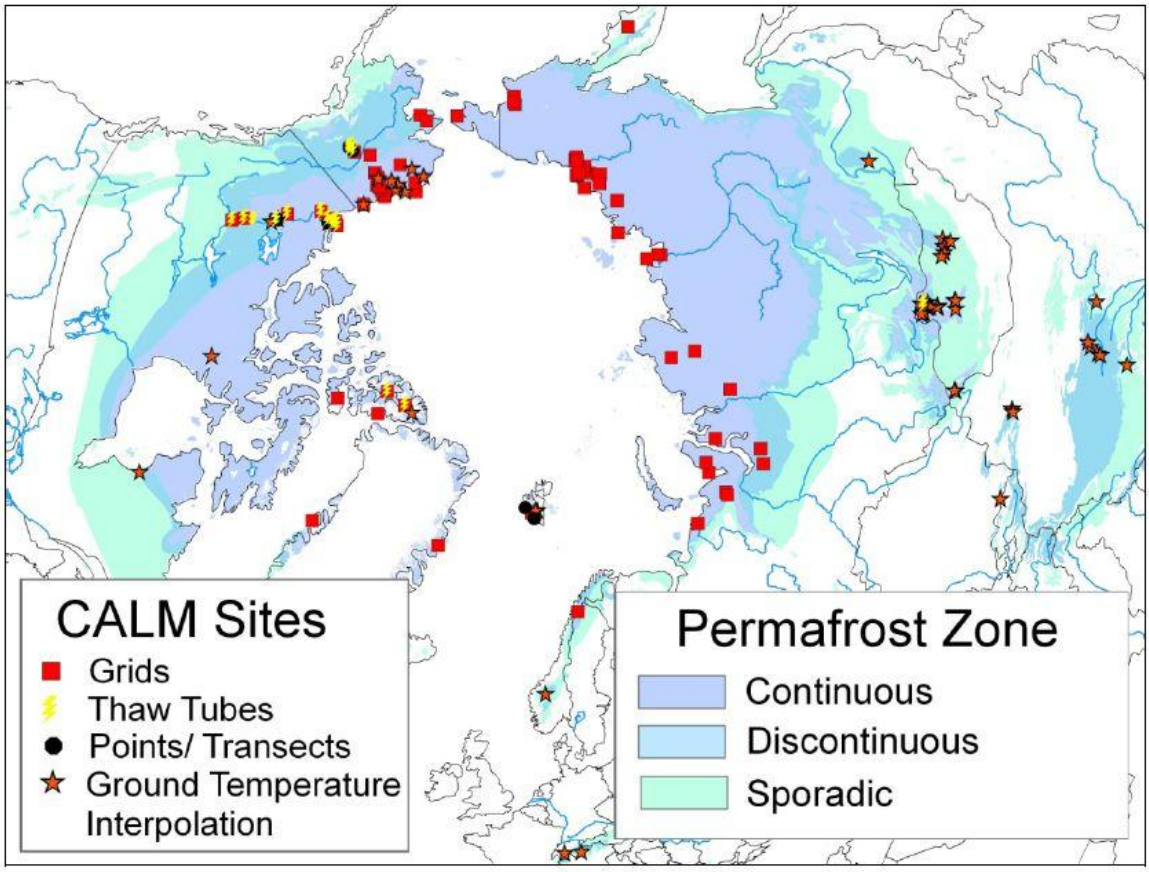

Figure 2. Distribution of CALM monitoring sites in the Northern Hemisphere (Reproduced from http://www.udel.edu/Geography/calm/about/map.html).

While manual probing is a widely-accepted method to measure active-layer thickness, it is not capable of measuring ground displacement or long-term net subsidence (Shiklomanov et al. 2010). Therefore, frost heave and thaw subsidence are monitored at some sites using either standard manual surveying techniques or a high-precision (~1 cm) differential global positioning system (DGPS). Traditional survey methods, which include optical leveling or triangulation through the use of statia rods, chaining pins, magnetic probes, or expanded-foot anchor pins, can be useful for gathering centimeter-accurate data over an extensive area; however, these techniques all require line-of-sight to frost-defended reference markers (benchmarks), which are difficult to install and usually not established precisely in geodetic coordinate systems (Little et al. 2003). The DGPS method involves the use of two satellite receivers: a base receiver at a precisely known location for use as a reference station, and a roving receiver that is taken into the field. While the use of frost-defended benchmarks is still necessary for the calibration of the base receiver, the rover receiver relies on the base and satellite positioning, and can be used kilometers away where there are no pre-existing physical reference points or benchmarks, thus dramatically extending the range of surveying. Unfortunately, the DGPS method is still time-intensive because in order to achieve such high horizontal and vertical accuracies, DGPS requires simultaneous communication with a base receiver and four or more satellites. As a result, a single point can take anywhere from 10 minutes up to 1 hour to sufficiently calibrate (Little et al. 2003). Due to the time- and labor-intensive sampling techniques, researchers are investigating the possibility of incorporating remote-sensing techniques to help monitor surface topography as well as other environmental characteristics of the active layer.

2.3 LIDAR technology

LIDAR (LIght Detection And Ranging, or laser altimetry; Burtch 2002) is one remote sensing tool that is swiftly gaining popularity for use in ecological and environmental monitoring studies. Although the technology has been utilized for scientific observation since the 1980's, it was not until the mid-1990's that LIDAR data became widely available, and in the short time since then the technology has improved significantly in both accuracy and data density (Vosselmar & Maas 2010). LIDAR is a remote sensing technology that uses laser signals to discern distance by emitting light (waves or pulses) at a target object and calculating the time it takes for the light to be reflected back (Burtch 2002). LIDAR typically uses a combination of instruments for locating the target surface in three dimensional space, including Global Positioning System (GPS) receivers to obtain position, angle encoders for orientation of scanning mirrors, and Intertial Navigational Systems (INS) to measure the altitude of the LIDAR sensor (roll, pitch, yaw) in cases where the sensor is airborne or mounted on a vehicle (Lefsky et al. 2002). The rate at which LIDAR systems emit signals is typically measured in kHz, or the number of individual pulses emitted per second, in thousands of pulses (Burtch 2002). Some LIDAR systems now have pulse rates beyond 300 kHz, equivalent to 300,000 pulses per second (Dailey 2008), producing enormous, high density

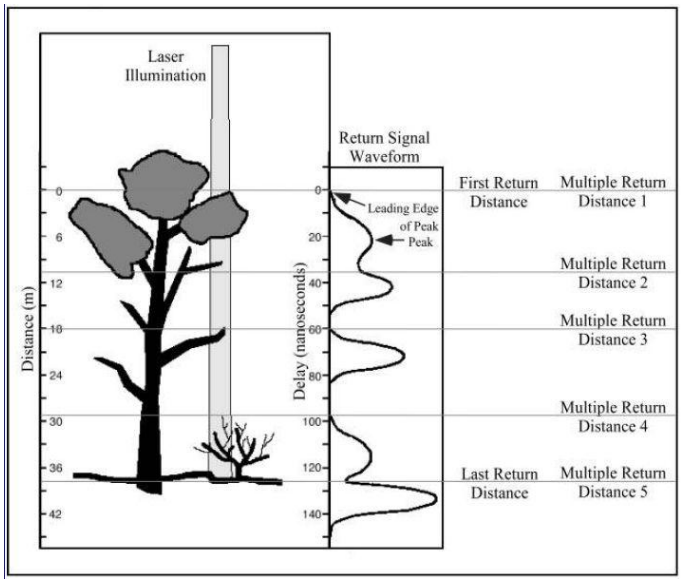

Figure 3. Multiple LIDAR returns generated as a result of the various layers of vegetation between the laser source and the ground (Reprinted from Lefsky et al. 2002).

datasets. Individual laser signals can yield multiple return pulses if they encounter intermediary surfaces before reaching the ground (Figure 3). Discrete return LIDAR can record these multiple measurements through the use of a reflected signal strength threshold, beyond which the sensor will record another measurement for the same point (Evans et al. 2009).

LIDAR data can be collected in one of two ways: airborne, where the scanner is mounted on an aircraft or satellite, or terrestrial, where the scanner is either stationary on the ground or attached to a moving vehicle. Both aerial and terrestrial LIDAR are capable of recording multiple returns and producing dense, three-dimensional data point clouds. Aerial LIDAR produces fairly uniform point clouds with regular post spacing as a result of constant aircraft and laser scanner speed. Point clouds from terrestrial-based LIDAR, on the other hand, tend to be denser but less uniform as they are created from multiple laser beams scanning at different angles which are then merged into one dataset with a common reference system (Bonaffe et al. 2007). In a point cloud generated by terrestrial LIDAR, point density is the highest closest to the scanners and decreases dramatically with distance. Point cloud data can be useful for studying vegetation layers and canopy cover (Hofton et al. 2002), but many LIDAR users are only interested in the final return points that can be used for the generation of high resolution DEMs of the ground surface. In order to generate a true ground-surface DEM from the point cloud, ground returns points must be separated from non-ground returns through the application of a classification or filtering model (Evans et al. 2009). Once all non-ground points are removed, interpolation techniques can be applied to the remaining points to generate a "bare earth" surface. Because of the high density of point-cloud data, LIDAR DEMs are

among the most accurate topographic datasets available, able to achieve horizontal and vertical accuracies on the scale of centimeters (Arnold et al. 2006).

The availability and use of LIDAR is increasing quickly. Glaciologists currently use LIDAR to generate high-resolution DEMs for energy balance and ice-flow modeling purposes (Arnold et al. 2006). Many glaciologists believe with the increase in pulse frequency and positional accuracy of LIDAR systems, they now possess greater potential for glacial monitoring than any other remote sensing methods including stereo-photogrammetry and synthetic aperture radar (SAR) interferometry (Arnold et al. 2006). LIDAR has also become increasingly useful in forestry mapping because it requires "only one opening through a tree canopy to 'see' the ground, whereas photogrammetry requires that the same ground point be visible from two exposure stations" (Burtch 2002). Uses have also been found for LIDAR in mining surveys, civil engineering, and geological outcrop studies (Bonnaffe et al. 2007). Planning is underway for complete nation-wide LIDAR acquisition in the United States to improve the current National Elevation Dataset (NED) and provide other LIDAR-derived products to a variety of users (Evans et al. 2009).

High-resolution DEMs are being used to inform ecological and geomorphological research at increasingly finer scales. Topography often exerts a strong influence over the structure, composition, and function of ecological systems across a range of scales (Lefsky et al. 2002). In permafrost areas, vertical variations occur both spatially (manifested as patterned ground; Peterson 1999), and temporally (as observed with annual frost heave and gradual thaw subsidence; Zhu 2006). Ice-rich permafrost environments are characterized by a high degree of microtopographical variation, where

vertical changes on the sub-centimeter scale can have pronounced effects on microclimate and hydrological regimes (Brown & Johnson 1965). These small topographical changes can create significant variation in vegetation species composition, near-surface soil moisture, and depth to the permafrost (Engstrom et al. 2005; Olivas et al. 2011). In the context of Arctic climate change, it has been shown that microtopography can cause variations in temperature and water availability that can result in "considerable differences in CO_2 sink activity of the polygonal tundra" (Olivas et al. 2011). Studying and mapping these topographical variations at the finest scale possible is essential for building a more comprehensive understanding of environmental process and climate change in the Arctic.

3 STUDY AREA

The four plots analyzed in this study are located (general area: 17°18'28"N, 156°35'17") about 7.5 km east-north east of the village of Barrow, Alaska, near the northernmost point in the United States. The Barrow area is underlain by nearly continuous permafrost, which can reach depths of more than 400 m (Sellmann et al, 1975). The surrounding coastal plain is scattered with oriented thaw lakes, drained lake basins, and ice-wedge polygons and is characterized by low elevation (0-20 m) and very little relief (Sellmann et al, 1975). Barrow has been a hub for arctic and permafrost-related research since the opening of the Naval Arctic Research Laboratory (NARL) in 1940 (Norton 2001).

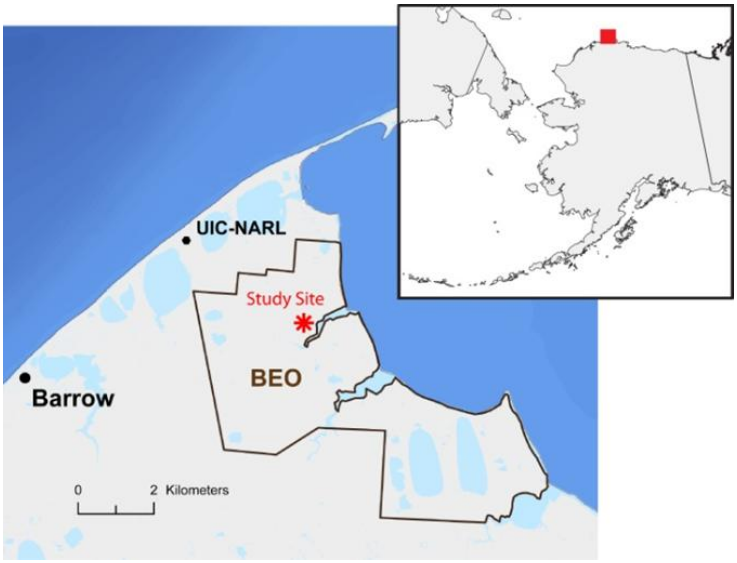

Figure 4. Map of the study site, the UIC-NARL research complex, and the Barrow Environmental Observatory near Barrow, AK.

Figure 5. Locations of CALM sites (ARCSS 1 km^2 grid [U1] and CRREL plots [U2]) looking south from the Chukchi Sea, with the Air Force Radar site in the foreground (Photo: Nikolay Shiklomanov).

The study plots are located within the Barrow Environmental Observatory (BEO; Figure 4), a 7,500 acre research reserve created in 1992 on land owned by the Ukpeaġvik Iñupiat Corporation (Norton 2001). The BEO contains a 1 km^2 ARCSS/CALM monitoring grid (U1), established in the early 1990's as well as a transect implemented by the U.S. Army Cold Regions Research Laboratory (CRREL) that was first monitored in the 1960's (U2; Figure 5; Brown & Johnson 1965). Monitoring was resumed at the CRREL plots in the early 1990's, and both the CRREL and ARCSS sites are currently monitored on an annual basis for active-layer thickness among other environmental variables. Figure 6 shows the locations of these research sites relative to local landscape features, including the drained lake basin (Central marsh) to the west, the north-south

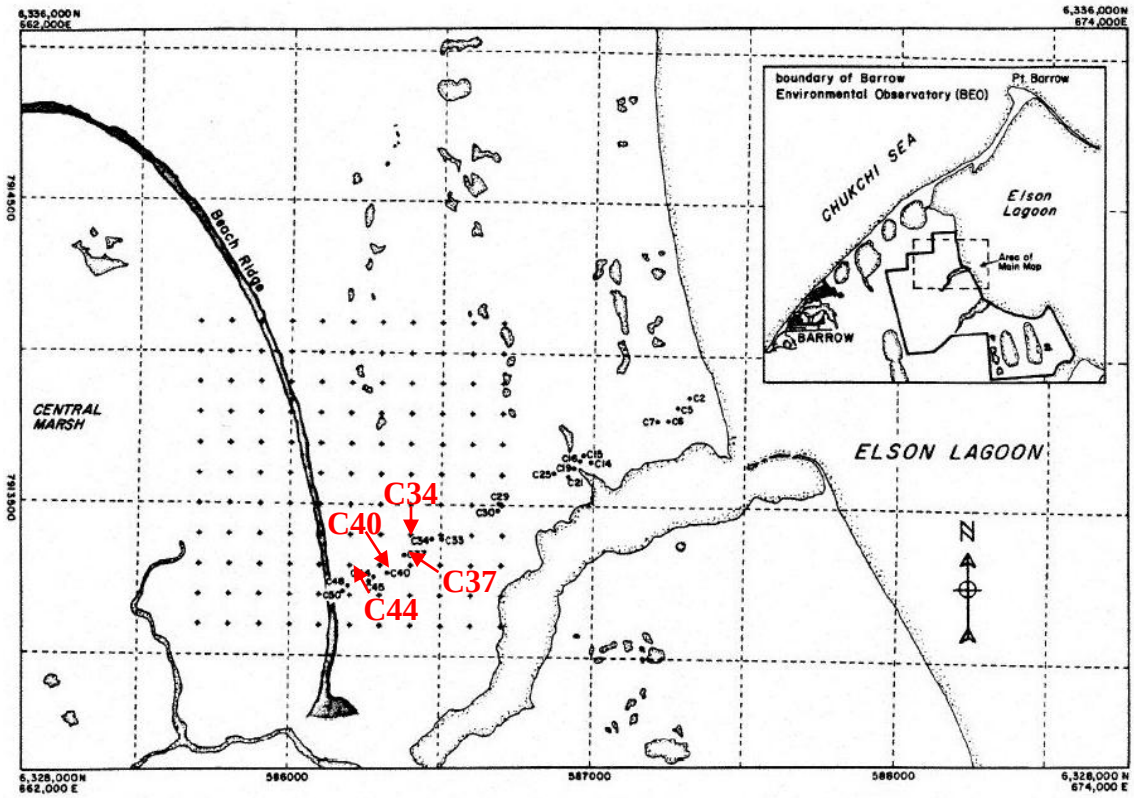

Figure 6. Overview of the study area showing the four CRREL plots analyzed in this study in relation to the entire CRREL transect, the 1 km^2 ARCSS grid, and general landscape features (Original illustration from Nelson et al. 1998).

oriented beach ridge that cuts through the ARCSS grid and the western-most CRREL plots, and Elson Lagoon to the east (Nelson et al. 1998).

The LIDAR scan sites were located in the southern portion of the ARCSS/CALM grid on four plots within the CRREL transect (C34, C37, C40, and C44, labeled in Figure 6). A more detailed aerial photograph of the study area can be found in Figure 7, which also shows the locations of the 36 points where active-layer monitoring measurements are taken within each CRREL plot, as well as the locations of DGPS sites annually.

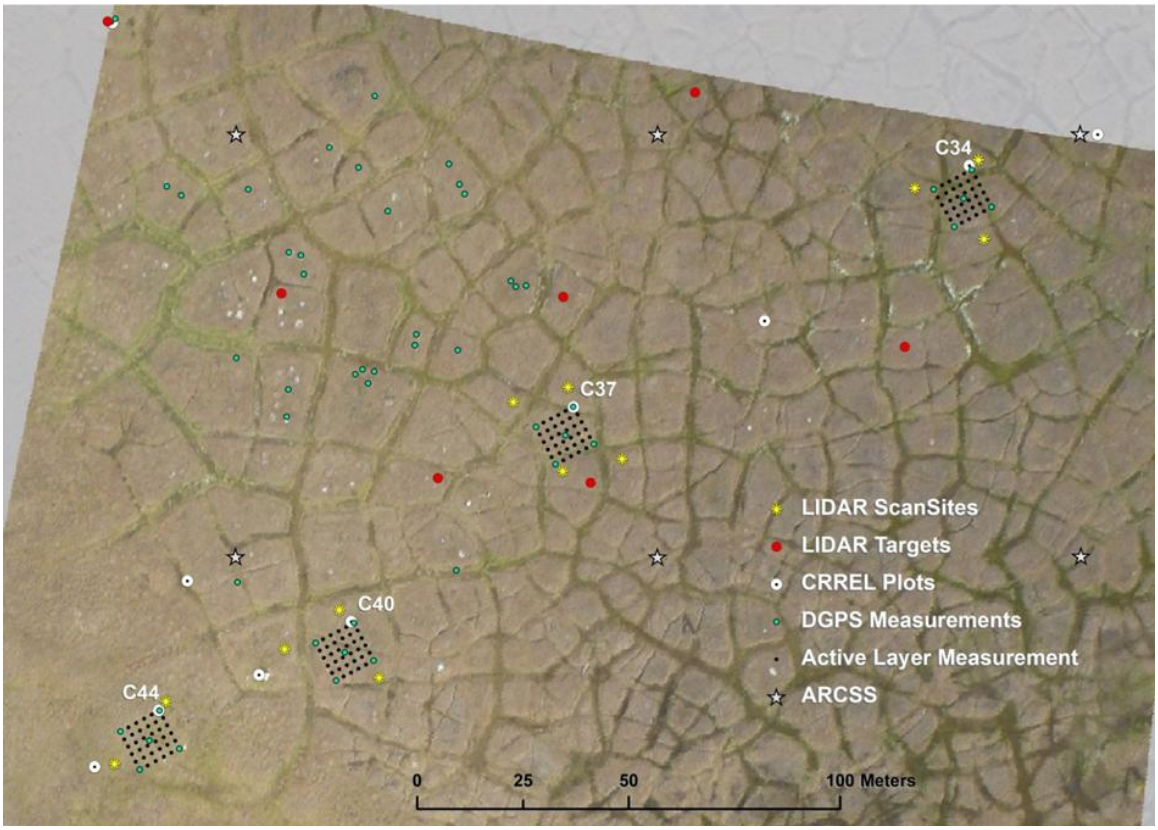

Figure 7. Aerial photograph of the study area overlain by the individual LIDAR scan sites and positions of the LIDAR targets used for georeferencing in the context of other research initiatives including the CALM active-layer measurements and DGPS sites.

The general area is characterized as "polygonized upland [relative to the central marsh] occupied by moist acidic tundra, with …high-centered ice wedge polygons [that] developed in response to thermo-mechanical incision by streams draining to Elson

Lagoon" (Hinkel & Nelson 2003). The landscape is dominated by wet sedge meadows with more than half the vegetation cover made up of vascular plants (Nelson et al. 1998; Brown & Johnson 1965). Local relief across the entire area is only ~1 m, with seasonal flow during summer months confined to the ice-wedge troughs maintaining and furthering the microtopography (Hinkel & Nelson 2003).

One prominent small-scale thermokarst feature scattered across the study area is the nonsorted circle, or "frost boil." These are small (typically ~50 cm – 5 m) mounds of soil formed by frost action and commonly found in areas of fine-grain sediment underlain by permafrost (Harris et al. 1998). Active frost boils are bare ground typically with small cracks on the surface, whereas older or inactive sites may be completely vegetated. Bare frost boils can be seen as conspicuous round white areas on the polygon tops in Figure 7.

Among the four study plots, C44 represents the highest elevation and C34 the lowest, though the difference is just ~50 cm between them. C44 is located on the east-facing beach ridge slope, an area which is generally associated with well-drained, sandy gravel substrate and low vegetation cover comprised mostly of grass and sedge species with a high diversity of lichen (Brown & Johnson 1965). The other three plots (C34, C37, and to a lesser extent C40), are more closely associated with the well-developed ice-wedge polygon "upland", which is actually lower in elevation relative to the beach ridge, and characterized by greater soil moisture content and higher bryophyte vegetation cover. Lower elevations are found further to the south and east along the Slough.

4 METHODOLOGY

The raw LIDAR point-cloud data were filtered and processed using a variety of interpolation methodologies in order to derive several high-resolution DEMs. Each DEM was compared to DGPS data as well as reference data withheld from the original LIDAR point cloud to evaluate the statistical accuracy of the interpolation methodology. The best method was used to process the four point-cloud datasets into fine-scale DEMs. These DEMs were classified based on microtopographical variation and subsequently used to analyze spatial trends in active-layer thickness (ALT) as well as the temporal trends in the 10 year DGPS record of heave and subsidence. That analysis was supplemented by a high-resolution land cover classification of aerial kite photography to further investigate local differences in annual ALT and subsidence.

4.1 Data Collection & Processing

4.1.1 DGPS Data

The 2010 DGPS data were collected on 16 - 18 August 2010 by Dr. Nikolay Shiklomanov as part of the annual CALM survey, which has been made annually since 2004. Two receivers were used, one serving as a base antennae (Trimble®NetR8) mounted on a telephone pole against the east side of the Barrow Arctic Science Consortium (BASC) facility at the former Naval Arctic Research Laboratory (NARL) building (~5 km from the study site) to provide a clear line of sight, and another (Trimble®NetR7) as a rover antennae in the field (Little 2006; Dmitry Streletskiy, pers. comm., 13 December 2012). At each of four CRREL plots a total of five DGPS points were collected – one at each of the four corners and one in the center (Figure 8). There

were two points for which there was no data available in 2010 (404 and 443 – referring to plots 40 and 44, points 4 and 3, respectively). Additionally, a series of DGPS data were collected on 20 frost boils located just NW of the four CRREL plots, also visible in Figure 8. While the LIDAR data collection focused on the CRREL plots, some of the scans captured the frost boil area as well, so the LIDAR point cloud was also evaluated at these points to determine if there were enough data to include them in analysis.

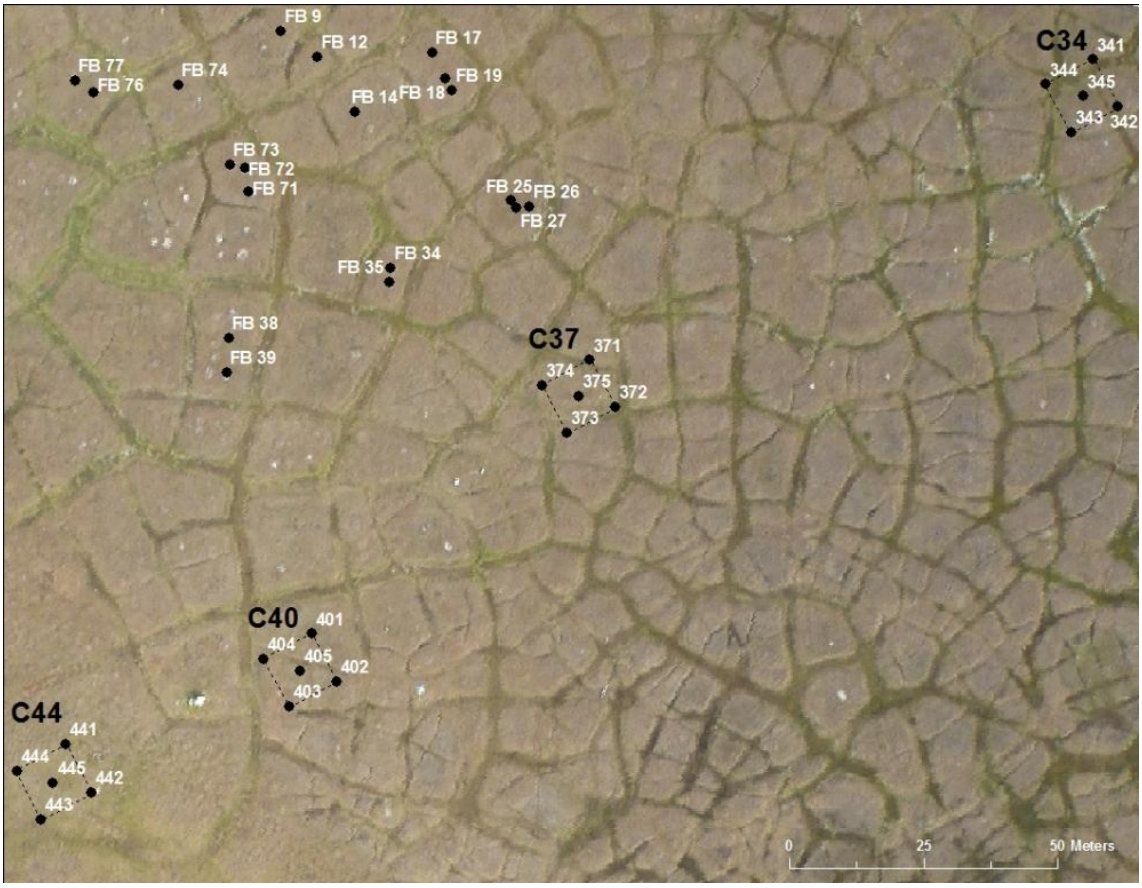

Figure 8. Aerial photo showing the locations of annual DGPS measurements in the study area. Points labeled "FB" indicate frost boils.

DGPS points were recorded on previously-installed University of Delaware Permafrost Group (UDPG) tube-shaped targets, approximately 20 cm in height and 2.5 cm in diameter (Little 2006). To reduce the potential for error, horizontal leveling of the rover antennae was done manually using a small level (Little 2006). A dual-

frequency real-time kinematic (RTK) survey method, using radio-link communication between the base station and the rover, was used to compute a 3D vector between the two GPSs to obtain vertical and horizontal resolution of 1-2 cm accuracy after occupying the target for approximately 8 minutes (Little 2006). After each DGPS point was measured, four manual measurements of the height of the antennae/tube were taken, and the mean height was used to adjust the DGPS point to the ground surface. Post-processing of the DGPS data was done with Trimble Geomatics Office™ (TGO) software, yielding vertical accuracies of $\leq$ 2cm (D. Streletskiy, pers. comm., 13 December 2012).

CALM project researchers began collecting high-resolution DGPS data at these sites in 2003, compiling a record of heave and subsidence. While only the DGPS data collected in 2010 were used to assess the LIDAR-derived DEMs, the ten-year record was incorporated into the analysis of microtopography and vegetation to enhance understanding of long-term heave and subsidence.

4.1.2 Active-Layer Data

The CRREL transect from the 1960s consisted of 20 10 × 10 m monitoring plots extending across the three main landscapes characteristic of the BEO: a large drained-lake basin, a raised beach ridge, and ice-wedge polygon uplands, terminating at the low, eroding lagoon bluff (Figure 6; Brown et al. 2000). While a variety of measurements were taken at these plots throughout the 1960s, annual end-of-season active-layer thickness (ALT) observations resumed in 1991 and continue to the present. The CRREL transect is located in the southeastern portion of the 1 km^2 ARCSS/CALM grid and four of these plots correspond to the four LIDAR scans (Figure 9).

Figure 9. Sampling design employed by CALM researchers to monitor active-layer thickness at each CRREL plot.

ALT measurements were recorded on a grid consisting of 36 points spaced 2 m apart within each plot, including at the corners where DGPS readings were taken,

Figure 10. Wooden posts marking the exterior nodes of the ALT sampling grid at CRREL Plot 44 (Photo: Nikolay Shiklomanov).

though not at the center point where the fifth DGPS measurement was recorded (Figure 9). The grid was defined by twine strung between wooden posts marking the exterior nodes, and each ALT measurement was taken within 15.2 cm (6 in.) of the intersecting points, (Figure 10; Brown & Johnson 1965; Streleskiy, pers. comm., 7 January 2013). This sampling design produced a record of 144 data points (36 points × 4 plots) for the study area.

The 2010 ALT measurements were analyzed using descriptive statistics (minimum, maximum, mean, range, standard deviation) within each microtopographic and land-cover classification for each plot to examine the correlation between these variables and the spatial variability of thaw depth.

An investigation into the historical ALT data from the CRREL plots produced a time-series of 23 years (1962-66, 1992-93, and 1997-2012) of end-of-season ALT data for all 144 points. Gaps in this time series were the result of incomplete data, only early-season data, or no data collection for a given year. This temporal record was also analyzed using descriptive statistics in the context of microtopography and vegetation at each plot.

4.1.3 Historical Elevation Data

The time-series of data available from the CRREL plots records many environmental variables including air temperature, soil temperature, soil moisture, and snow cover. While not all of the available data was utilized in this study, one record of particular interest was the surveyed elevation, recorded in the early 1960's, for each of the 36 points within the CRREL plots. The original data (Brown et al. 1970) was

explored to determine if it could provide the groundwork for an investigation into the temporal changes in elevation of a much larger sample size (144 surveyed points from the 1960s compared to only 20 DGPS points in the recent record) and analyzed using microtopography derived from modern DEMs. However, lack of information about the surveying datum used for the 1960s elevation measurements meant that comparison of absolute elevations were not available for direct comparison at the time of this study

4.1.4 Kite Photography

On 14 August 2012, a series of high-resolution aerial images were collected in the BEO by Sergio Vargas as part of ongoing vegetation studies. The imagery was captured using a Panasonic® Lumix DCM TS3 12 megapixel camera mounted on a kite flying ~400-450 m above ground level (Figure 11, Sergio Vargas, pers. comm, 17 October 2012). The spatial coverage of the raw images included all four CRREL plots at a resolution of ~10 cm; the photographs had not been georeferenced or classified.

Figure 11. Sergio Vargas and the kite used to collect high-resolution aerial imagery of the study area, August of 2012 (Photo: Kelsey Nyland).

Since the photographs covered an area much larger than the scope of this study (400 m × 300 m per photo), one photograph containing all of the plots was selected to be georeferenced and classified. This photograph was cropped to an area

~200 m × 275 m, then georeferenced to the LIDAR data using the georeferencing toolbar in ArcGIS® 10.0, employing a nearest-neighbor third-order polynomial transformation method with 58 ground control points distributed evenly across the landscape, resulting in an RMSE of 0.89. For the plot-level analysis, the original photograph was cropped to a series of 4 50 m × 50 m images centered over each of the four CRREL plots. These smaller images were individually georeferenced utilizing a nearest-neighbor first-order polynomial (affine) transformation with 6-8 ground control points per image and overall RMSE values of ≤ 0.4 (Figure 12).

Figure 12. Georeferenced high-resolution kite photograph of the entire study area, overlain with cropped and independently georeferenced images of the individual study plots.

4.1.5 LIDAR Data

On 16-18 August 2010, thirteen LIDAR scans were completed on four 10 m × 10 m plots located in the southeastern corner of the ARCSS/CALM grid by Marianne Okal from UNAVCO[1] (M. Okal, pers comm, 20 March 2012). Locations of the scan sites relative to the CRREL plots are shown in Figure 7. Scans were made using a Riegl® VZ-400 Terrestrial Laser Scanner with a D700 high-precision camera mount (Figure 13). Reference points were University of Texas-Dallas (UTD) 12 cm Red Disc Targets placed at 14.7 cm offset from the bottom of the antennae mount. The targets were georeferenced using a Trimble® GPS 5700 with R7 receivers and a Zephyr® Geodetic Antennae that occupied each UTD Red Disc target for at least an hour. GPS points were differentially corrected using BASC's Base Station less than 10 km from the study site (70°28'19.3"N, 157°24'28.20"W) and subsequently processed to within 3 cm vertically for all points.

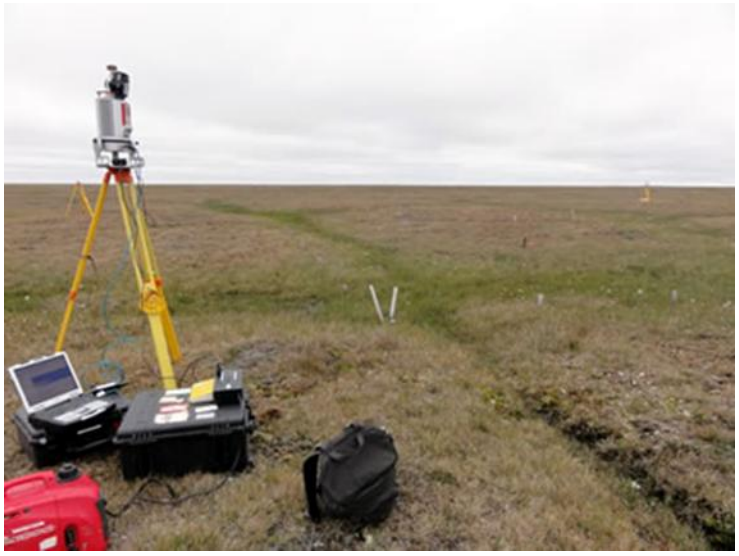

Figure 13. Terrestrial LIDAR system used to collect data at the study sites, August 2010 (Photo: Marianne Okal).

One of the first steps in utilizing terrestrial LIDAR is the co-registration of the datasets to a local (reference) coordinate system using designated targets as reference points and applying iterative closest-point algorithms (Besl & McKay 1992). Each scan has its own relative coordinate system that pinpoints the scanner as the origin, so a

[1] UNAVCO, Inc., Boulder, CO

transformation matrix must be imposed on each point cloud in order to merge and transfer multiple scans into a single coordinate system (Bonnaffe et al. 2007). In order to register multiple scans to produce a mosaic, there must be at least 10% overlap between successive scans (Bonnaffe et al. 2007). The registration of this LIDAR data set was done by M. Okal using RiSCANPro software, with scans 2 and 3 registered to scan 1 for each site using the UTD targets are reference points. This process yielded standard deviations of 0.3 – 1.02 cm, and all data registered to the target GPS points with standard deviations of $\leq$ 0.4 cm.

To further process the data, the resulting local coordinate system must be transferred to a global reference system, using coordinates of the targets in the selected reference frame as control point information (Böhm & Haala 2005). To accomplish this, the LIDAR datasets were initially exported as XYZ (Earth-Centered, Earth-Fixed) data files with ellipsoid heights (m), RGB values (0-255), and intensity values (0-65535) for all points. The XYZ files were then converted into longitude and latitude (WGS84) to facilitate processing inside GIS (M. Okal, pers. comm., 1 May 2012). Those files were exported in ASCII and subsequently converted by the author into the .las file format using the txt2las function of LAStools® software. Because all data from the CALM project were recorded in UTM 4N (NAD83), the .las files were projected into that coordinate system for comparative analysis using LAStools® las2las. LAStools® default processing truncates the input data to two decimal places limiting the output to cm-scale resolution which in this case was a degradation of the original data (Figure 14).

To preserve the precision of the original data, a flag ("target_precision 0.001") was added to the syntax of the las2las tool to retain three decimal places for all coordinates.

During the initial export of the data by UNAVCO, most scan positions were broken into 2-3 separate data files, producing 38 text files in total that, when combined, represented the entire LIDAR data collection. These individual scans were merged together using LAStools® lasmerge into one file containing 181,042,837 points. Four of the original data files (C34_Scan1_pt3, C37_Scan1_pt2, C37_Scan2_pt3, and C40_Scan2_pt1) were corrupt and could not be processed with the rest of the data. These files could not be re-exported by UNAVCO in time to be included in this study. The final dataset used for this project is shown in Figure 15.

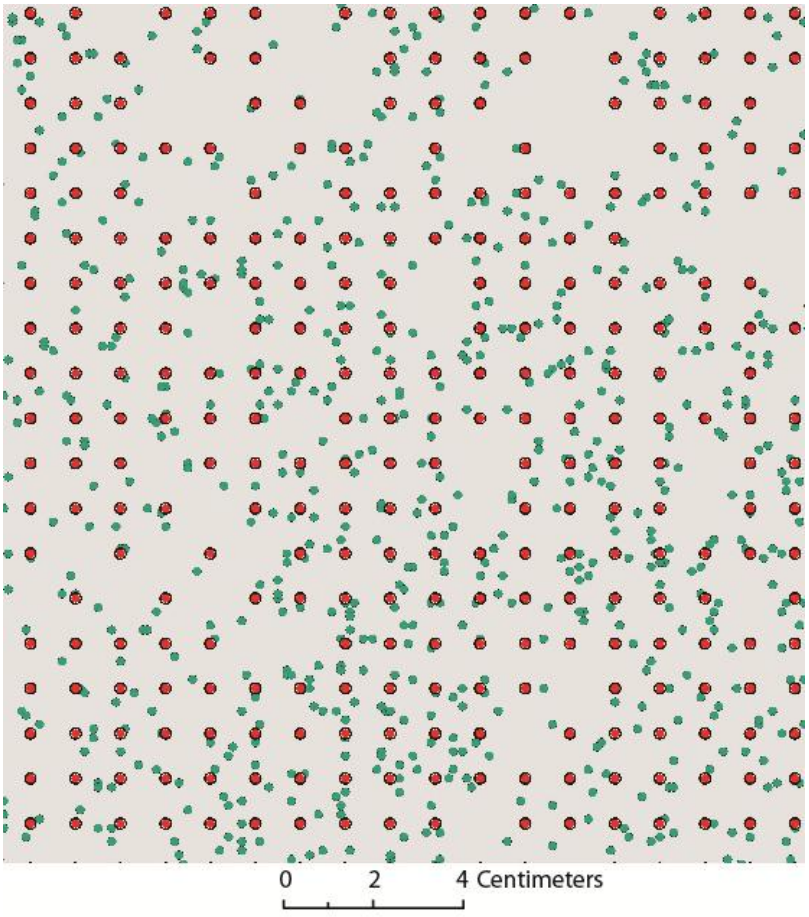

Figure 14. Detail map showing the loss of accuracy which could be caused by rounding during data projection. Original data points are shown in green; red points represent the same dataset rounded to two decimal places in UTM coordinates.

Figure 15. Individual scans merged together to display the entire raw LIDAR dataset, rendered using RGB values.

In order to compare the DGPS data directly to the LIDAR data, the original point cloud was analyzed before it was processed into a DEM. Clips were taken of the merged point cloud at each DGPS location (CRREL plots and frost boils) using LAStools® lasclip function and specifying a 5 cm diameter circle (created in ArcGIS and stored in ESRI shapefile format) to define the area around the point. If more than one LIDAR point fell within that area, the lowest point was taken to represent the ground surface.

In addition to the 38 scan files, four area-of-interest (AOI) files were exported by UNAVCO of the area of the CRREL plots with a buffer of ~2 m on all sides. However, the AOI file for plot C40 was significantly smaller in terms of number of points and was

not buffered, so a new AOI file was created by clipping the merged file of all scans. This new AOI file was roughly equivalent to the other three in both area and number of points, and was used for all further analysis. Additional processing was also done to the C34 AOI file to remove contained 80 points (z-values of 2.365 - 19.609 m) believed to be erroneously high. This filtering was accomplished using LAStools® las2las (filter) specified to "clip_z_above 2". A summary of the AOI files is presented in Table 1.

Table 1. Summary of the LIDAR files defining the four CRREL plots.

	C34	*C37*	*C40*	*C40_new*	*C44*
No. of points	7,303,671*	7,872,785	2,671,084	7,370,668	6,981,650
Min (m)	1.109	1.242	1.423	1.383	1.786
Max (m)	1.928*	2.378	2.484	2.528	2.616
Range (m)	0.822*	1.136	1.061	1.145	0.83

* The original C34 file contained an additional 80 points which were removed prior to analysis.

The instrument used for the LIDAR collection (Riegl® VZ-400) returns the full waveform but it cannot be exported in a single file; rather, first and single returns, "multiple" (middle) returns, and last returns subsets can be extracted by applying a filter when viewing the data and saved in separate files (M. Okal, pers. comm., 5 January 2013). Due to the dense and wet ground cover at the study sites, most of the LIDAR data points in this dataset were single returns (M. Okal, pers. comm., 20 April 2012), so only first and single returns were exported. Last returns were exported for one sample plot (C34, Figure 16) but due to the low point density they were not investigated or exported for the others. While not useful on their own, the information contained in the last returns may have helped to inform analysis and interpretation of the first and single returns; however, this data was not available for inclusion in this analysis.

Since the data was delivered as an unclassified, single-return point cloud, the points had to first be classified as "ground" and "non-ground" in order to extract bare earth (the surface that represents the boundary between solid ground and surface objects such as vegetation and buildings; Vosselmar & Maas 2010) to create DEMs. The four AOI files were processed through LAStools® lasground utility repeatedly with different terrain type and granularity settings; however, all modifications resulted in all points being classified as "ground". The inability to extract bare-earth points from the cloud may be explained by the incredibly dense nature of the terrestrial LIDAR data – because of the data density, there may not be enough area for the software to determine what is ground (John Gale, pers. comm., 21 December 2012). It could also be a result of the organization of the terrestrial data – aerial LIDAR data is collected in swaths and stored in a fairly uniform way based upon their spatial location, whereas terrestrial LIDAR data is collected and often stored in a much more random spatial association, which can be difficult for interpolation algorithms to process (John Gale, pers. comm., 21 December 2012). The result of the lasground operation was four new

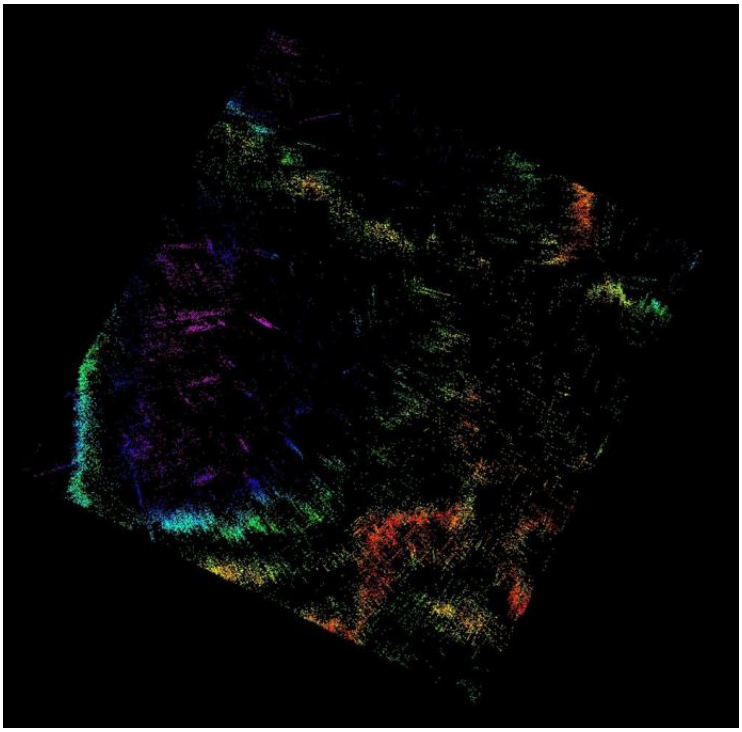

Figure 16. Last returns from plot C34, colored using elevation. The streaking pattern in the first returns is also visible in the last returns, most noticeably on the tops of the ice-wedge polygons (left side of image).

AOI files, each with the same number of points as its corresponding original, but with all of those points classified as ground and assumed to represent the bare earth surface.

To further examine the original data, point-density maps were created for each plot at two different resolutions (1 cm and 10 cm). Point density maps are useful as visual explorations of underlying data, allowing areas with fewer points to be investigated and illustrating interpolation and extrapolation areas (Vosselmar & Maas, 2010). In addition to point density, LIDAR intensity values, representing the return strength of the laser pulse, were also mapped at 1 cm resolution. Intensity values are, at least in part, determined by the reflectance of a surface, making it possible to discern different land cover classes in carefully calibrated data (Wang & Glenn 2009). The intensity values were evaluated to determine if they could be useful in both error interpretation and in the classification of the microtopography and/or landcover. Both the density and intensity images were created with LAStools® lasgrid function, specifying the density (16-bit) and intensity as the items to grid and step values to reflect the desired output resolutions.

4.2 DEM Interpolation and Analysis

After extensive research into the various processing capabilities, accessibility, and cost of different LIDAR software (FUSION, LAStools®, SCOP++™, LASEdit, SAGA, Open Topography, MicroDEM, and LIDAR Analyst®), two programs – LAStools® and LIDAR Analyst® – were selected for DEM generation. Plot C34 was selected as the evaluation plot for initial interpolations.

4.2.1 Thinning the Point Clouds and DEM Generation

To assess the effects of LIDAR point density on the accuracy and appearance of the output DEMs, four new .las files were created from the original AOI file, thinned to different resolutions (1 cm, 2 cm, 5 cm, and 10 cm) using LAStools® lasthin, keeping the lowest point in each grid cell. These files were evaluated using three different processing tools – LAStools® blast2dem, LIDAR Analyst® LAS file to Raster with Filtering, and LIDAR Analyst® Extract Bare Earth – to create an array of DEMs for analysis.

LAStools® blast2dem uses "a bottom-up approach that repeatedly refines an initial ground estimate" using a triangulated irregular network (TIN) that is initially constructed from the lowest points of a grid with selected step size, gradually added to in several passes, and immediately rasterized onto a DEM (Isenburg 2011). This approach is similar to "virtual deforestation" (VDF) algorithms, many of which are fully automated and have been successfully used to map ground surface in heavily forested areas (Haugerud & Harding 2001). The only variable available for manipulation by the user was the "kill triangles" variable, adjustment of which did not affect the output DEMs because the study area did not contain any large data voids (i.e. lakes or tight boundaries).

LIDAR Analyst® LAS file to Raster with Filtering uses an unspecified "advanced algorithm" to convert point cloud data directly to raster (DEM) format. The only variable to specify is whether or not to "fill holes in the data", an option which produced no quantifiable differences in output DEMs with this data.

LIDAR Analyst® Bare Earth Extraction, which uses an iterative spline interpolation algorithm, provided the most user-defined options for creating a DEM. Processing options that were tested included: removing spikes and pits before processing,

smoothing bare earth using low-pass filter, extraction method 1 (rasters or point clouds) or extraction method 2 (point clouds), hierarchical spline interpolator or ArcGIS spline interpolator, option to clean up bare earth, and manually setting the number of points for interpolation, spline tension, percentage overlap, number of iterations for bare earth extraction, and ground parameters. However, although all these options were evaluated, no combination changed the output DEM visibly or quantifiably way, perhaps because of data density and lack of tall vegetation and buildings that these algorithms were designed to extract. The tool was run successfully to produce the final outputs used for analysis with the default settings (interpolation based on elevation, no automatic filling of holes in data, filtered by all returns, output raster properties set from input LAS file) on the 10 cm, 5 cm, and 2 cm data but was unable to process the 1 cm data and the original AOI point cloud, even when left to run for over 72 hours.

4.2.2 Assessing DEM Accuracy

All output DEMs for C34 were assessed using the 5 DGPS points collected within that plot at the time of the LIDAR acquisition. DEM values were extracted at each control point using the Extract Values to Points tool of ArcGIS Spatial Analyst with the option to interpolate values at point locations. Descriptive statistics were calculated for each set of points and the five DEM-generation methods which produced the smallest average error and low standard deviation were applied to the other three plots. These were reevaluated using the entire set of 18 DGPS points available for the four plots by calculating descriptive statistics, mean bias error (MBE), and mean absolute error

(MAE). The DEMs with the overall smallest error with a low standard deviation at all plots were used for the rest of the analysis.

To fully assess the accuracy of the DEM interpolation method, four different sets of data points were withheld from the original point cloud before it was used to generate the DEM. These control point datasets were created using LAStools® lasthin with the following specifications: 1) withhold the lowest point every 1 m; 2) withhold a random point every 1 m; 3) withhold the lowest point every 50 cm; and 4) withhold a random point every 50 cm. All four control point datasets were then compared to their respective DEMs (in this case, 10 cm-resolution DEMs created with LIDAR Analyst® LAS to Raster) to assess errors. DEM values were extracted for each control point using the Extract Values to Points tool of ArcGIS Spatial Analyst with the option to interpolate values at point locations. The attribute tables of the output files were examined and any points without corresponding raster values (points on the edges of the extent) were removed. Residuals were calculated between the z-value of the DEM (z) and the "true" terrain surface (Briese et al 2002) and mean bias error (MBE), mean absolute error (MAE), and root-mean-square error (RMSE) were found for each plot. All measures of error were less than 1 cm in magnitude (Table 2).

Table 2. Descriptive statistics of LIDAR and DEM elevations and **s**ummary of errors (DEM-LIDAR) for plot C34 using four different methods of withholding points from the LIDAR datasets. Units are cm above ellipsoid. Residuals – max is the absolute value of the maximum residual of the dataset.

Control Point Data Set	*1 m lowest*		*1 m random*		*50 cm lowest*		*50 cm random*	
	LIDAR	*DEM*	*LIDAR*	*DEM*	*LIDAR*	*DEM*	*LIDAR*	*DEM*
Minimum	110.6	111.6	115.5	115.6	110.6	111.7	113.6	114.1
Mean	127.6	127.7	132.3	132.3	129.6	129.7	132.4	132.4
Maximum	148.5	148.6	151.1	151.1	149.9	149.9	152.6	152.6
Range	37.9	37.0	35.6	35.5	39.3	38.2	39.0	38.4
Standard Deviation	9.3	9.3	9.2	9.2	9.5	9.5	9.3	9.2
Residuals - Max.	1.3		0.5		4.1		1.9	
Residuals - Mean	0.1		0.1		0.2		0.1	
RMSE	0.2		0.1		0.2		0.1	
MBE	-0.1		< 0.1		-0.1		< 0.1	
MAE	0.1		0.1		0.1		0.1	
Number of Points	242		243		898		904	

Because of the small magnitude and differences in errors between the methods, the "50 cm lowest" dataset was chosen to assess the final DEMs for the other plots since it was presumed to be a closer representation of the ground surface than the "random" datasets and contained a larger sample size than the "l m lowest" dataset. Statistics were then calculated for each plot using the withheld LIDAR points as ground truth for the DEM. Statistics were also calculated using the DGPS points as ground truth; however, due to the small sample size at each plot, just one set of statistics was calculated to summarize all plots.

To examine the spatial pattern of error, residuals points were mapped using the entire point-cloud dataset that was used to generate to DEM for each plot. This point map was calculated as LIDAR elevation – DEM elevation in cm and clipped to the area of the study site.

4.3 Microtopography Classification

Polygon centers and troughs, visible in the aerial photographs, were classified for microtopography based upon relative elevation as that is their defining characteristic. Because the average elevations of each of the four plots varied substantially (~63 cm difference between C34 and C44), one elevation value could not be used as the break point with which to differentiate polygon centers and troughs at all sites. Consequently, the elevation was determined for each plot through visual comparison of the results to the DEM and aerial photographs. For the final classification, boundaries to differentiate polygon centers and troughs at each plot were set at: 1.27 m for C34; 1.36 m for C37; 1.51 m for C40 m; and 1.88 m for C44.

Terrain analysis was necessary to identify the sides of the polygons and other areas of sloping terrain. Different measures and indices for quantifying microtopographical variability were initially tested on plot C34. The DEM raster files originally exported by LIDAR Analyst® at a pixel resolution of 1 cm (not representative of spatial resolution but optimal for visual display) proved too fine a scale for meaningful terrain analysis and the rasters were re-exported using the Aggregate tool set to the "mean" aggregation technique at the following resolutions for comparative analysis: 10 cm, 20 cm, 30 cm, and 50 cm. The ArcGIS Focal Statistics tool was used to create sets of raster files of the mean, minimum, maximum, and range of the 10 cm resolution DEM for plot C34 for use in topographic index calculations, using three different cell neighborhoods of three, five, and ten for comparative analysis.

An array of terrain measures were calculated, including: first-order surface derivatives (slope), second-order derivatives (curvature, profile curvature, planform curvature), measures of local surface variability (standard deviation of slope, standard

deviation of elevation, slope variability), and more complex terrain indices (elevation-relief ratio, Melton's ruggedness number, topographic position index, terrain ruggedness index, compound topographic index). All calculations were examined at three or more different resolutions of the DEM and with three different neighborhood sizes (three-cell, five-cell, and ten-cell) to determine the most useful resolution for each statistic. This decision was made by visually comparing the outputs to both the DEM and the aerial images of the site to see how accurately they described the landscape. The calculations are summarized in Table 3, which lists which were determined to be the most useful cell neighborhood and DEM resolution for each variable.

Table 3. Terrain calculations and corresponding input specifications.

Variable/Index	*Description/Equation*	*Cell Neighborhood*	*Input DEM Resolution*
Slope (gradient, or rate of maximum change in z-value; Burrough & McDonnell 1998)	$\text{Atan}(\sqrt{([\Delta z/\Delta x]^2 + [\Delta z/\Delta y]^2)}) * (180/\pi)$	3 × 3	30 cm
Curvature (Buckley 2010)	second derivative of the surface (i.e. the slope of the slope)	3 × 3	30 cm
Profile Curvature (Buckley 2010)	curvature parallel to the direction of the maximum slope	3 × 3	30 cm
Planform Curvature (Buckley 2010)	curvature perpendicular to the direction of the maximum slope	3 × 3	30 cm
SDE (standard deviation of elevation; Ascione 2008)	Std(DEM)	5 × 5	10 cm
SDS (standard deviation of slope; Grohmann 2011)	Std(Slope)	10 × 10	10 cm
SV (slope variability; Ruszkiczay-Rudiger et al. 2009)	$\text{Slope}_{max} - \text{Slope}_{min}$	5 × 5	10 cm
E/R (elevation-relief ratio; Pike & Wilson 1971)	$(\text{DEM}_{mean} - \text{DEM})/\text{DEM}_{range}$	10 × 10	10 cm
MRN (Melton's ruggedness number; Melton 1965)	$(\text{DEM}_{max} - \text{DEM}_{min})/\sqrt{\text{Area}}$	5 × 5	10 cm
TPI (topographic position index; Weiss 2001)	$(\text{DEM} - \text{DEM}_{min})/(\text{DEM}_{max} + \text{DEM}_{min})$	10 × 10	10 cm
TRI (terrain ruggedness index; Riley et al. 1999)	$\sqrt{\lvert(\text{DEM}_{max})^2 - (\text{DEM}_{min})^2\rvert}$	5 × 5	10 cm
CTI (compound topographic index; Evans 2004)	$\ln(\text{As}/(\tan(\text{beta})))$ †	1 × 1	10 cm

† As = Area Value calculated as (flow accumulation + 1)*(pixel area m^2); beta = slope (in radians)

Slope and curvature were calculated using the respective Surface tools in Spatial Analyst. Standard deviation calculations, as well as input slope variability rasters, were made using the Focal Statistics tool. All other calculations were performed in the Raster Calculator based on the formulas in Table 3. Through qualitative visual analysis using the DEM and the aerial images, the two variables that best captured the microtopography of the plot were identified as slope (at 30 cm resolution), which provided the best general picture of topography, identifying the general edges of the polygons distinctly, and Melton's ruggedness number (at 10 cm resolution) which differentiated changes at a finer scale, particularly terrain variations on the centers of the polygons. These two rasters were combined using the Raster calculator with the equation = [Slope] + ([MRN]*100) and the result was manually classified using a class boundary of 6.5 to differentiate flat (homogenous) and sloping (heterogeneous) terrain.

Finally the DEM and the Slope/MRN rasters were combined into a new microtopography classification with four classes – troughs; low sides (sloping areas in the troughs); high sides (sloping areas on the polygon centers), and polygon centers. This classification was visually assessed using the DEM and aerial images and then repeated for the remaining three plots.

To categorize microtopography for each of the 36 monitoring points within each plot, the classified microtopography images were clipped using a 30 cm diameter circle (approximating the 6 in sampling radius of the CALM ALT measurements). Whichever category had the largest number of pixels within each circle was assigned as the microtopography class. The DGPS points were assigned in a similar manner, but with a 5 cm diameter circle representing the area occupied by the DGPS target and receiver.

Once all points were classified, it was determined that there was not a large enough sample size to statistically assess the differentiation between high and low sloping sides (n=10 and n=13, respectively, out of a total of 164 points), so the two "sides" classes were grouped, resulting in three microtopography classes for the final analysis – centers, sides, and troughs.

4.4 Vegetation Classification

Interpretation of ALT and DGPS data was also examined by the creation of a land-cover classification of the four CRREL plots. At the time of the data analysis, the highest resolution land-cover classification available for the study area was based upon 2002 Quickbird image (Figure 17), with a resolution of ~ 0.7 m, which provided general information about what land-cover classes were present at the study site but was too coarse to use for analysis of the ALT and DGPS data. In order to analyze land cover differences at the plot level, a new classification was created from the kite photographs described in Section 4.1.4. These classifications were created with vegetation index (VI) techniques, which use "arithmetic operations on the available bands (visible light, near-infrared, etc.)… to enhance some features and better visualize the vegetation" (Ponti 2012).

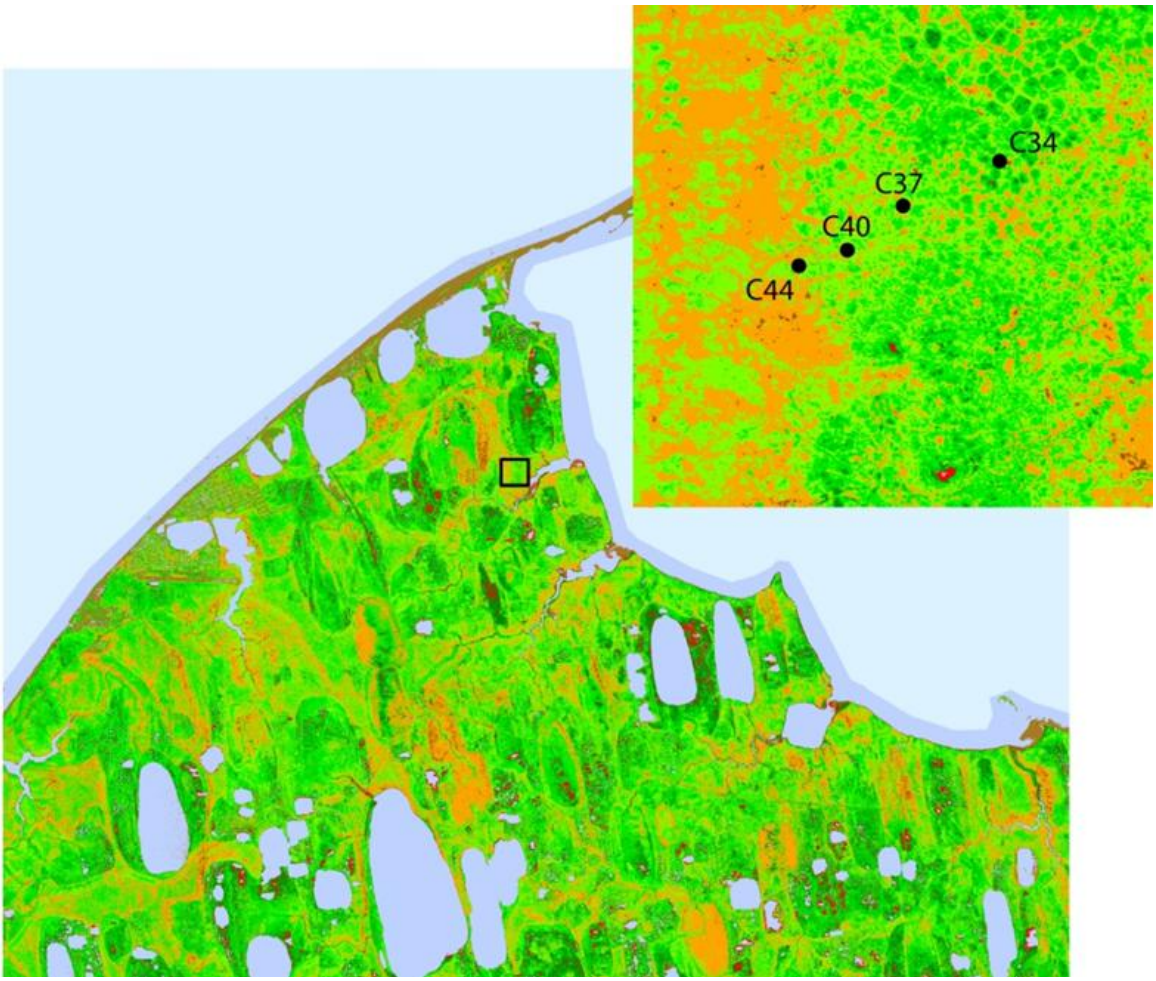

Figure 17. High resolution (2.4 m multispectral, pan-sharpened to 0.7 m resolution) land-cover image derived from Quickbird satellite imagery collected on August 1, 2002. Data provided by NCAR/EOL under sponsorship of the National Science Foundation: http://data.eol.ucar.edu.

The kite photographs were collected using three bands from the visible spectrum: red (~630-690 nm), green (~520-600 nm), and blue (~450-520 nm). While VIs often use the near-infrared portion of the visible spectrum, there are a number which can be calculated using reflectance from just the visible wavelengths. Since a review of current literature did not reveal a commonly used vegetation index to use for differentiation of tundra vegetation which did not include the near-infrared, seven VIs were explored for use in this study. Each VI was tested on the georeferenced image of plot C34, including: the Green-Red Vegetation Index (GVRI; Motohka et al. 2010), Excess Green (ExG or

2B_RB; Ponti 2012), Triangular Greenness Index (TGI; Hunt et al. 2013), Green Leaf Index (GLI; Louhaichi et al. 2001 and Hunt et al. 2013) Visible Atmospherically Resistant Index (VARI; Gitelson et al. 2002), Visual Vegetation Index (VVI; Ponti 2012), and Color Index of Vegetation Extraction (CIVE; Ponti, 2012). These indices are summarized in Table 4.

Table 4. Vegetation indices which can be calculated using bands in visible wavelengths showing equations and corresponding raster calculations.

Index	*Equation*	*Raster Calculation*
GVRI (green-red vegetation index; Motohka et al. 2010)	$(R_g - R_r)/(R_g + R_r)$	("Band_2" - "Band_1") / ("Band_2" + "Band_1")
ExG (excess green; Ponti 2012)	$2G - R - B$	(2 * "Band_2_normalized") - "Band_1_normalized" - "Band_3_normalized" †
TGI (triangular greenness index; Hunt et al. 2013)	$-0.5[(\lambda_r - \lambda_b)(R_r - R_g) - (\lambda_r - \lambda_g)(R_r - R_b)]$	-0.5 * ((165 * ("Band_1" - "Band_2")) - (80 * ("Band_1" - "Band_3")))
GLI*(a)* (green leaf index; Louhaichi et al. 2001)	((G-R)+(G-B))/(G+R+G+B)	(("Band_2" - "Band_1") + ("Band_2" - "Band_3"))/("Band_2" + "Band_1" + "Band_2" + "Band_3")
GLI*(b)* (green leaf index; Hunt et al. 2013)	$(2*R_g - R_r - R_b)/(2*R_g + R_r + R_b)$	(2 * "Band_2" - "Band_1" - "Band_3") / (2 * "Band_2" + "Band_1" + "Band_3")
VARI (visible atmospherically resistant index; Gitelson et al. 2002)	$(R_g - R_r)/(R_g + R_r - R_b)$	("Band_2" - "Band_1") / ("Band_2" + "Band_1" - "Band_3")
VVI (visual vegetation index; Ponti 2012)	$[(1 - \lvert R - R_o/R + R_o\rvert) * (1 - \lvert G - G_o/G + G_o\rvert) * (1 - \lvert B - B_o/B + B_o\rvert)]^{1/w}$	(1 - (Abs(("Band_1" - 40)/("Band_1" + 40)))) * (1 - (Abs(("Band_2" - 60)/("Band_2" + 60)))) * (1 - (Abs(("Band_3" - 10)/("Band_3" + 10))))
CIVE (color index of vegetation extraction; Ponti, 2012)	$0.441R - 0.811G + 0.385B + 18.787$	(0.441 * "Band_1") - (0.811 * "Band_2") + (0.385 * "Band_3") + 18.787

†Calculation for normalized bands: "Band_1" / ("Band_1" + "Band_2" + "Band_3")

To perform these calculations inside of ArcGIS, each image band was exported as a separate raster file and converted into floating files using the 3D Analyst Float tool. Raster Calculator was then used to calculate the VIs described in Table 4. These images were then compared to the original kite photos and the one that most accurately represented the vegetation cover (in this case, the VVI) was selected as the basis of the new classification and calculated for the remaining three plots. Figure 18 shows the individual raster bands used to derive to vegetation indices as well as a sample calculation.

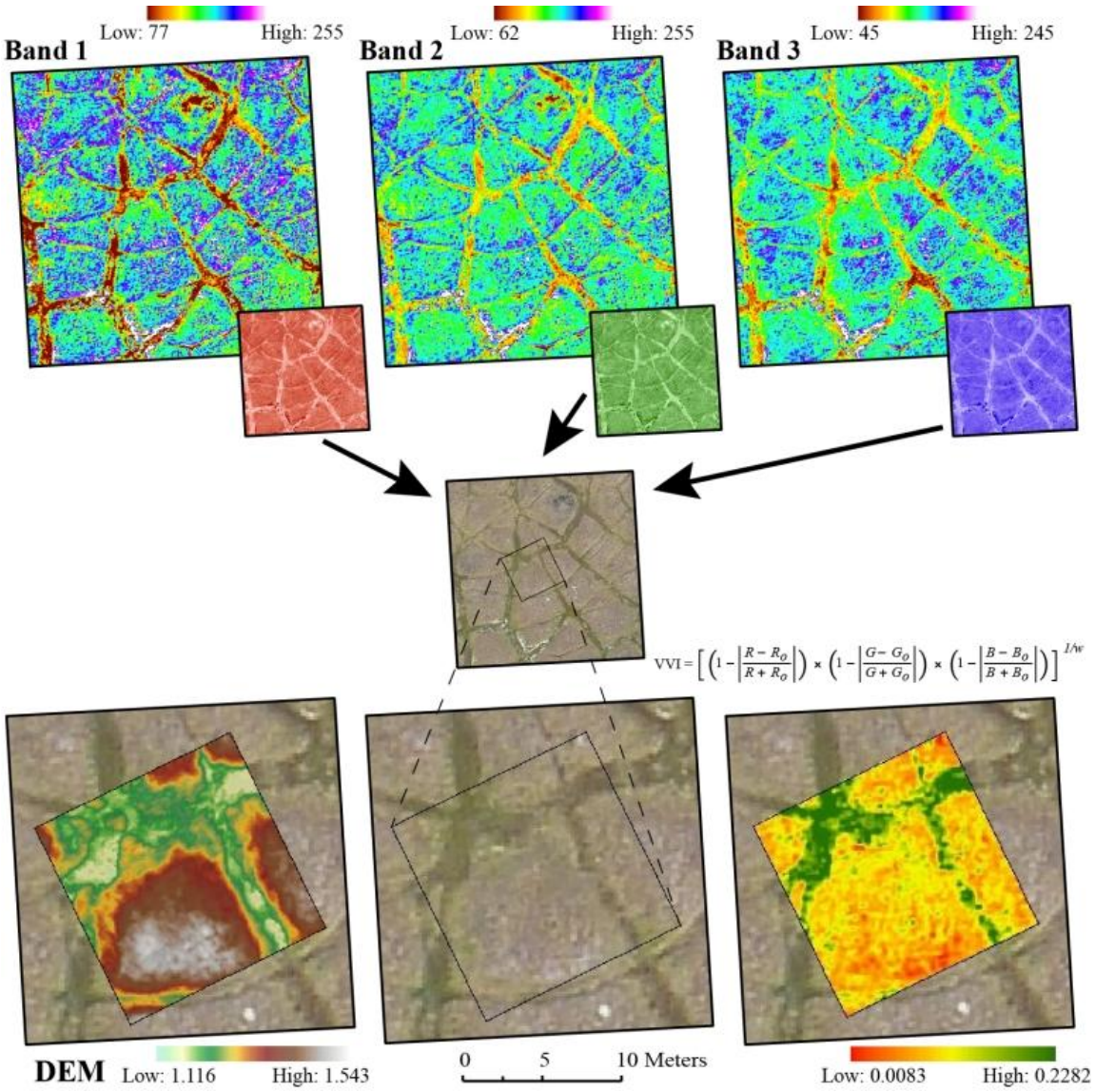

Figure 18. Calculation of the VVI for plot C34. Three visible bands make up the original image, of which individual bands were used in the calculation of the VVI and other indices. The original aerial image and DEM are shown for reference.

The VVI images were then categorized (i.e. density sliced) using boundaries chosen to reflect the local variations in vegetation observed in both the aerial images as well as in on-the-ground photographs of the plots (Figure 19).

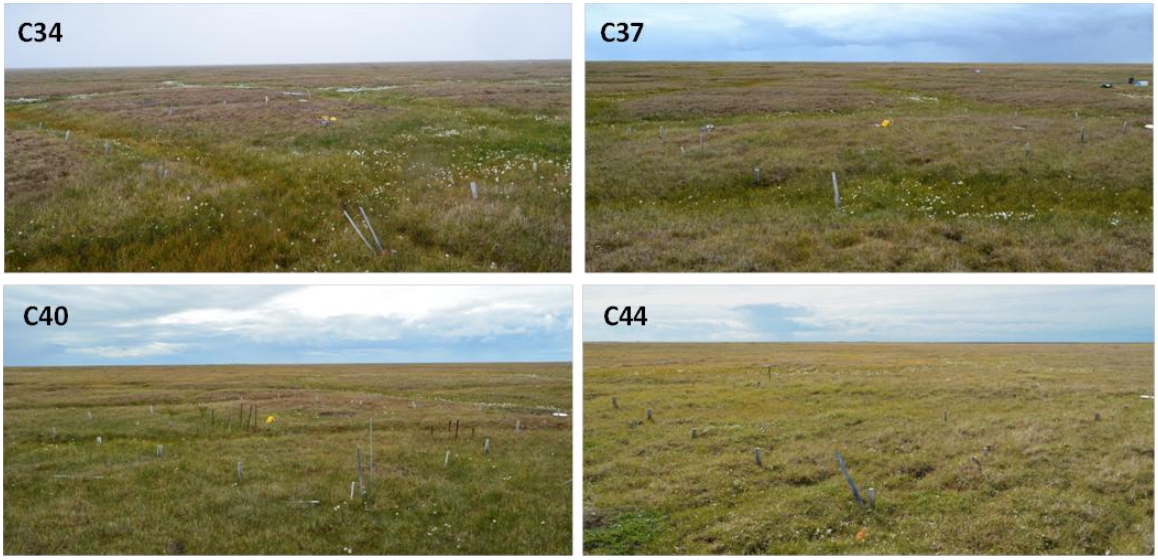

Figure 19. Photographs of the four study plots, August 2012. Each photograph was taken from the northeastern corner of the plot, facing southwest. Photos: Nikolay Shiklomanov.

A series of land-cover classifications were created containing between three and five classes each – one class representing bare ground (frost boils) and two to four other classes representing different types of vegetation. Categorization of the ALT and DGPS observation locations were done using the same methodologies described for the microtopography classifications for each of the three potential land-cover classifications. The classification which appeared to most accurately represent the vegetation observed in the photographs was chosen for further analysis.

The classification that was chosen contained four classes – one for bare ground (frost boils) and three for vegetation – with boundaries at 0.020, 0.042, and 0.060. The 2002 Quickbird classification (Figure 17) identified five types of land cover within the four study plots: wet graminoid tundra, moist graminoid tundra, dry-moist dwarf shrub-

graminoid tundra, dry dwarf shrub-graminoid tundra, dry dwarf shrub tundra (Tweedie 2010). These classes were simplified down to three – dry graminoid tundra, mesic graminoid tundra, and we graminoid tundra – based on the Alaska vegetation classification by Viereck et al. (1992) that differentiated classes for graminoid and forb herbaceous tundra based on moisture content of the substrate. Vegetation classes were delineated based on the following definitions: wet – sites that are saturated or semi permanently flooded, usually with standing water for part of the year; mesic – moist sites but without standing water; and dry – sites that are dry, usually rocky and well drained (Viereck et al. 1992), definitions which correlate well with conditions observed on the ground and in photographs of the study sites.

4.5 Statistical Analysis

For each plot, descriptive statistics of ALT (minimum, mean, maximum, range, and standard deviation) were calculated using two different subsets of the CALM data: 1) a snapshot in time, using 2010 data that was collected at the time of the LIDAR collection, and 2) a time series using the modern ALT data that coincides with the 10-year DGPS record (2003-2012).

Utilizing the microtopography and land-cover classifications described above, descriptive statistics were also calculated for each landcover and each microtopography class for three different subsets of the data: 1) a snapshot in time, using 2010 data, 2) a time series using the modern ALT data (2003-2012), and 3) a time series using the historic ALT data (1962-1966). Goodness-of-fit statistics and box plots were used to assess trends both visually and quantitatively (based upon the regression equations) for all years for which data was available.

Descriptive statistics were also calculated for the 10-year DGPS record of subsidence (2003-2012), first by plot and then by landcover and microtopography classes. Scatterplots were used to visually and quantitatively assess trends (based upon the trend lines).

5 RESULTS AND DISCUSSION

5.1 LIDAR point cloud analysis

Direct analysis of the raw LIDAR point cloud values at the CRREL DGPS sites revealed differences of 0.7-7.6 cm between the two datasets. Point density in the immediate vicinity of the measurement sites was highly variable, ranging from 5 to 660 points within the clipped area (~20 cm^2). Residuals at individual points are shown in Table 5 and summary statistics are provided in Table 6.

With the exception of two points, the LIDAR data consistently returned height values above those measured by DGPS. Most of these residuals were quite small, with an average of 3.8 cm. The differences between the LIDAR point cloud and the DGPS measurements might be explained in part by the artifacts inherent in the LIDAR data that were discovered in the DEM generation process (Section 5.2). Streaking patterns in the point cloud produced ridges ~2-5 cm in height on the interpolated DEM, and 70%.of the differences observed between the LIDAR and the DGPS data were less than 5 cm. If the artifacts could be removed, it may significantly improve the accuracy of the LIDAR data compared to the DGPS data.

Table 5. LIDAR points contained within a 20 cm^2 circular area clipped from raw point cloud at each DGPS location. The clipped area represents the space occupied by the DGPS target and receiver. Units are cm above ellipsoid.

Site	*No. of Points*	*Lowest HAE*	*2010 DGPS*	*Difference DGPS - LIDAR*
341	419	123.1	121.0	-2.1
342	44	143.5	136.2	-7.3
343	27	142.3	140.6	-1.7
344	61	120.6	117.3	-3.3
345	27	142.3	144.4	2.1
371	250	133.9	129.3	-4.6
372	92	137.4	129.8	-7.6
373	465	146.0	145.3	-0.7
374	42	147.7	140.7	-7
375	31	155.2	152.6	-2.6
401	61	152.9	149.5	-3.4
402	74	159.7	156.8	-2.9
403	24	165.7	161.8	-3.9
404	63	167.7	No Data	---
405	35	161.6	155.7	-5.9
441	660	185.5	187.1	1.6
442	5	190.9	183.2	-7.7
443	39	191.1	No Data	---
444	23	199.4	198.1	-1.3
445	33	190.8	187.9	-2.9

Table 6. Residual statistics between the DGPS sites and the LIDAR point cloud. Units are cm above ellipsoid.

	DGPS – LIDAR (cm)
No. of Points	18
Minimum Residual	0.7
Maximum Residual	7.7
MBE	-3.4
MAE	3.8
SD	2.3
RMSE	4.4

The density image in Figure 20 shows the study area including locations of the CRREL plots and frost boils.

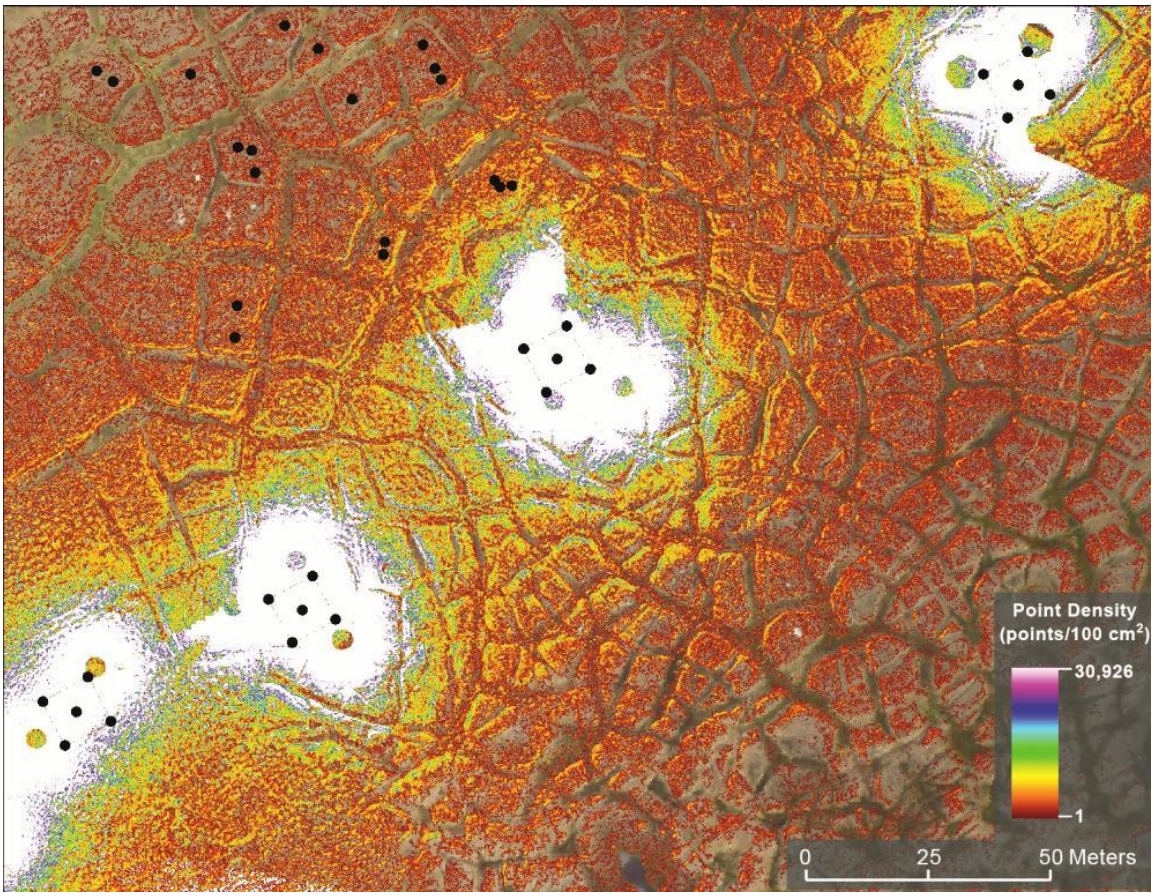

Figure 201. Point density of the entire original LIDAR point cloud, expressed as number of points per 10 cm^2. Study plots are demarcated with dashed lines with black dots representing the locations of DGPS measurements. Point density decreases dramatically within 20 m of the scanner.

As evident in the LIDAR density image, point density decreases dramatically with distance from the scanner, and analysis of the point cloud at the frost boil sites revealed no data points recorded within a 2.5 cm radius of 14 of the 20 sites, while five out of the remaining six sites registered only one point. Differences between the LIDAR point values and the corresponding DGPS measurements at the frost boil sites ranged from 1.2-9.3 cm (Table 7).

Because this analysis revealed minimal LIDAR coverage at the frost boil sites, they were not used for further analysis.

Table 7. Frost boil sites clipped from LIDAR point cloud. Units are cm above ellipsoid.

Site	*Points*	*Lowest HAE*	*2010 DGPS*	*Difference DGPS - LIDAR*
FB_9	1	167.4	164.7	-2.7
FB_12	1	169.4	170.6	1.2
FB_19	1	164.8	156.1	-8.7
FB_27	1	155.7	152.2	-3.5
FB_35	1	173.2	163.9	-9.3
FB_39	3	176.8	174.8	-2
All other (14 sites)	No Data			

Significantly higher LIDAR point density was registered within each of the four CRREL plots (Figure 21). Local point densities ranged from 0-5,505 points/100cm^2 within the plots, and decreased with increasing distance from the scanner, which was compensated for by scanning each site from multiple positions. However, some of the scan sites were positioned too close to the plot and caused noticeable data voids in the ~2 m radius around the scanner (observable in C34, C37, and C44). Point density was so high within most of the CRREL plots that it appeared sufficient to capture topography even within the polygon troughs. Mean point densities for the four plots ranged from 332-360 points/100cm^2. The only topographic feature observable in the 10 cm resolution density images is the trough that cuts horizontally across plot C40.

Examining point density at a finer resolution (1 cm^2) revealed even more detail in the LIDAR point cloud (Figure 22). Local densities ranged from 0-522 points/cm^2 with average densities of 3-4 points/cm^2. While the density still appears minimally affected by

terrain variation at this resolution, one feature that is absent in the 10 cm density image but visible in the 1 cm image are small streaks (data voids) emanating from behind the wooden posts to mark the site boundaries, a phenomenon known as “flagging” (Carl Sielstad, pers. comm., 8 February 2013). These artifacts do not appear to affect point density at resolutions coarser than 1 cm, but could explain potential inconsistencies in very high resolution DEMs produced from this kind of data.

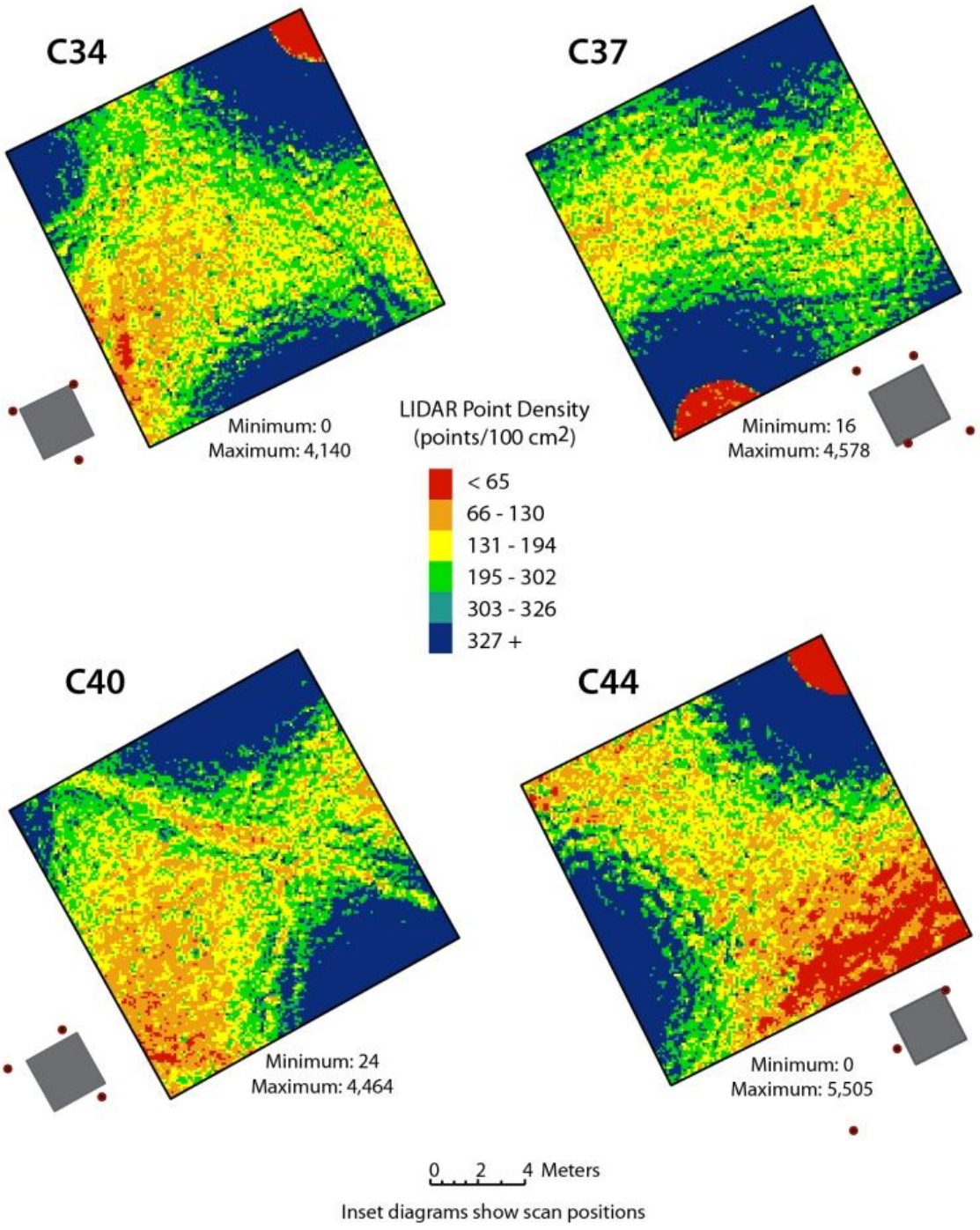

Figure 21. Point density maps of each of the four study plots. Density is expressed as number of points per 10 cm^2. The highest point density recorded in the plots was 5,305 points/10 cm^2. Inset diagrams show the relative locations of the scanner around each plot. Point density noticeably decreased with increasing distance from the scanner.

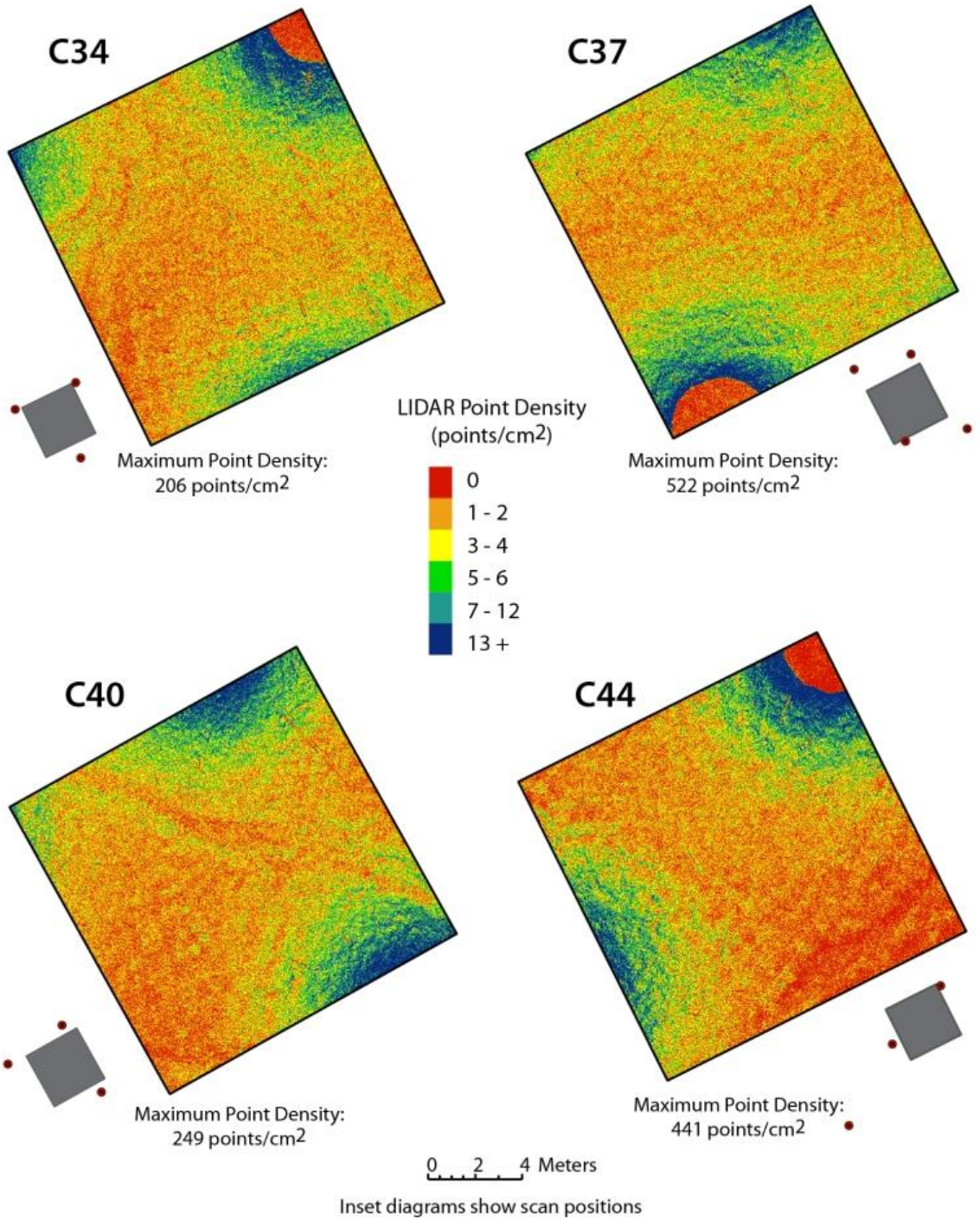

Figure 22. Point density maps of each of the four study plots. Density is expressed as number of points per 1 cm^2. The highest point density recorded in the plots was 522 points/cm^2. Flagging due to obstruction by the wooden posts used to demarcate the active layer sapling grid (Figure 10) can be seen to some degree in all plots at this resolution. Inset diagrams show the relative locations of the scanner around each plot.

Maps of LIDAR intensity for each plot are presented in Figure 23. Because intensity values are acquired using a variable grain, the values are not calibrated unless careful post-processing is performed (Evans 2009). The intensity values for this LIDAR dataset were delivered as raw, non-calibrated values and revealed little about the ground surface cover of the plots.

Visual analysis of the LIDAR intensity images revealed similar spatial patterns as found the density images. Intensity values ranged from 0-4,277, with average intensities of 3,422-3,516 in the four study plots. There is some streaking visible in the intensity images, which is qualitatively different than the "flagging" in the density images as it does not correspond to the location of the posts. Rather, the streaking pattern appears to emanate radially from each scanner position. The exact cause of the streaking pattern could not be determined, even with detailed investigation into the DEMs interpolated from this data (Section 5.2).

The only plot that showed variations in intensity values that appear to potentially correspond to changes in vegetation cover was C34, where the darker green blue values of high intensity occurred in roughly the same area as the wet graminoid vegetation that dominated the polygon troughs. However, with uncalibrated values it was not possible to differentiate these areas of low intensity from the other high-intensity areas that buffer the scanner that do not appear to correspond well to particular ground cover types.

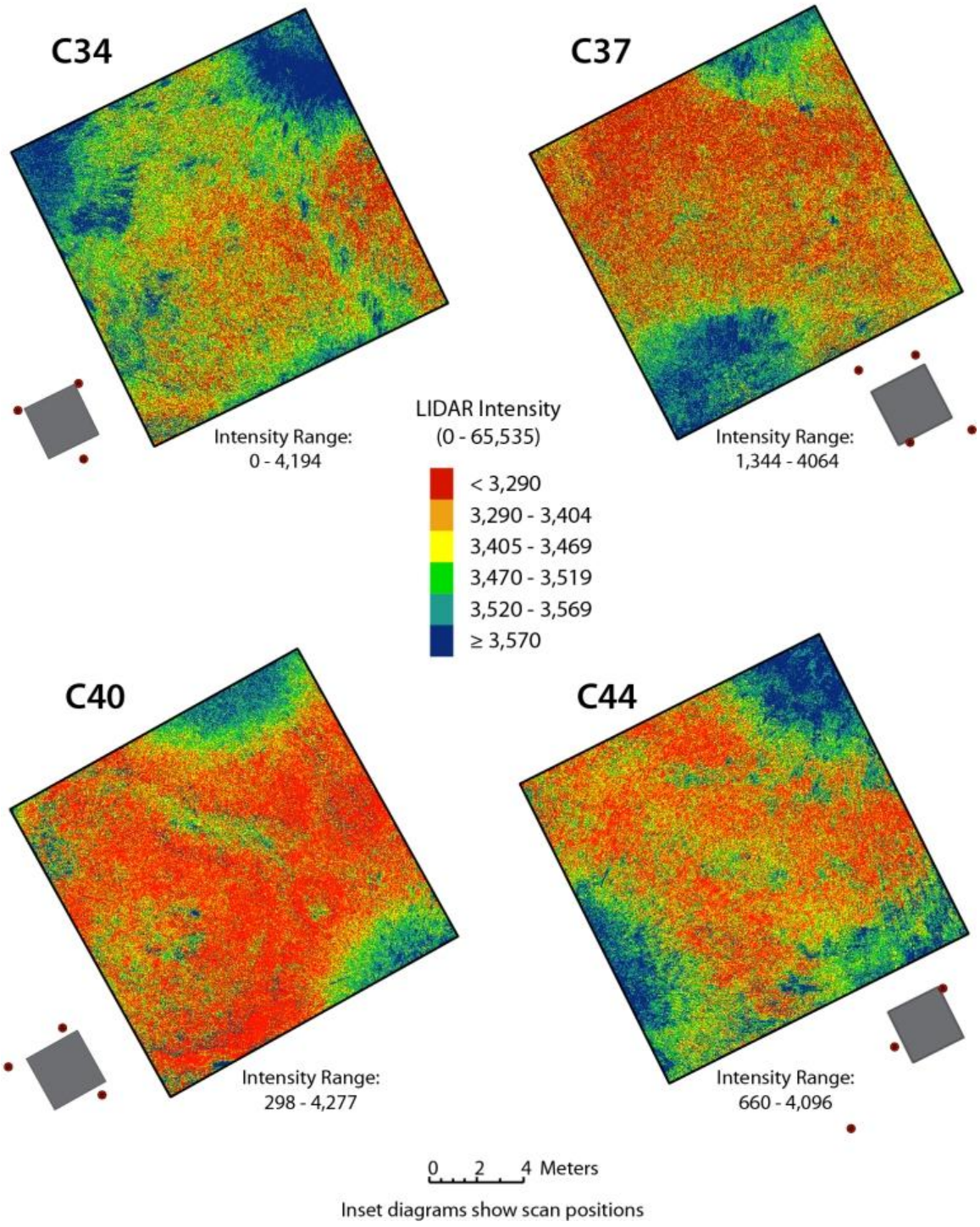

Figure 23. LIDAR intensity maps for each of the four study plots. Uncalibrated values ranged from a minimum of 0 (C34) to a maximum of 4,277 (C40). Intensity generally decreased with increased distance from the scanner. Inset diagrams show the relative locations of the scanner around each plot.

5.2 DEM Interpolation

Interpolation of high-resolution DEMs from the LIDAR point cloud was complicated by streaking anomalies present in the point cloud (described in Section 5.1 and visible to a lesser degree in Figure 23), not the "flagging" caused by the wooden stakes on the perimeter of each plot. This "streaking" resulted in the interpolation of a series of small artificial ridges and troughs in the DEM that radiated from each scan position. These streaks were visible in DEMs created from thinned out point clouds to 1, 2, and 5 cm resolution (retaining only the lowest point within each cell as described in Section 4.2.1) and no longer visible when the input data were thinned to 10 cm resolution (Figure 24). Elevation profile graphs generated from multiple transects across plot C34 (Figure 25) revealed that the streaks were ~2-5 cm in height and did not vary based on the height of the vegetation, which is generally taller in the troughs. They are also clearly not related to trails formed by lemming's movements near their burrows as those have a distinct, recognizable structure.

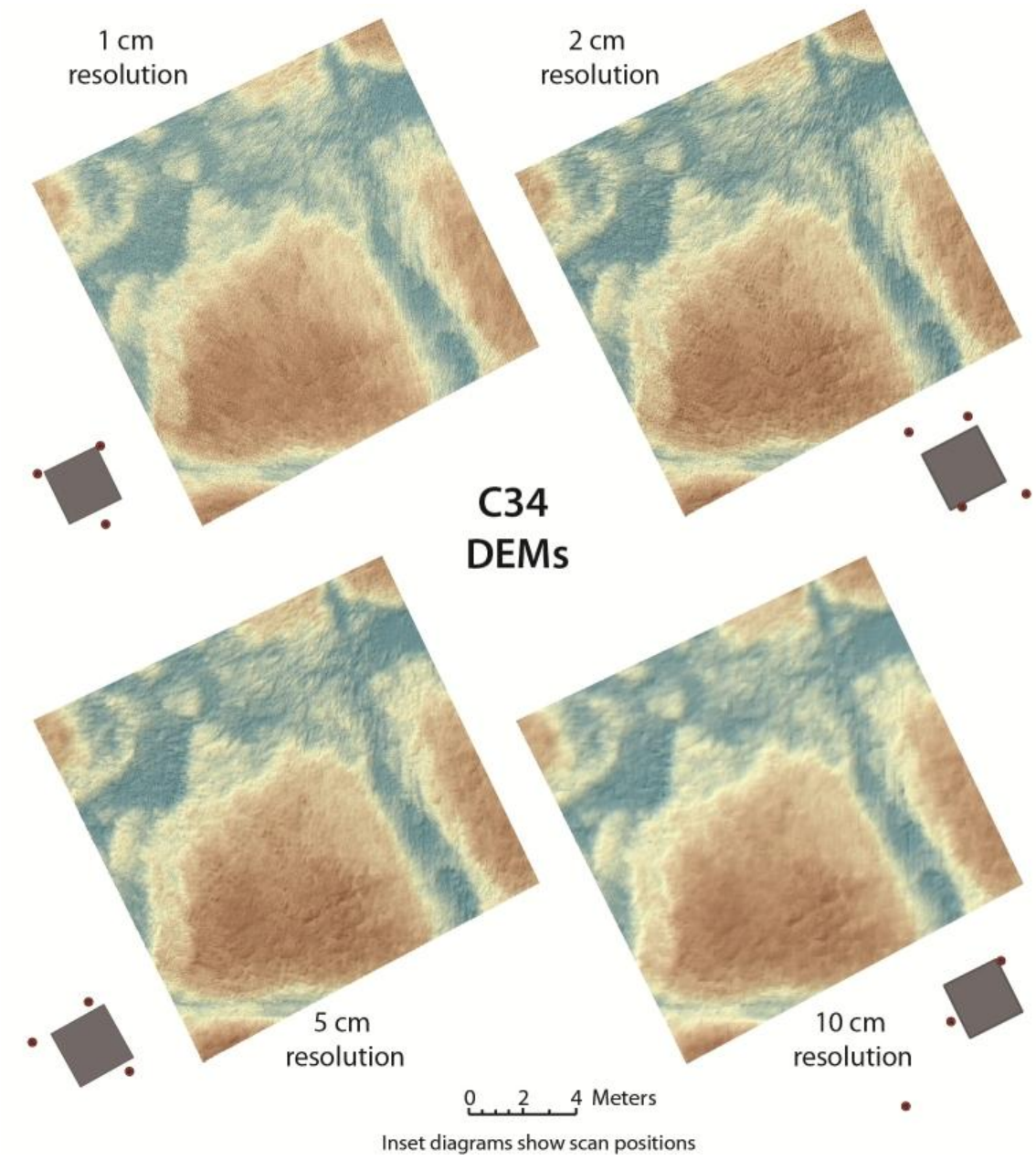

Figure 24. DEMs for plot C34 generated from point clouds thinned out to resolutions of 1, 2, 5, and 10 cm. Thinned point clouds were made by taking the lowest point in each grid cell of specified size. Steaks in the LIDAR data manifested as small ridges on the DEM can be seen clearly in the 1, 2, and 5 cm DEMs and to a lesser extent in the 10 cm DEM, where they appear somewhat smoothed out. Inset diagrams show scanner positions

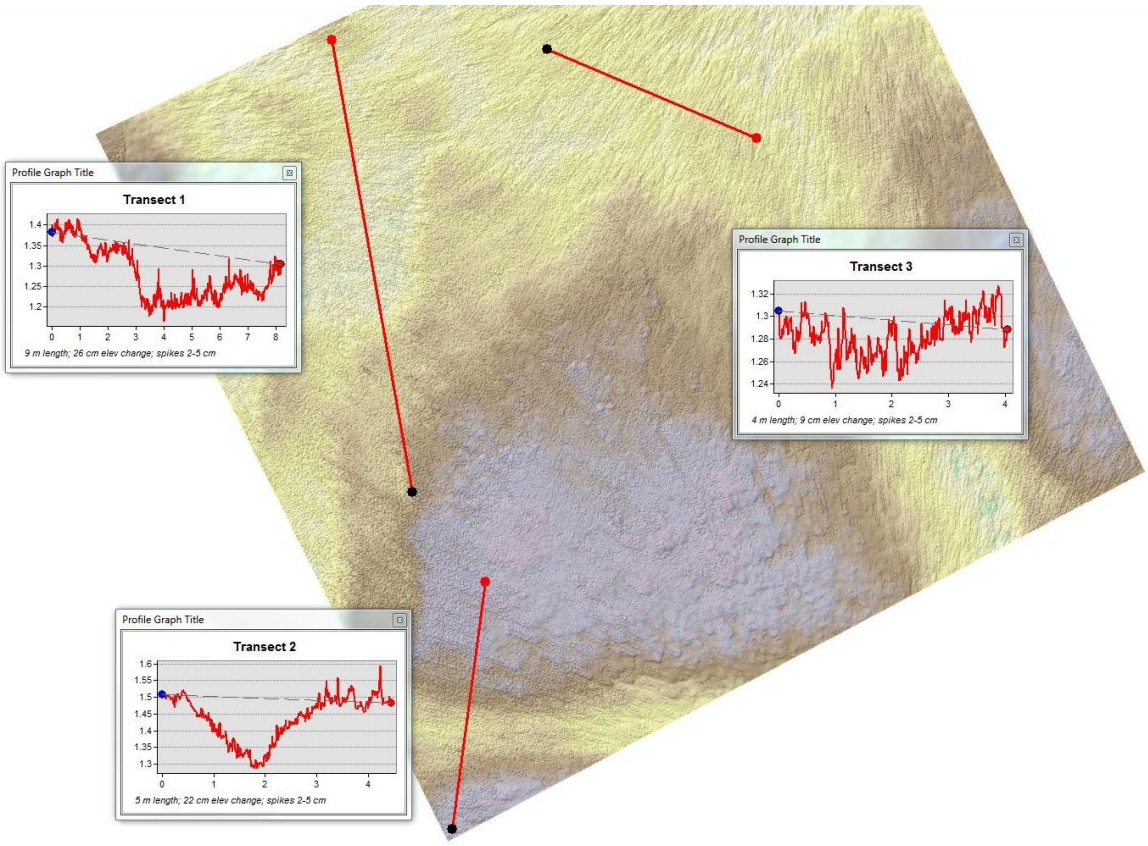

Figure 25. Elevation profile graphs for a variety of transects in plot C34. Profile graphs revealed that small ridges resulting from streaks in the original data were 2-5 cm and did not vary in magnitude between the polygon centers and troughs, even though vegetation is both denser and taller in the troughs.

Review of the literature produced no reasonable explanations of these streaks and no description of it occurring in other terrestrial LIDAR datasets. In terms of general sources of error, atmospheric conditions are often cited as potentially confounding factors in LIDAR collection (Fowler 2012); however, photographs taken during data acquisition suggest that there was minimal atmospheric disturbance (i.e. no fog or visible particulate matter) on any of the three collection days. Weather varied slightly – one of the days was clear and sunny while the other two were overcast – but this variable proved irrelevant since the streaking anomalies were consistent among all scans regardless of acquisition date.

In consultation with LIDAR professionals at UNAVCO, Overwatch[2], and the University of Montana, two other hypotheses were developed as possible explanations of the anomalies. One was that the streaking could be due to very minute changes in the scanner speed (John Gale, pers. comm., 14 December 2012), however, there was no way to test this without repeating the entire scan. The second hypothesis was that the laser might be intercepting individual blades of grass and creating a trail of multiple returns behind them out (Marianne Okal, pers. comm., 19 February 2013 and John Gale, pers. comm., 21 December 2012). If this were the case, it would be possible to eliminate much of the streaking if the data could be broken into multiple returns and some of the intermediate noise filtered (John Gale, pers. comm., 21 December 2012). However, in that case, one would expect the first return only data used here to have less streaking (Carl Seilstad, pers. comm., 4 February 2013).

Since discrete returns could not be exported from this dataset at the time of analysis, this hypothesis was investigated further by identifying areas of bare ground (in this case, unvegetated frost boils; Figure 26) in two plots and comparing a 1 m long elevation profile of those areas to

Figure 26. Raised, unvegetated frost boil, typical in appearance to those scattered throughout the study area (Photo: Anna Klene).

[2] Overwatch Systems, Ltd. Austin, TX

1 m profiles of surrounding vegetated areas. If the streaking were the due to vegetation occlusions, then they should be less prominent on unvegetated ground. However, analysis on two different plots revealed that the elevation spikes were present in roughly the same magnitude on bare ground compared to vegetated areas (Figure 27).

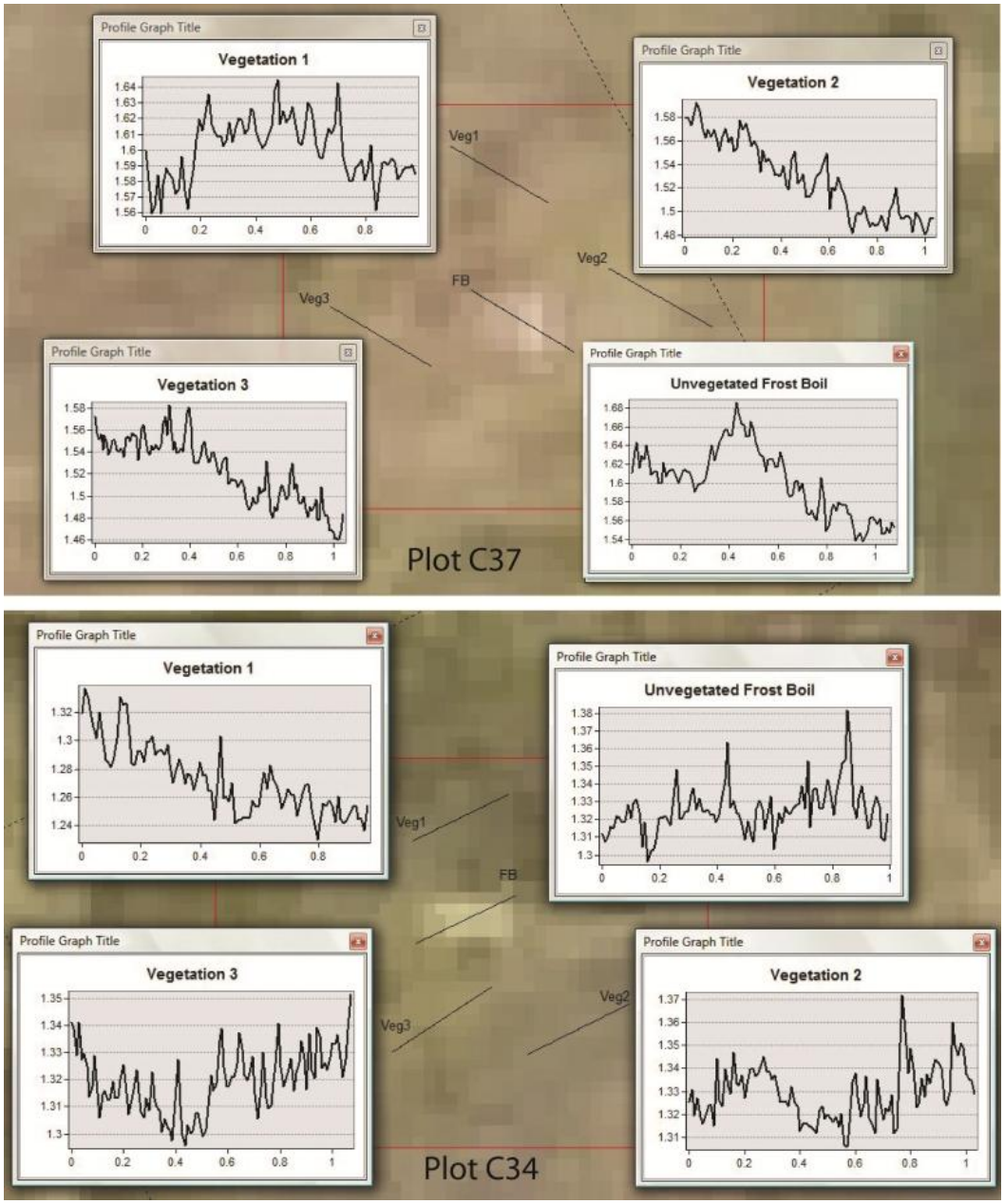

Figure 27. Elevation profile graphs comparing vegetated areas to unvegetated frost boils overlain on the aerial imagery of plots 34 and 37. Streaks in the data manifested as ridges on the DEMs were not affected by the presence or absence of vegetation, presenting in the same patterns (~2-5 cm in height) on both vegetated and unvegetated ground.

5.3 DEM Analysis

Since the cause of the streaking in the point cloud could not be ascertained and removed, the four variations of the original point cloud (thinned out to 1, 2, 5, and 10 cm resolutions) were used to create a selection of DEMs using the three LIDAR software tools described in Section 4.2.1. Experimentation with every available option within each software tool produced over 100 variations of DEM for test site C34. Each DEM was clipped and compared to the 5 DGPS measurements within that plot, and the five best-performing algorithms were applied to the other sites and analyzed utilizing the complete set of 18 DGPS points. Since manipulation of the various options within each tool was not found to significantly alter the resulting DEM, all of the tools were run with their default settings (interpolation based on elevation, no automatic filling of holes in data, filtered by all returns, output raster properties set from input LAS file) to produce the five final sets of DEMs. The best performing interpolation compared to the DGPS data was subsequently tested for accuracy using the LIDAR control points withheld from the original point cloud (Section 4.2.2)

5.3.1 Assessment with DGPS Data

Analysis revealed two DGPS points which were consistently outliers when compared to the DEMs produced from the thinned out point clouds: C344, which returned DEM values that were 20-30 cm *above* the measured DGPS heights; and C345, which returned DEM values that were consistently 20-25 cm *below* the DGPS measurements. These rather large discrepancies were present in all of the DEMs, regardless of resolution of the DEM and/or interpolation algorithm. The underlying cause of these outliers could not be determined, as the original LIDAR point cloud

(Table 5) showed no significant divergences when compared to the DGPS heights at these points and examination of the 10-year DGPS dataset showed that the measured DGPS heights were fairly consistent with those for previous years. Removal of these two points from error calculations significantly improved results, particularly with respect to absolute error. Error analyses for all five sets of DEMs, with and without outliers, are presented in Table 8 and 9.

Table 8. Differences between DGPS height measurements and LIDAR-derived DEM elevations, (DGPS-DEM) expressed as Mean Bias Error (MBE) and Mean Absolute Error (MAE). The DEM-generation software and tool is indicated: LAStools® blast2dem, LIDAR Analyst® LAS file to Raster with Filtering, and LIDAR Analyst® Extract Bare Earth All values are cm above ellipsoid.

DEM	*MBE*	*SD*	*MAE*	*SD*
10 cm resolution (LAS to Raster)	-2.8	8.5	5.7	6.9
10 cm resolution (LAStools)	-3.0	8.4	5.9	6.7
10 cm resolution (Bare Earth)	-3.1	8.3	5.8	6.7
5 cm resolution (LAStools)	-3.5	8.4	6.2	6.6
5 cm resolution (Bare Earth)	-3.6	8.3	6.3	6.5

Table 9. Differences as in Table 8, but for the remaining 16 DGPS points after the 2 outliers were removed.

DEM	*MBE*	*SD*	*MAE*	*SD*
10 cm resolution (LAS to Raster)	-3.0	2.7	3.3	2.2
10 cm resolution (LAStools)	-3.2	2.7	3.6	2.2
10 cm resolution (Bare Earth)	-3.2	2.8	3.6	2.3
5 cm resolution (LAStools)	-3.8	2.7	4.1	2.3
5 cm resolution (Bare Earth)	-3.8	2.7	4.2	2.2

The 10 cm DEM produced by the LAS to Raster tool within LIDAR Analyst® was selected for use in all further analysis of this study because of its small error values and low standard deviations. However, none of the software tools utilized had mean

errors that were more than 1 cm different than the best performing one and none had errors over 5 cm from the mean, excluding outliers (unpublished data).

The four DEMs for the CRREL plots are displayed (Figure 28) using color ramps stretched over the heights of each plot. An attempt was made to display all the DEMs using consistent minimum and maximum values, but the difference between the mean elevations of plots C34 and C44 made it difficult to display the microtopographical variation (Figure 29). However, that emphasizes the magnitude of the underlying elevational gradient in context of scale of microtopography of the plots.

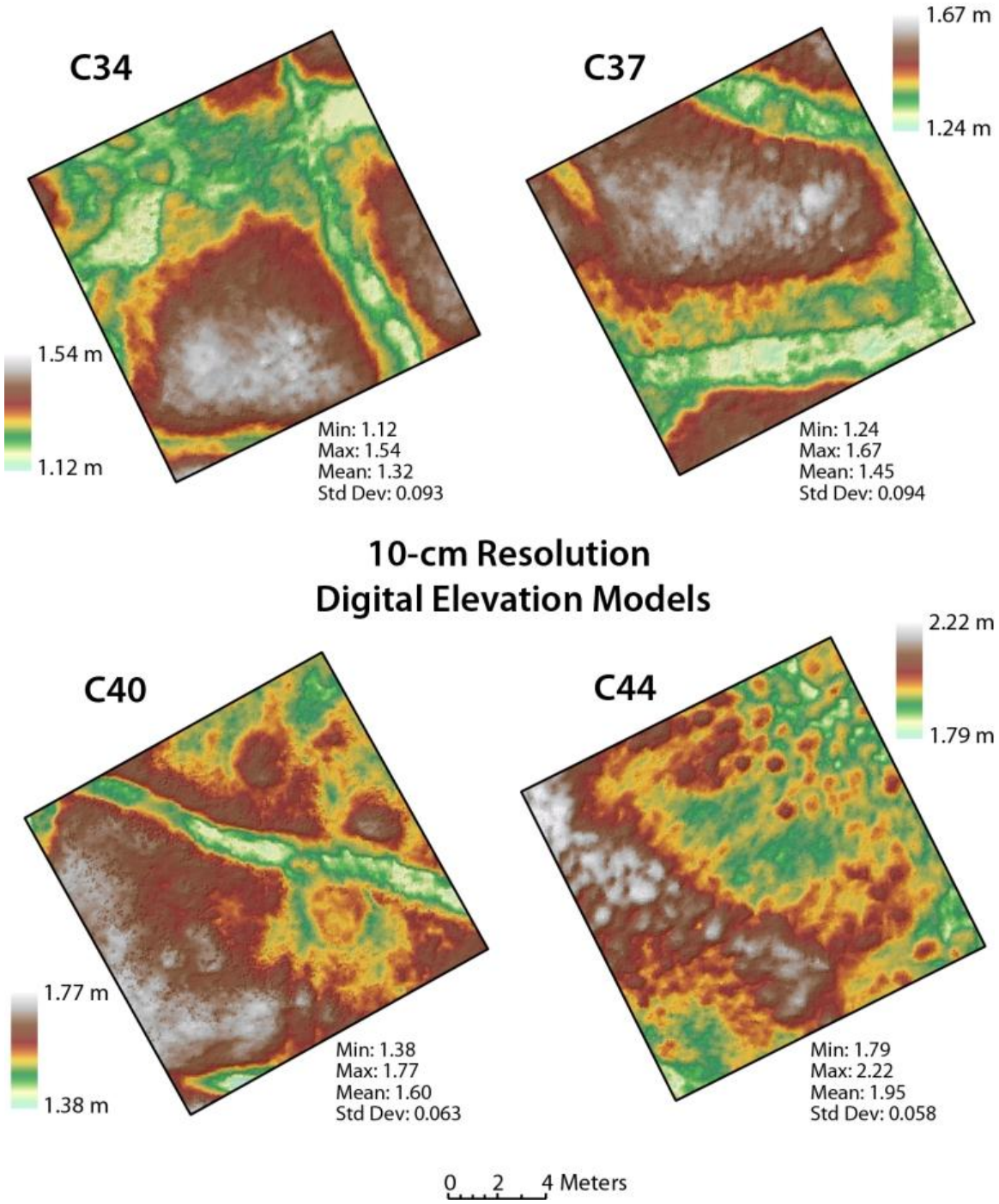

Figure 28. Final digital elevation models (DEMs) for each of the four study plots using color ramps stretched over the range of elevations within each plot.

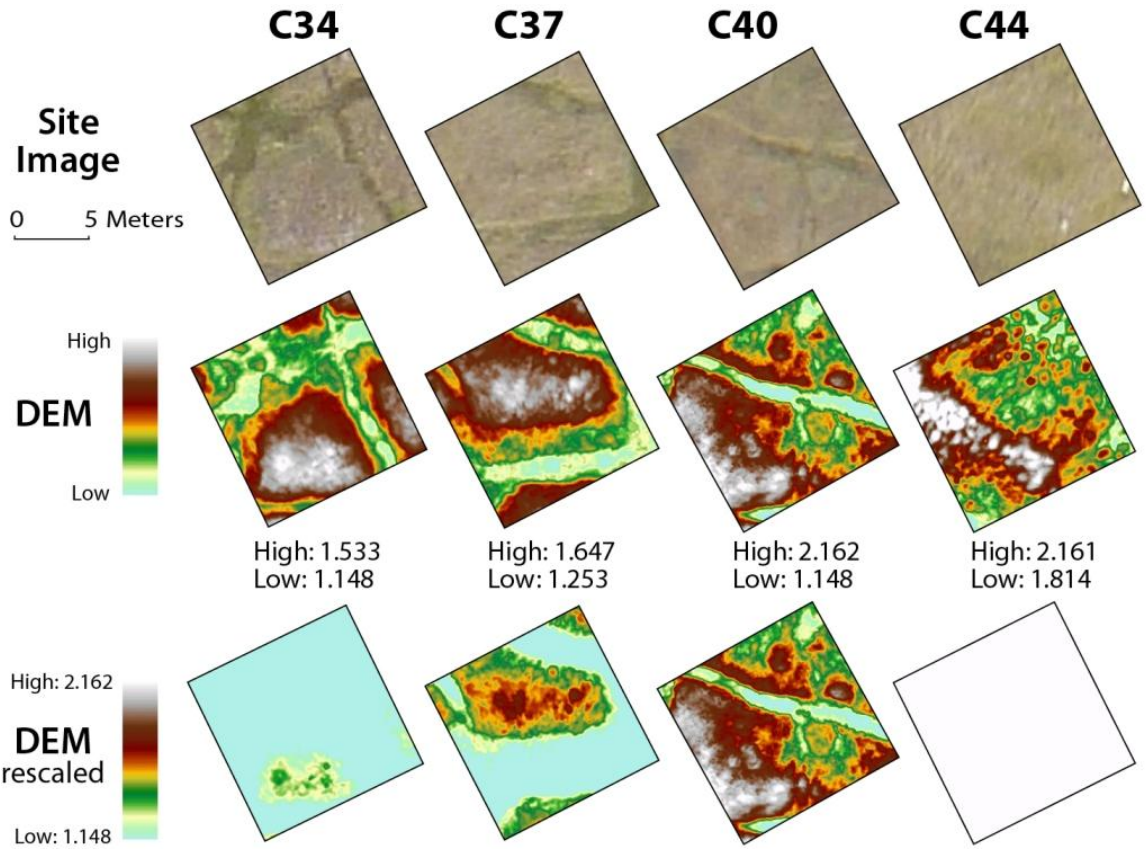

Figure 292. DEMs for each study plot, symbolized first based only on the range of values present in the individual plot and second based upon the entire range of values between all four plots. Most of the microtopographical relief in plot C34 (the lowest) and C44 (the highest) is lost in the second symbolization due to overall elevation differences. Aerial photos of each plot are shown for reference.

That the coarsest DEM generated from the most thinned LIDAR point cloud yielded the best statistical performance compared to the measured DGPS points reveals a great deal about the limitations and drawbacks of ultra-high-resolution terrestrial LIDAR data. Table 10 shows a comparison of the original point cloud for each plot and the thinned point cloud used to create the most accurate DEM. Only ~0.3% of the data points available for each plot was used to interpolate the final DEM.

Table 10. Summary of the original AOI point clouds and the 10 cm-resolution thinned point clouds used to derive the best performing DEMs.

	C34		*C37*		*C40*		*C44*	
	Original	10 cm	Original	10 cm	Original	10 cm	Original	10 cm
No. of points	7,303,671	21,128	7,872,785	20,866	7,370,668	20,382	6,981,650	21,209
Min (m)	1.109	1.106	1.242	1.242	1.383	1.383	1.786	1.786
Max (m)	1.928	1.543	2.378	1.656	2.528	1.786	2.616	2.224
Range (m)	0.822	0.437	1.136	0.414	1.145	0.403	0.83	0.438

To investigate interpolation errors, the heights of the DEM at the DGPS locations were compared to the heights determined through direct analysis of the LIDAR point cloud at those same locations (Section 5.1). Scatterplots of the original, complete LIDAR point cloud vs. DGPS measurements (presented earlier in Table 5) and the DGPS measurements vs. DEM elevations (Figure 30) revealed that the raw LIDAR point cloud was more accurate in predicting the DGPS height and showed that some of the original

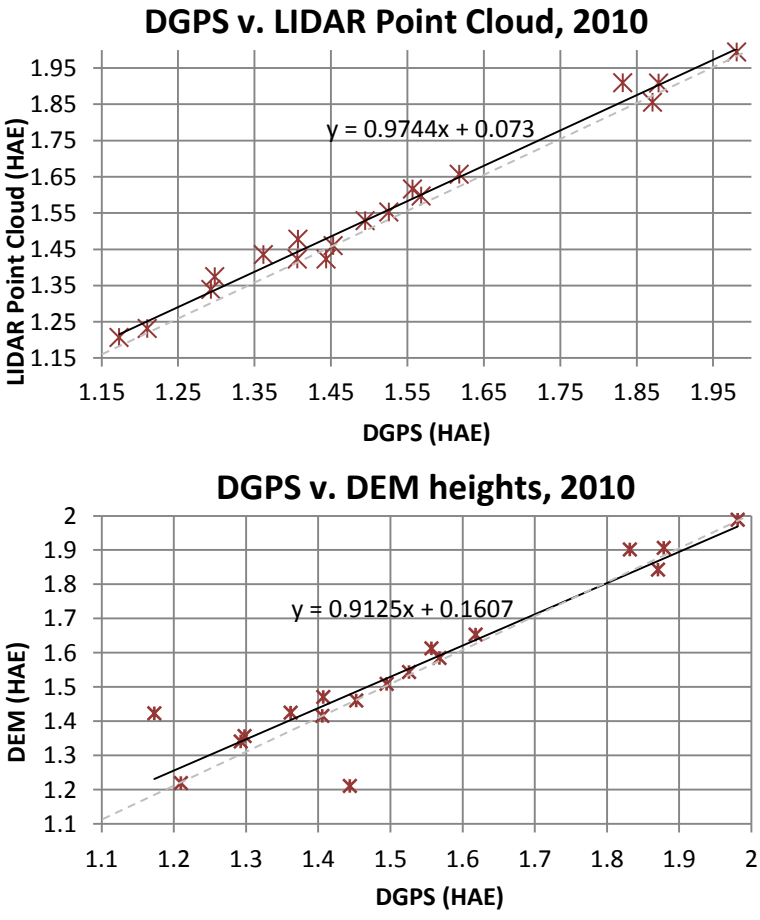

Figure 30. Comparison of the accuracy of the both the LIDAR point cloud data and the derived DEM using in situ DGPS data as ground truth. All elevations are given as height above ellipsoid (HAE) in meters.

accuracy of the LIDAR data was indeed lost in DEM interpolation, as expected; however, the difference in performance between the two datasets was quite small

Comparisons of the DGPS measurements to the final DEMs produced an RMSE of 8.9 cm and an MAE of 5.7 cm (Table 11). The size of these errors was due in large part to the two outliers discussed in earlier in this section. Removal of the outlying points reduced MAE by more than a third (to 3.3 cm) and RMSE to less than half (4.0 cm).

Table 11. Summary statistics for the comparison of DEM elevations to DGPS measurements. All units are cm above ellipsoid.

Number of Points	18		16 (outliers removed)	
	DGPS	*DEM*	*DGPS*	*DEM*
Minimum Value	117.3	121.1	121.0	122.0
Maximum Value	198.1	198.9	198.1	198.9
Range	80.8	77.8	77.1	76.9
Mean	152.1	154.8	154.7	157.7
Standard Deviation	23.0	22.6	22.6	22.0
RMSE	8.9		4.0	
MBE	-2.8		-3.0	
MAE	5.7		3.3	

5.3.2 Assessment with LIDAR Control Points

Comparisons of the control points withheld from the LIDAR cloud (50 cm lowest point as described in Section 4.2.2) to the derived DEMs revealed RMSE values of ≤ 0.3 cm for all DEMs (Table 12). Interpolated elevations were consistently higher on the DEM than in the control dataset, as indicated by the negative MBE values for all plots. Mean average error (residuals) ranged from 0.1-0.2 cm, with an overall MAE of

0.13 cm for all four DEMs. Scatterplots of these two datasets (Figure 31) illustrate the tight correlation between them at all four CRREL plots.

Table 12. Summary statistics comparing the lowest LIDAR point within each 50 cm cell to the DEM elevations (LIDAR-DEM). All units are cm above ellipsoid.

Plot	*C34*		*C37*		*C40*		*C44*	
	LIDAR	*DEM*	*LIDAR*	*DEM*	*LIDAR*	*DEM*	*LIDAR*	*DEM*
Minimum Value	110.6	111.7	124.2	124.6	138.3	138.4	178.6	178.9
Maximum Value	149.9	149.9	161.2	161.3	172.1	172.0	211.4	211.8
Range	39.3	38.2	37.0	36.7	33.8	33.6	32.8	32.9
Average	129.6	129.7	142.3	142.4	157.0	157.2	192.4	192.5
Standard Deviation	9.5	9.5	9.5	9.5	6.4	6.4	5.4	5.4
RMSE	0.2		0.2		0.3		0.2	
MBE	-0.1		-0.1		-0.2		-0.1	
MAE	0.1		0.1		0.2		0.1	
Number of Points	898		891		869		899	

.

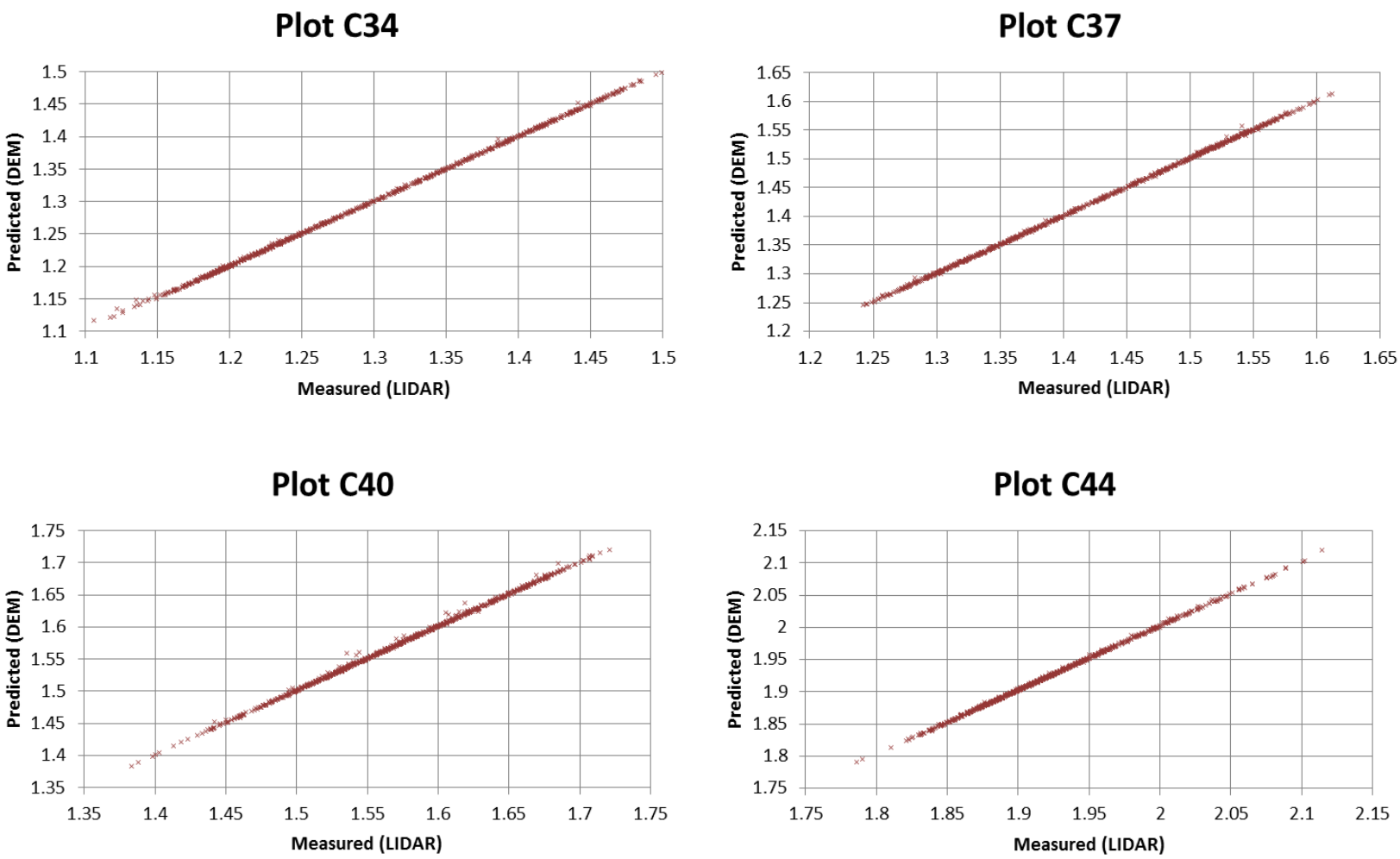

Figure 31. Scatterplots comparing the interpolated heights of the DEMs to the actual heights of the withheld LIDAR control points for each plot, showing strong correlation between the two datasets. All values represent heights above ellipsoid in meters.

Mapping of the residuals (Figure 32) revealed no spatial trends in error between the LIDAR control points and the DEM, despite spatial differences in the original data quality around the individual scan sites (Figure 21 and Figure 22) and the microtopography. Figure 33 is a binary map illustrating only those points where the absolute value of the residual was >1 cm.

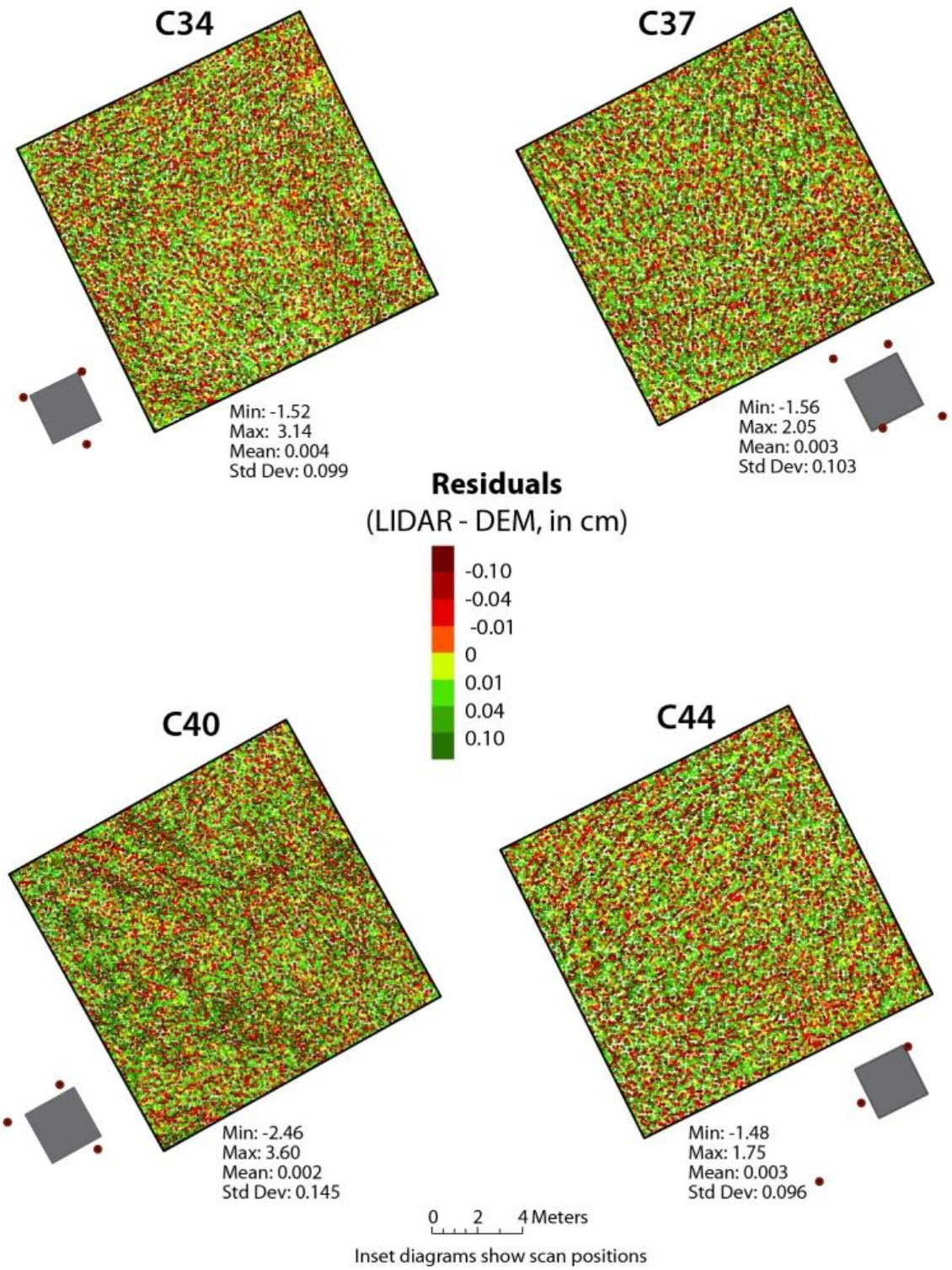

Figure 32. Residual maps for each of the four plots. Red points represent locations where the heights of the original LIDAR data were below those of the interpolated DEM; green points represent locations where the LIDAR heights were above those of the DEM. Average residual values for all plots were less than 0.1 cm.

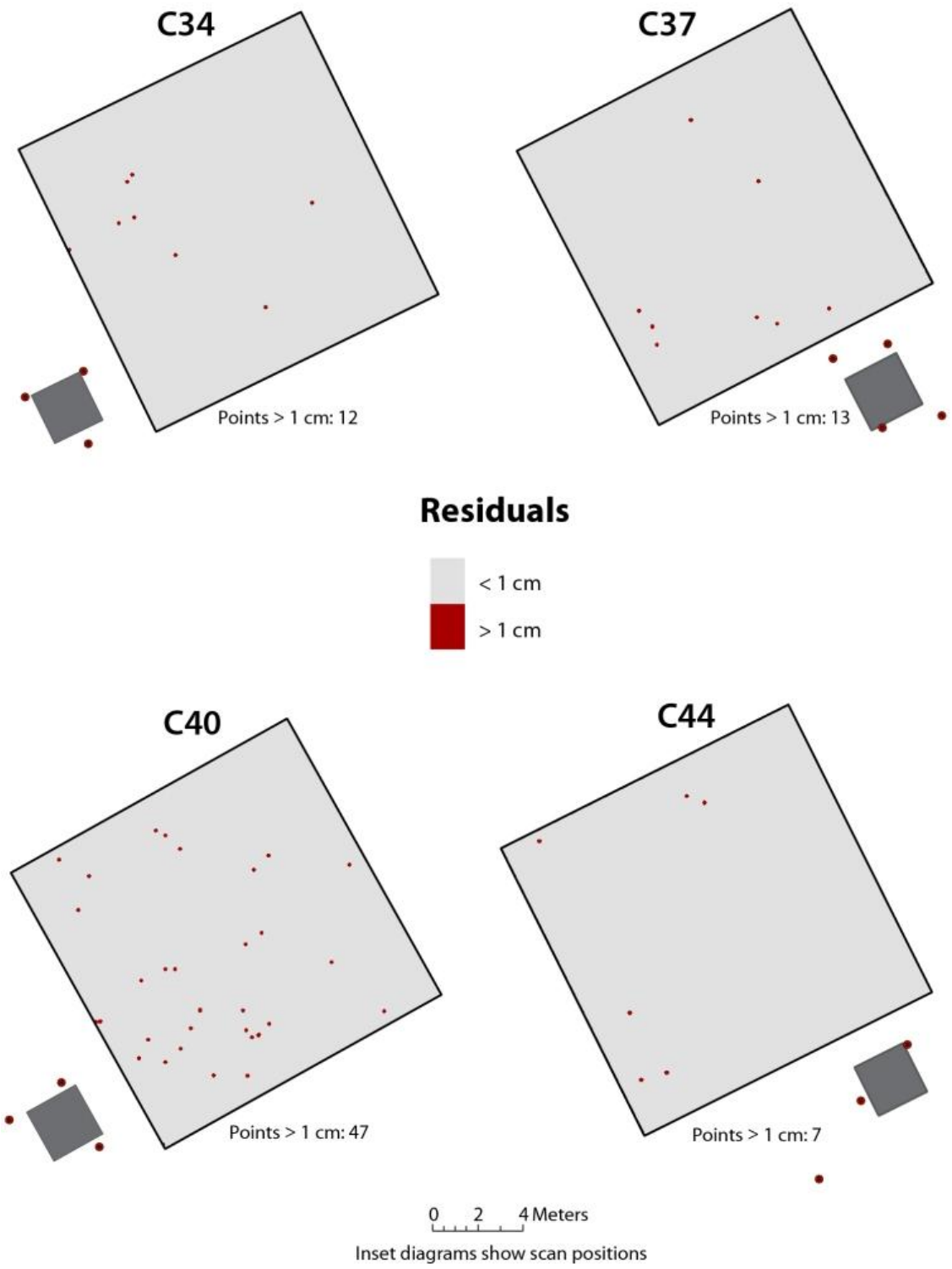

Figure 33. Simplified residual maps for each plot, showing only those points where residual values were greater than 1 cm (in red)

5.4 Microtopography Classification

Calculations of surface variable and topographic indices yielded mixed results. Maps of each surface calculation described in Section 4.3 at the optimal resolution listed in Table 3 for plot C34 are presented in Figure 34 and Figure 35.

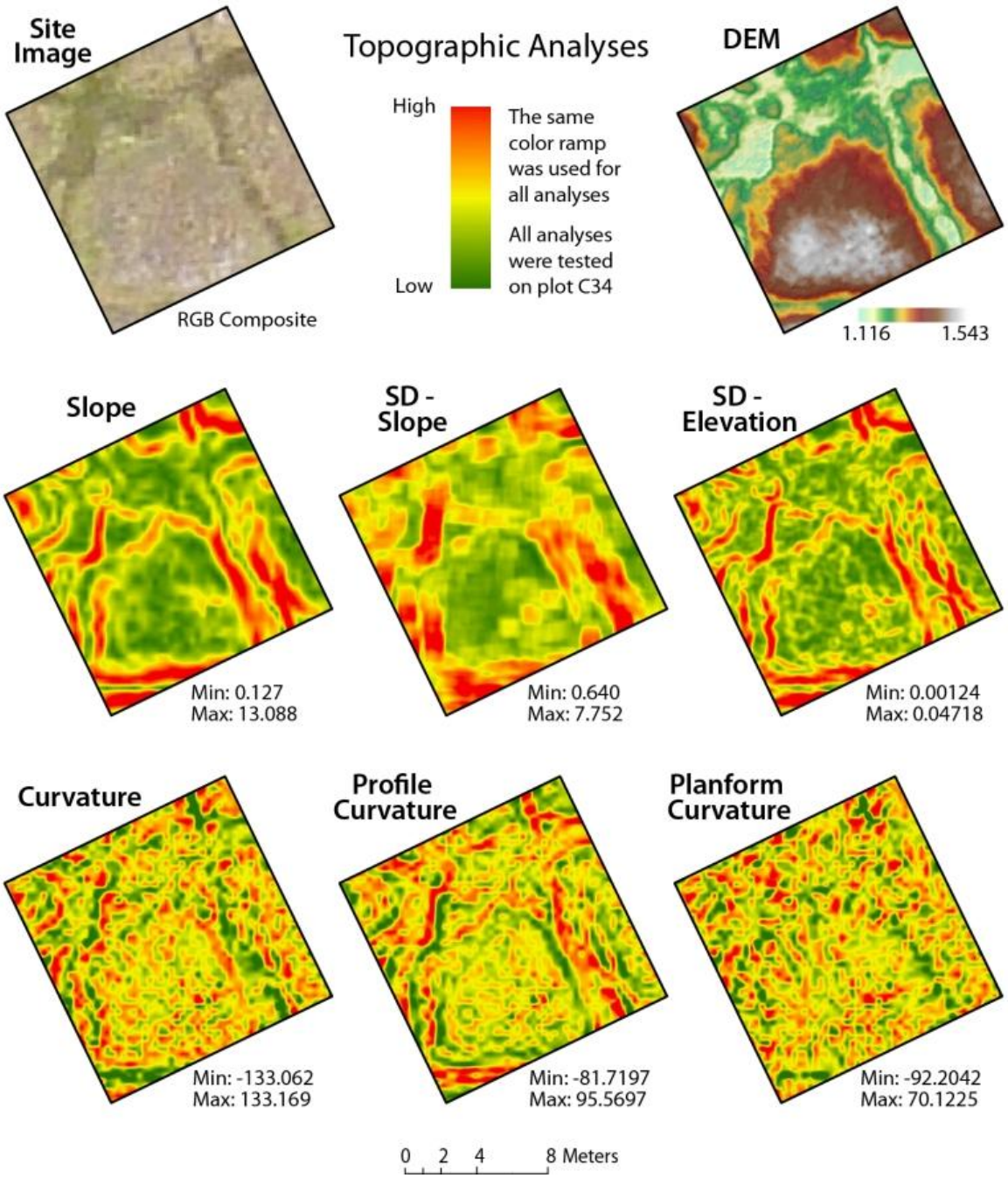

Figure 34. Surface derivative maps for plot C34. Red areas indicate higher values where there is greater variation in terrain surface. The aerial photo and DEM for plot C34 are provided for reference. Input specifications, including resolution and cell neighborhood size, used to create each map can be found in Table 3.

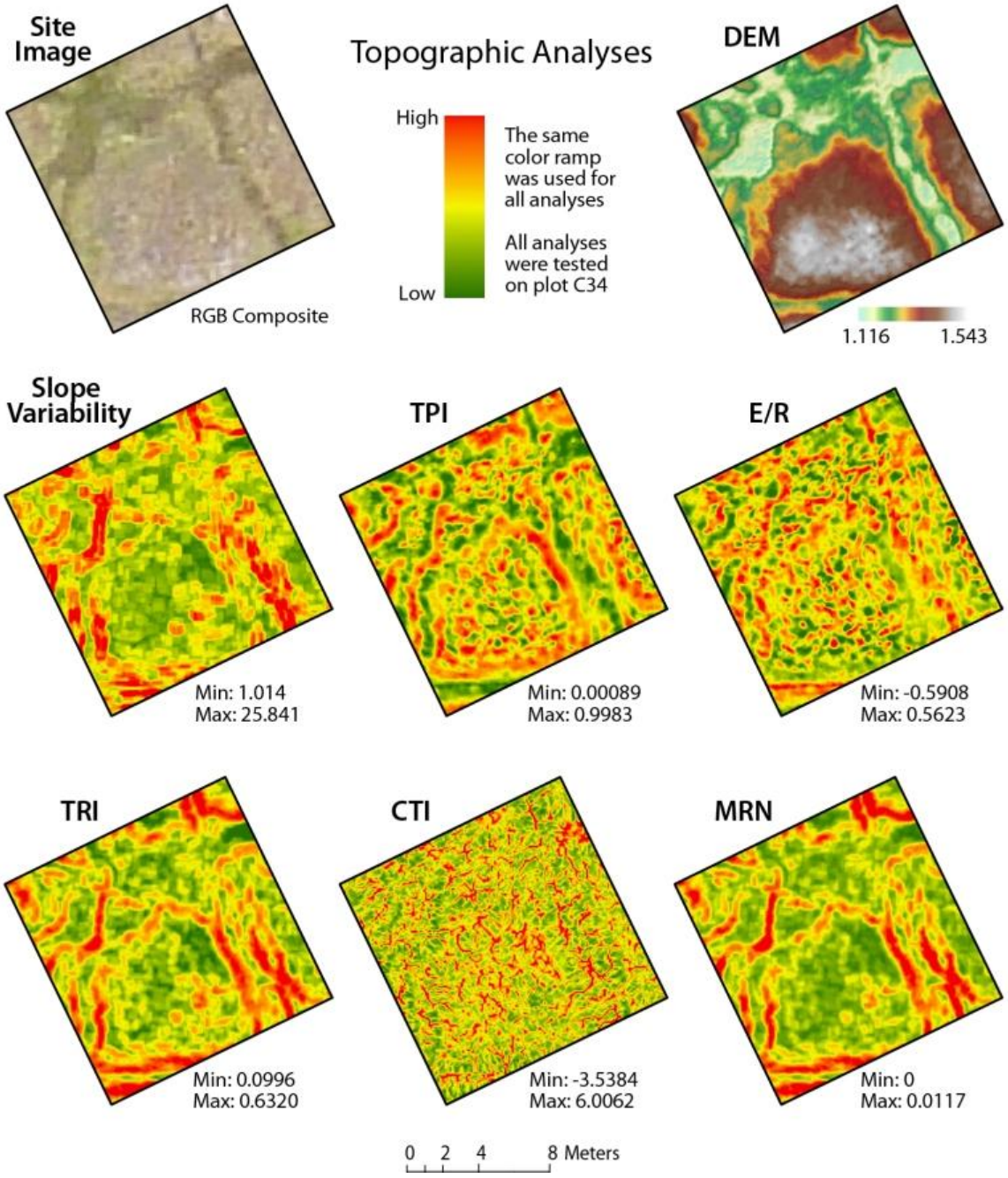

Figure 35. Topographic index maps for plot C34. Red areas indicate higher values where there is greater variation in terrain surface. Input specifications, including optimal resolution and cell neighborhood size, used to create each map can be found in Table 3.

Most of the topographic indices (TPI, E/R, CTI), and all second derivatives of the surface quantified the variability of the terrain ways that were visually confusing, even at coarse resolution, and ultimately not used for general classification. First derivatives of surface provided a better general picture of variability, but had to be reduced to a much coarser resolution to achieve this. Of the topographic indices, the TRI and MRN both quantified the local surface variability observed in the DEM at a slightly higher resolution than the first derivatives of surface because they could be successfully calculated on higher resolution input DEMs without the results becoming too visually confusing for rudimentary classification, as was the case with the slope calculated at higher resolutions.

The derivation of the final terrain raster used to classify the polygon sides is shown for each plot in Figure 36. Plot C44 showed the least microtopographical variation, which was expected given its location atop the beach ridge, which is slightly elevated and more uniform than the polygonal lowlands.

Figure 37 illustrates the derivation of the integer rasters for elevation (from the DEM) and terrain (from the final raster in Figure 36) that were used in the final microtopography classification. Figure 38 illustrates the final overlays of that process and presents the classified maps for each plot which were described in Section 4.3.

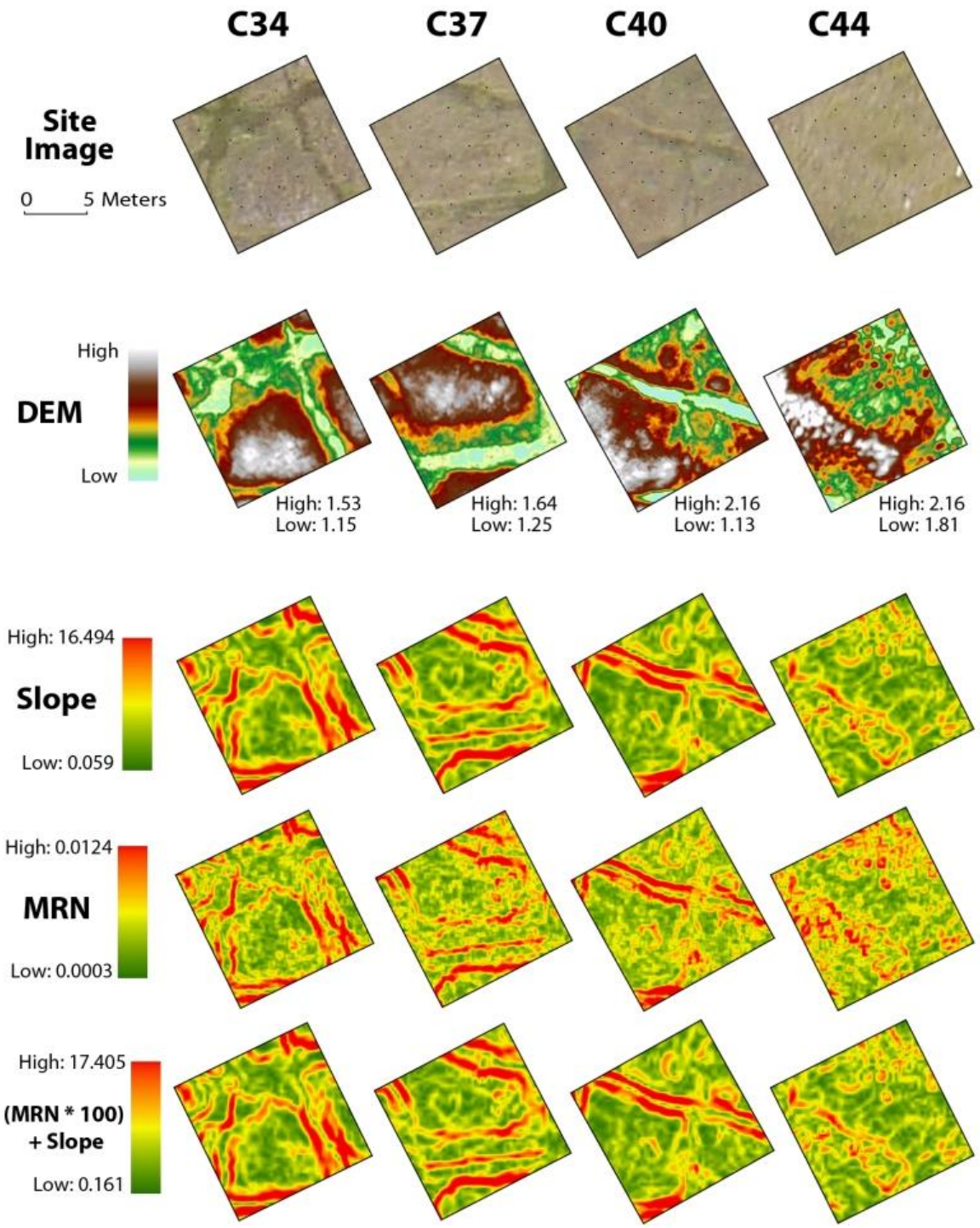

Figure 36. Maps of the final terrain calculations used in the microtopographical classification of the DEMs. The calculated layers for each plot are all symbolized with the same color ramp stretched to the same values in order to facilitate accurate visual comparison between plots.

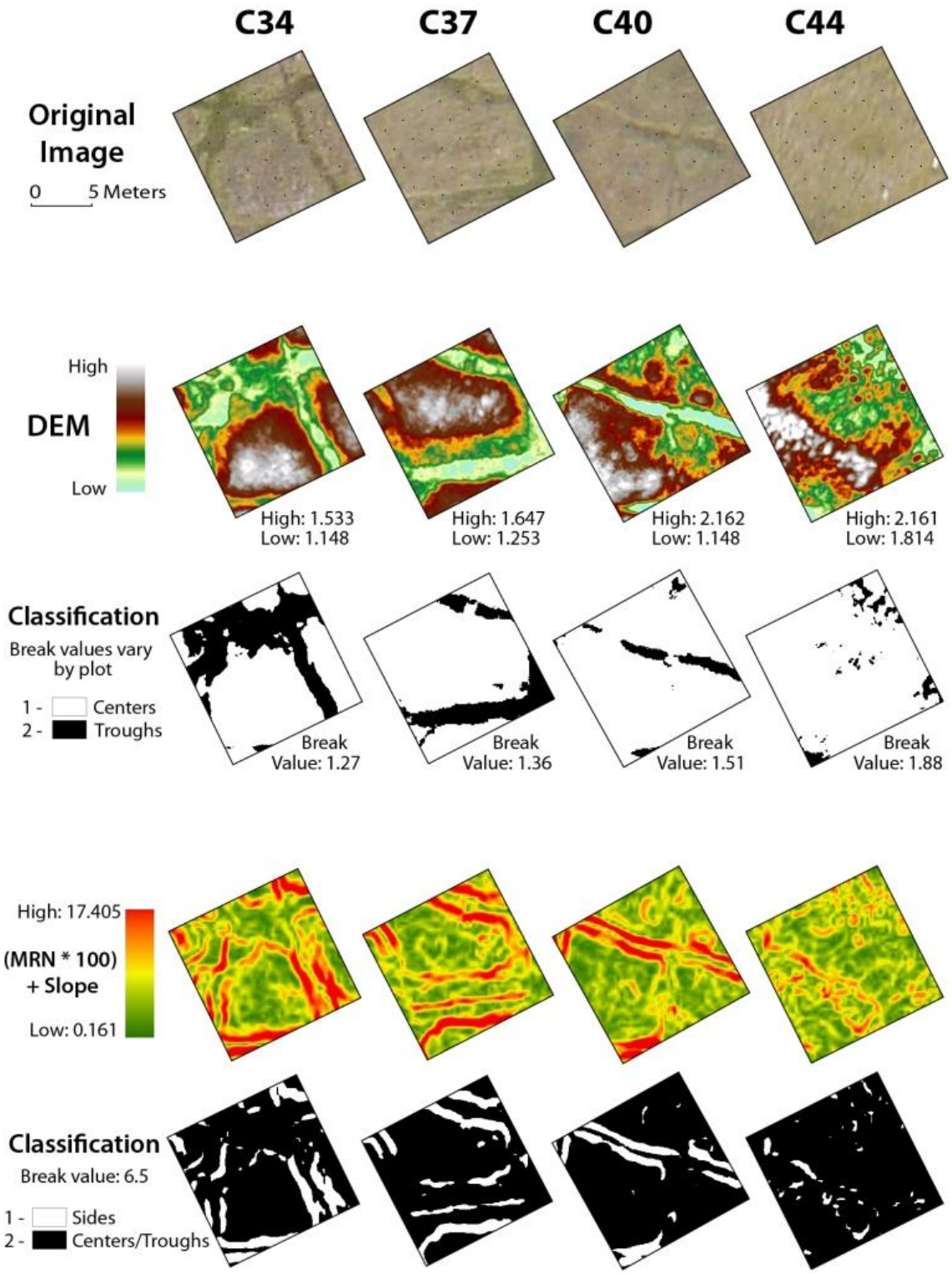

Figure 37. Construction of the binary maps used in the final microtopography classification of the DEMs for each plot. Break values were determined using both the DEM and aerial imagery as ground truth.

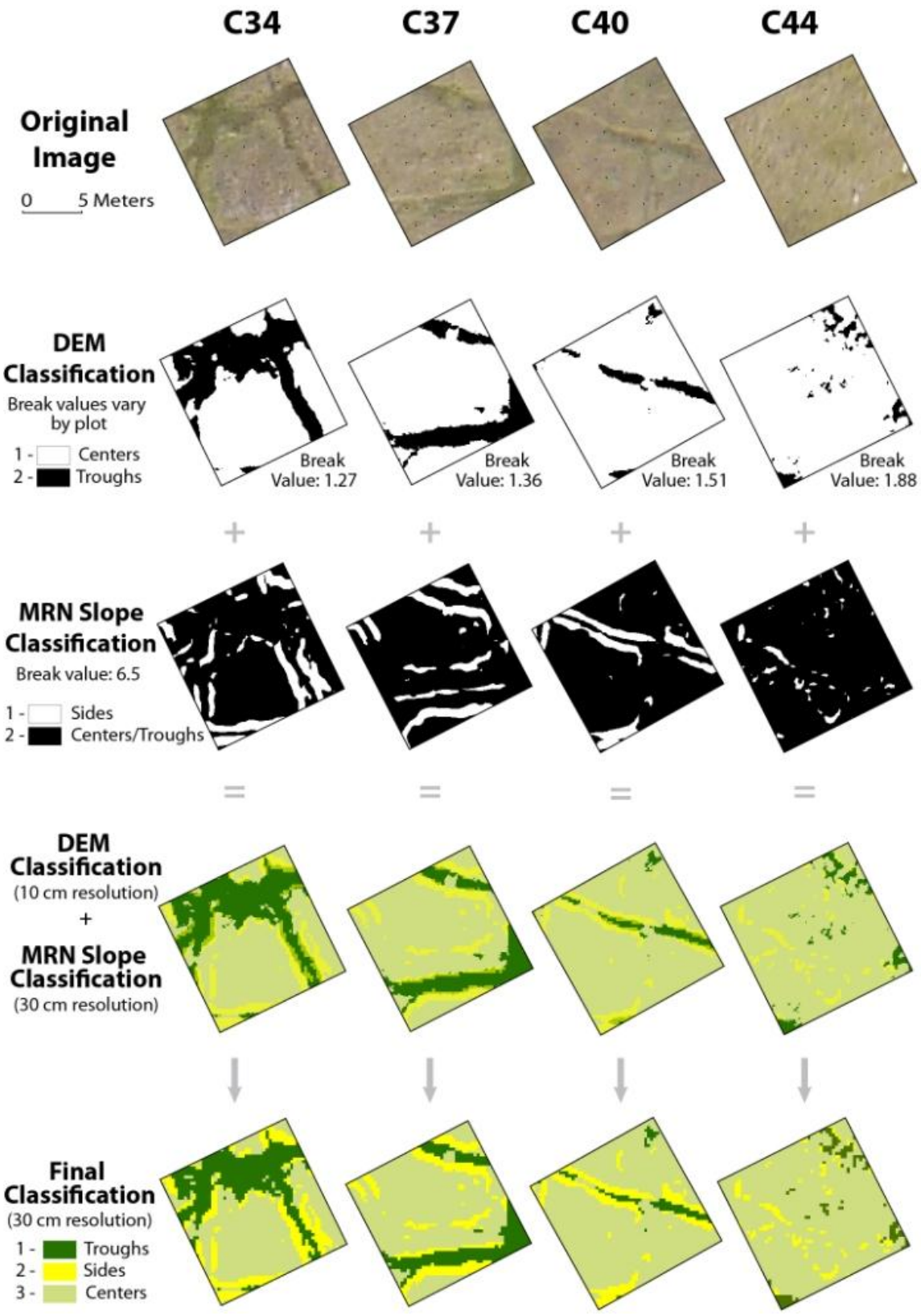

Figure 38. Final classification steps to produce the microtopography classification maps for each plot. Final maps were divided into three classes: troughs, sides, and centers.

5.5 Vegetation Classification

Calculations of the vegetation indices described in Table 4 of Section 4.4 for plot C34 are presented in Figure 39. The VVI was by far the best in terms of accurately quantifying variations in vegetation visible in the aerial photographs. The second-most reasonable index was the ExG, with the CIVE a close third. However, since the VVI produced such a reasonable result, no other indices were used to classify the CRREL plots.

VVI maps for all four plots are shown in Figure 40, along with the three experimental vegetation classifications for each plot created by slicing the VVI. Box-and-whisker plots of each classification in the context of the modern (1997-2012) ALT record are presented in Figure 41, and confirmed that no one classification was better than the others at explaining variations in ALT, so a classification was chosen based upon qualitative analysis (Section 4.4). The 4-class vegetation classification (Figure 40) was the one used in the final classification of the plots.

Maps of the final vegetation and microtopography classifications for each plot are presented in Figure 42. From the aerial photographs alone, it appeared that vegetation almost directly coincided with topography. While that assumption was true in certain places, the side-by-side comparison made clear that the microtopography did not always dictate vegetation cover at the study site. Each classification provided slightly different information about the microenvironments present in the plots – the vegetation classification provided more information about what was happening on the ground surface as seen in the aerial photographs, but the microtopography classifications extracted details about the landscape that were not visible in the photographs but clearly present in the DEM. Together, these classifications provided a more complete picture of

the microenvironments in the plots and a more comprehensive baseline for further analysis.

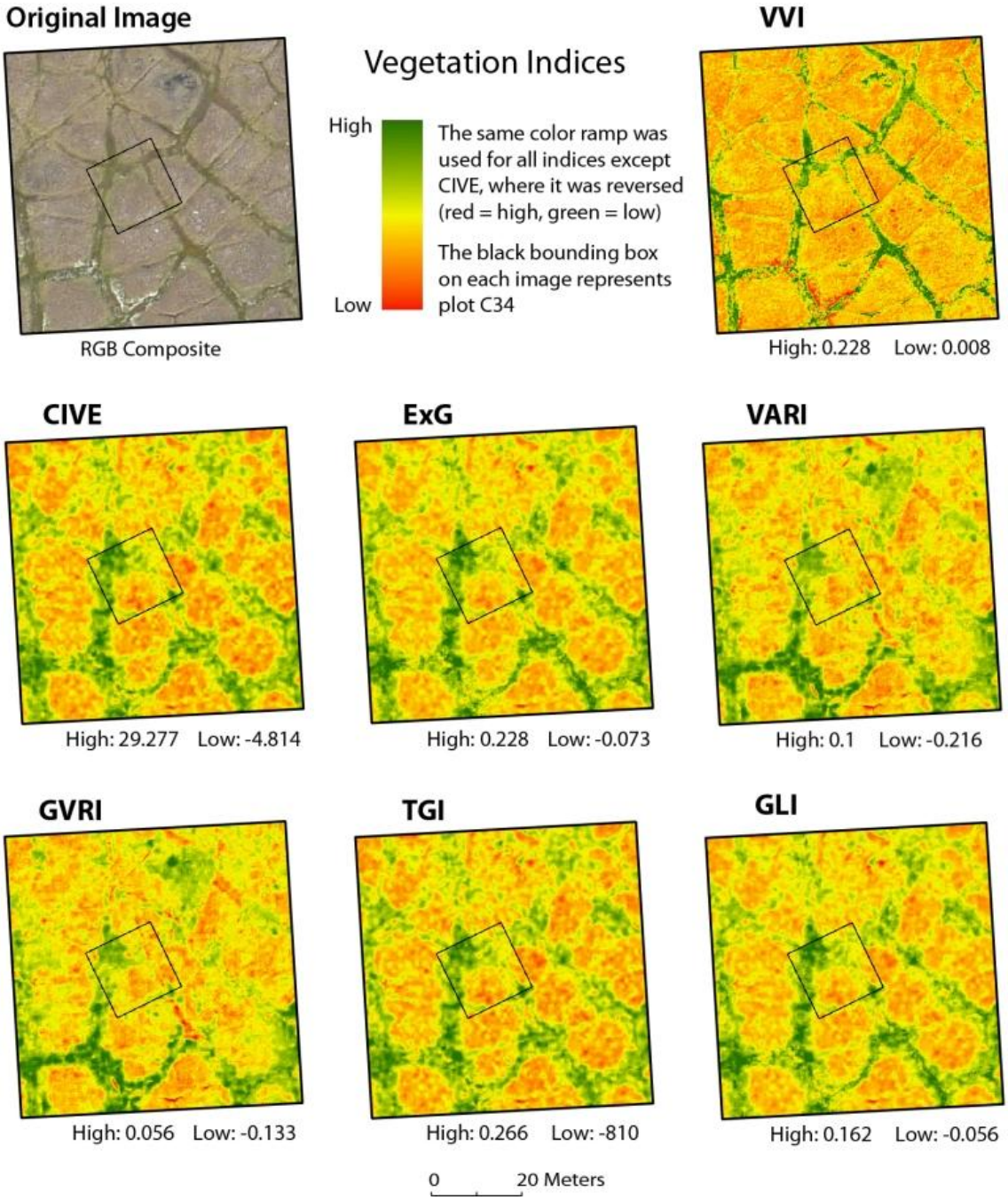

Figure 39. Vegetation index maps for plot C34. Aerial imagery of the site is provided for reference. The most informative index (the VVI) is shown in the upper-right.

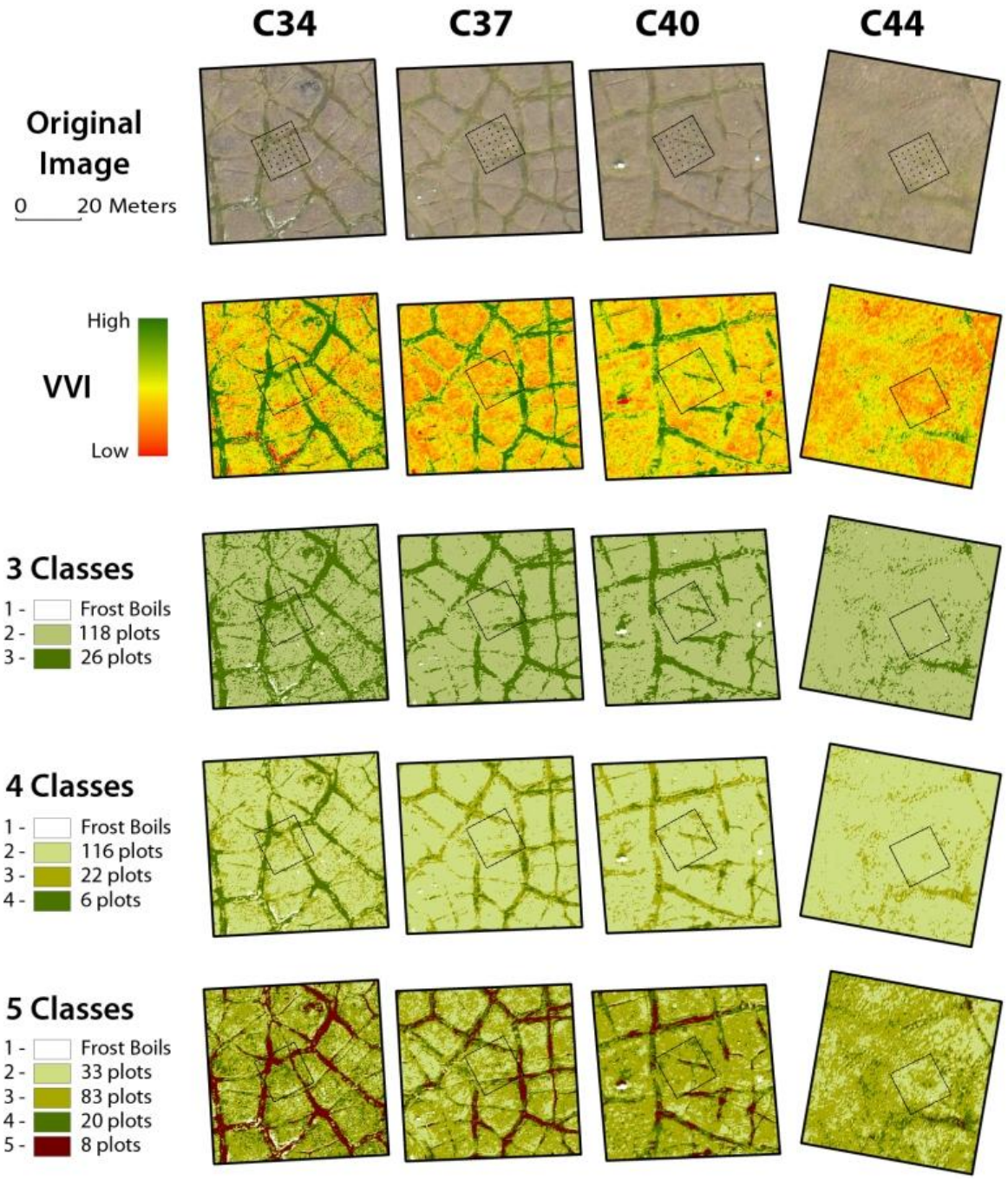

Figure 40. Maps of the three experimental vegetation classifications derived from the VVI for each study site. Legends indicate how many of the 144 ALT monitoring plots were represented by each class. Frost boils were classified on all maps, but none of the ALT monitoring plots fell within that category. Black boxes on each map represent the boundaries of each plot. The final classification used in analysis was the "4 Classes", which contained one class for frost boils and three for vegetation types.

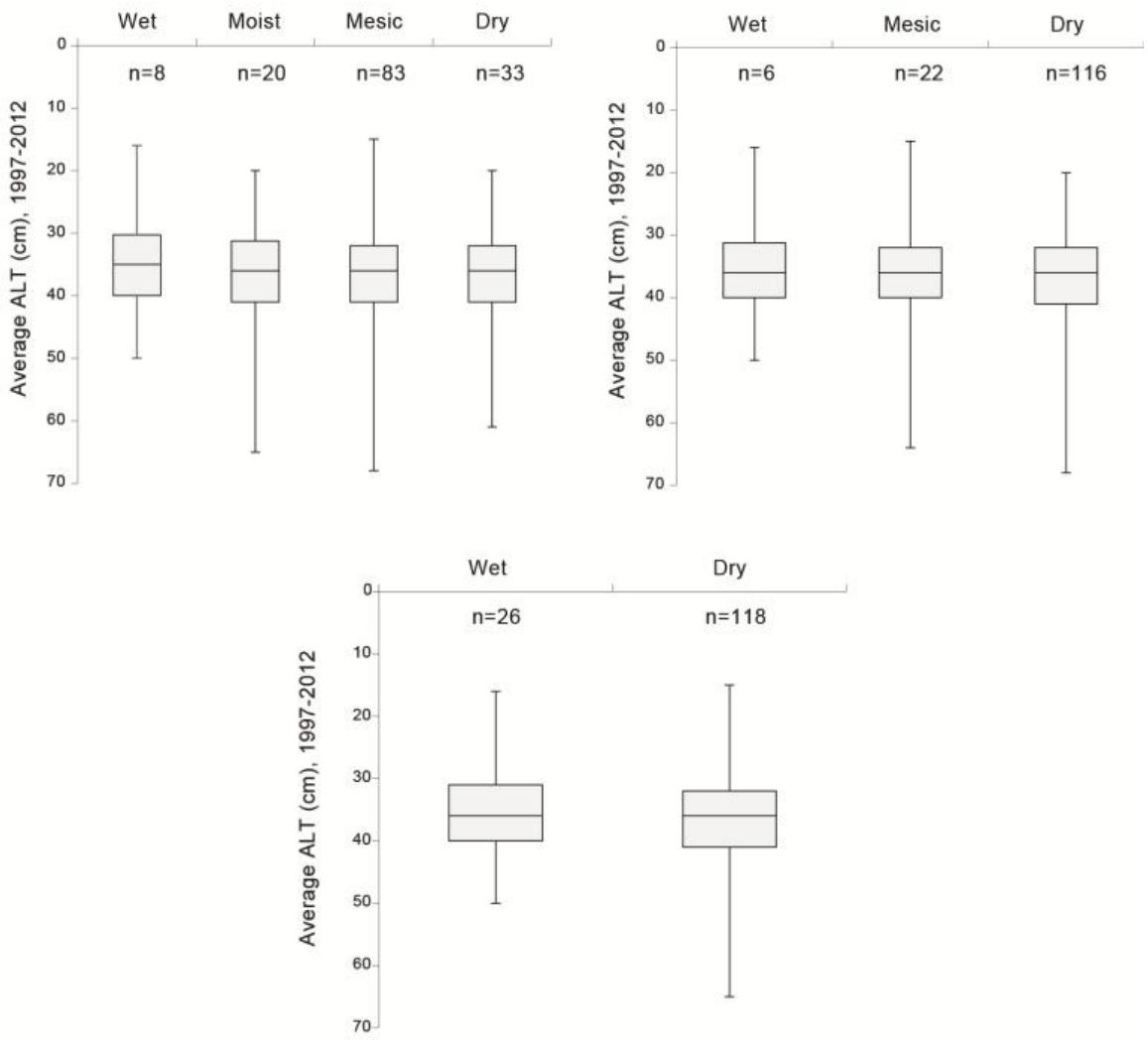

Figure 41. Box-and-whisker plots of active-layer thickness based upon each of the three experimental vegetation classifications. The final classification defined wet, mesic, and dry categories.

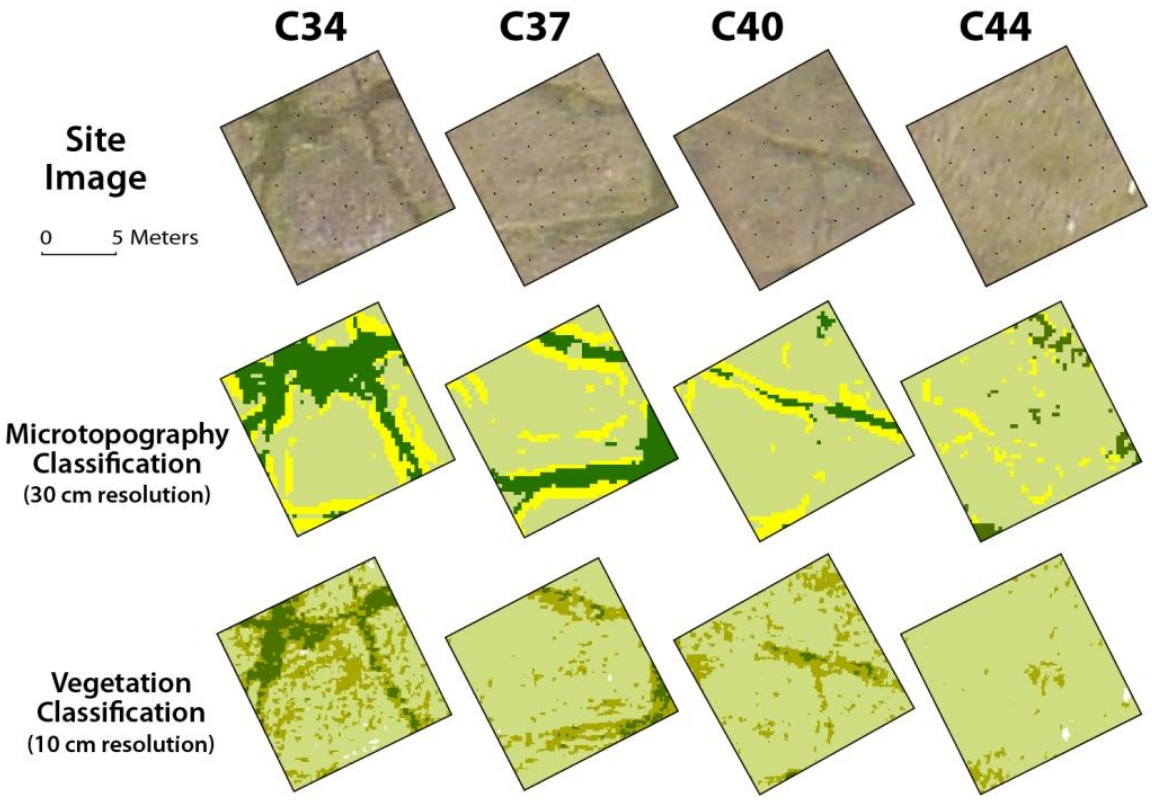

Figure 42. Maps of the final microtopographic and vegetation classifications as well as the aerial imagery for each study plot.

The operation used to extract the classification for the ALT and DGPS points is illustrated in Figure 43 and a summary of the results is presented in Table 13. The pixels shown in Figure 43 illustrate the occurrence of more than one classification type within each sample site. Classifications of these sites were determined based on the majority class as described in Section 4.3. The bulk of ALT and DGPS points were classified as mesic graminoid tundra and polygon centers. None of the sampling points were classified as bare ground (frost boils), so the subsequent vegetation examined the three remaining classes for ALT and only two for the DGPS sites, since none of those points fell into the wet graminoid tundra class.

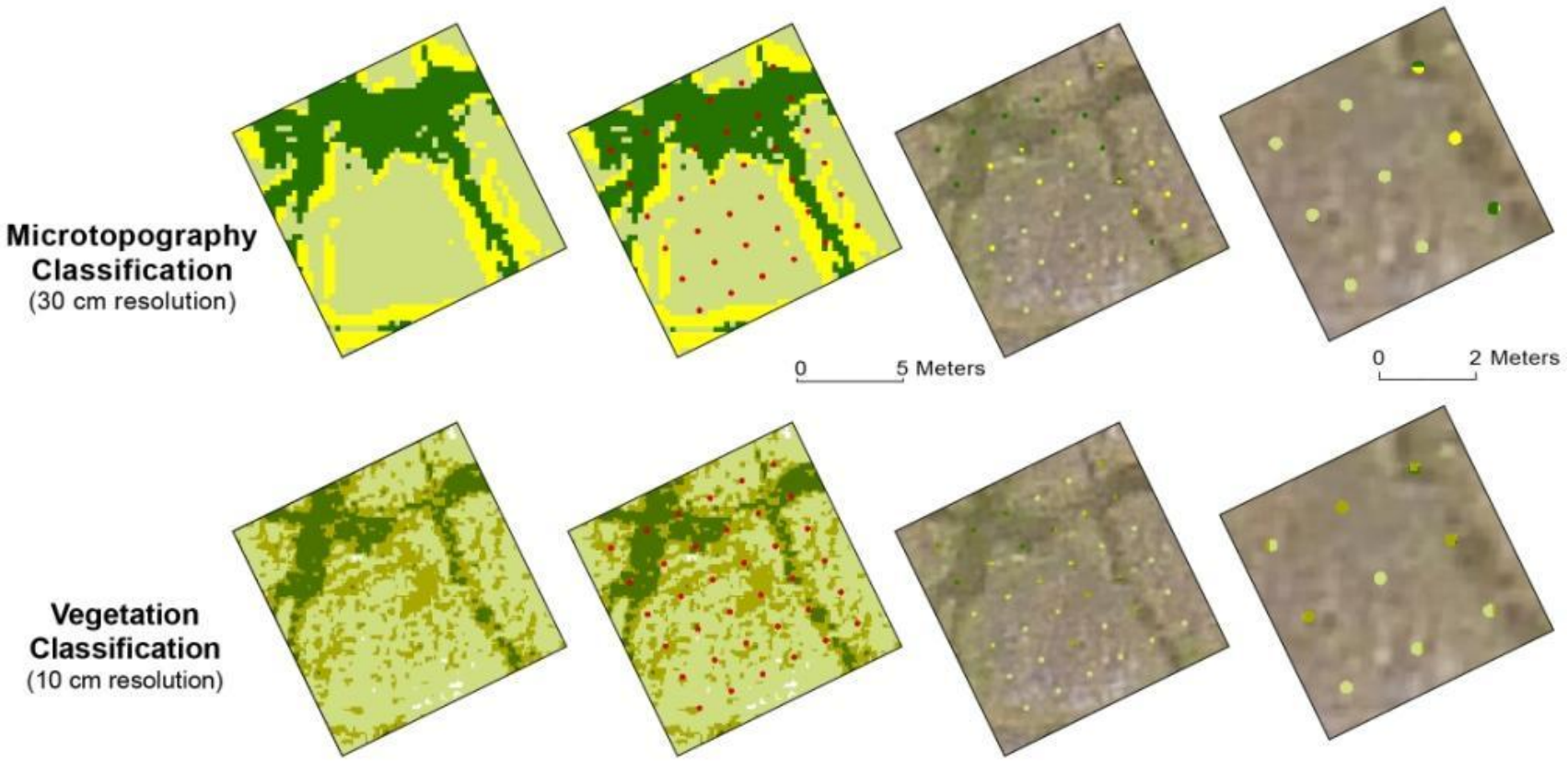

Figure 43. Illustration of the clipping operation used to classify the 144 ALT and 18 DGPS sites within the four study plots. Polygons used to clip ALT sites (shown in Figure 9) were ~30 cm (12 in) diameter circles to represent the sampling radius, and polygons used to clip the DGPS sites were ~5 cm diameter circles to account for the size of the target and rover antennae. Clipped areas that contained more than one class were classified based on whatever class occupied the majority of the area.

Table 13. Number of observations and percentages of the ALT and DGPS measurement points located within each microtopography and vegetation category.

		ALT	%	DGPS	%
Microtopography	Trough	20	14%	4	20%
	Side	21	15%	2	10%
	Centers	103	71%	14	70%
Vegetation	Wet	6	4%	0	0%
	Mesic	22	15%	3	15%
	Dry	116	81%	17	85%

5.6 Statistical Analysis

5.6.1 Active Layer Thickness

Summary statistics by plot of active layer thickness are presented in Table 14 to provide the context of the larger-scale spatial variability of thaw between the plots for 2010, as well as for the period corresponding to the 10-year DGPS record (2003-2012). For 2010, mean ALT values differed by ~3.4 cm among all plots, with the deepest mean ALT (43.8 cm) recorded at plot C37. Plot C44 had the greatest range of ALT values (30.0 cm), while plot C40 contained the most variability in measurements (standard deviation of 5.5 cm). Plot-level statistics from 2010 were similar to statistics from the 10-year record, with C37 and C40 consistently having greater ALT values than plots C34 and C44, with C40 having the most variability (standard deviation of 7.9 cm for 2003-2012). While there were differences between the plots, the range of values and magnitude of standard deviations suggest that these spatial variations were not statistically significant.

Table 14. Summary statistics by plot of ALT for 2010 and 2003-2012.

	C34		*C37*		*C40*		*C44*	
	2010	*2003-12*	*2010*	*2003-12*	*2010*	*2003-12*	*2010*	*2003-12*
No. of Points	36	360	36	360	36	360	36	360
Min	32.0	29.6	36.0	31.0	32.0	28.2	30.0	26.0
Max	53.0	42.4	55.0	50.5	54.0	59.8	60.0	48.8
Range	21.0	12.8	19.0	19.5	22.0	31.6	30.0	22.8
Mean	40.4	35.3	43.8	38.8	41.0	39.0	41.1	36.9
SD	4.4	2.4	4.8	4.1	5.5	7.9	7.0	4.9

Analysis of 2010 active-layer thickness based upon microtopography classes revealed only small differences in ALT between the polygon centers, sides, and troughs. Mean ALT varied slightly from 40.9 cm in the troughs to 42.2 cm on the slopes, but these differences were small compared to the standard deviations of 4-6 cm for each class. Descriptive statistics for 2010 ALT classified by microtopography are summarized in Table 15.

Table 15. Descriptive statistics for 2010 active layer thickness, based upon microtopography classes.

	Troughs	*Sides*	*Centers*
No. of Points	20	21	103
Min	34.0	32.0	30.0
Max	48.0	54.0	60.0
Range	14.0	22.0	30.0
Mean	40.9	42.2	41.6
SD	4.0	5.1	6.0

Analysis of variations in 2010 ALT between the three vegetation classes revealed even less variation than was observed between the microtopography classes. While ALT appeared to be slightly greater in the dry vegetation class, mean ALT only varied by

1.2 cm between vegetation types, with standard deviations of almost 6 cm. Points classified as wet graminoid tundra showed a substantially smaller range of ALT values, but this was based on only six sample points. Descriptive statistics for 2010 ALT classified by vegetation are summarized in Table 16.

Table 16. Descriptive statistics for 2010 active-layer thickness, based upon vegetation class.

	Dry	*Mesic*	*Wet*
No. of Points	116	22	6
Min	30.0	34.0	35.0
Max	60.0	54.0	48.0
Mean	41.7	41.0	40.5
Range	30.0	20.0	13.0
SD	6.0	4.3	3.8

Analysis of the modern (2003-2012) and historic (1962-1966) ALT measurements classified by microtopography revealed no substantial differences between the classes over time. Active layer thickness increased in all three classes by roughly the same amount (~2 cm) from the 1960's to the 2000's, and by ~6 cm in each class from the 1960's to 2010. No one class showed greater change in ALT over time than the others. A summary of the statistics for the time series comparison is presented in Table 17.

Table 17. Comparison of descriptive statistics for 2010, 2003-2012 and 1962-1966 ALT based upon microtopography classifications.

	2010			*2003-2012*			*1962-1966*		
Points	144			1,440			720		
	Trough	Side	Center	Trough	Side	Center	Trough	Side	Center
Min	34.0	32.0	30.0	16.0	20.0	17.0	16.0	21.0	21.0
Max	48.0	54.0	60.0	56.0	57.0	67.0	52.0	52.0	58.0
Range	14.0	22.0	30.0	40.0	37.0	50.0	36.0	31.0	37.0
Mean	40.9	42.2	41.6	36.4	35.7	38.1	34.2	34.0	36.1
SD	4.0	5.1	6.0	7.3	7.0	7.4	7.5	5.9	6.9

A box-and-whisker plot of the 144 individual measurements from all four CRREL plots on an annual basis (Figure 44), illustrating the gradual deepening of the active layer over time. One small trend suggested by the box plot that is not perceptible in the table of averages is a slightly greater increase of ALT in the troughs over time (~0.06 cm/year) when compared to the polygon centers and sides (~0.05 cm/year). However, the high variability of the data within each class and among years made it difficult to draw definitive conclusions. A summary of the rate of increase in ALT for each class is presented in Table 18

.

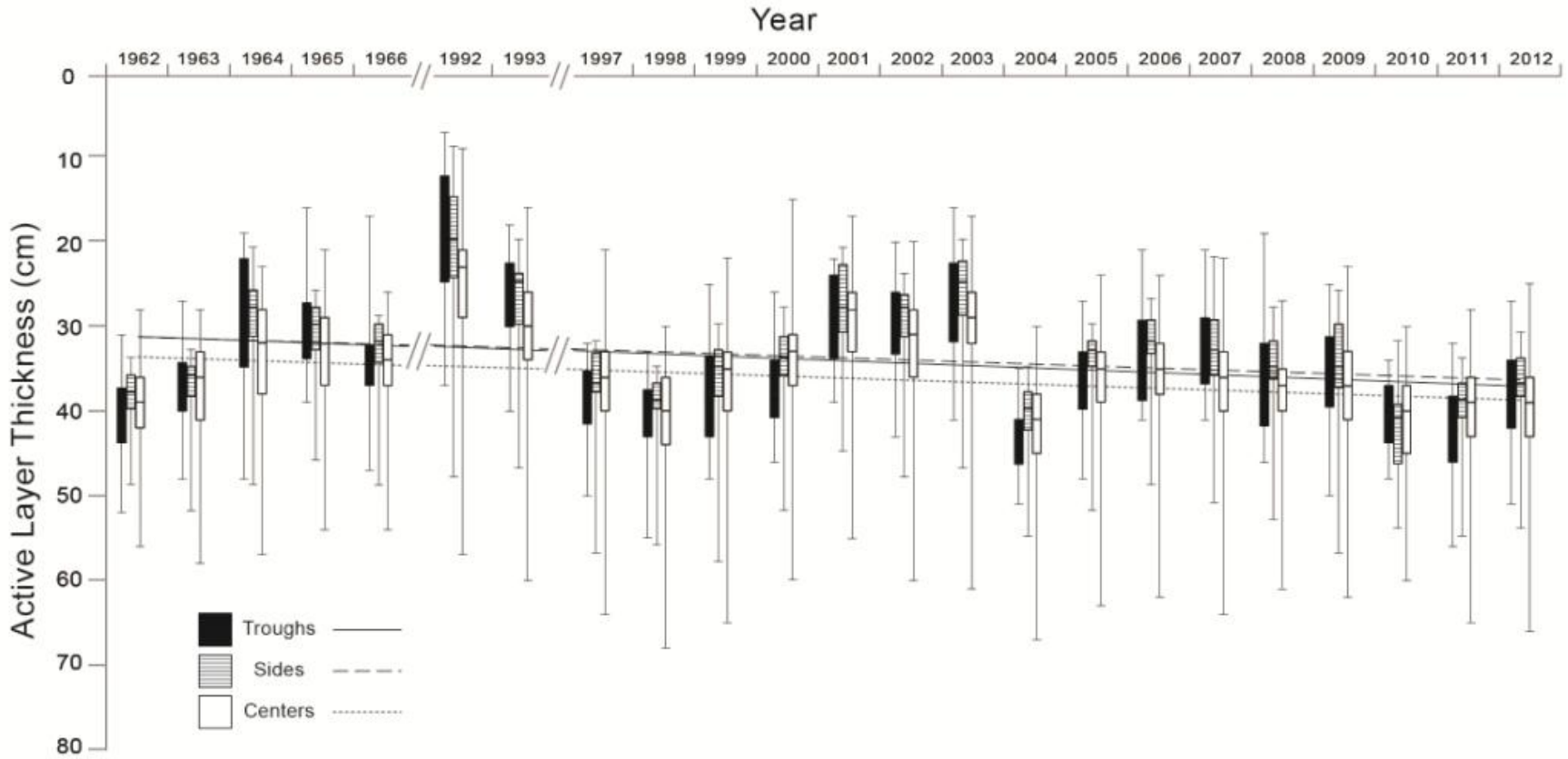

Figure 44. Box-and-whisker plot for ALT based upon microtopography class. Lines represent the general trend from 1962-2012, with the two breaks in the x-axis and trend lines signifying the lack of available data for the years 1967-1991 and 1994-1996.

Table 18. Rate of increase in ALT for each microtopography class.

	Troughs	*Sides*	*Centers*
Rate of increase in ALT (cm/year)	0.06	0.05	0.05

Analysis of the modern (2003-2012) and historic (1962-1966) ALT measurements classified by vegetation class revealed few differences. Active-layer thickness increased in all three classes (~2-3 cm) from the 1960's to the 2000's, and by ~6-7 cm in each class from the 1960's to 2010, but no class showed greater change in ALT over time than the others. A summary of the statistics for the time series comparison is presented in Table 19.

Table 19. Comparison of descriptive statistics for 2010, 2003-2012 and 1962-1966 ALT based upon vegetation classifications.

	2010			*2003-2012*			*1962-1966*		
Points	144			1,440			720		
	Wet	Mesic	Dry	Wet	Mesic	Dry	Wet	Mesic	Dry
Min	35.0	34.0	30.0	16.0	19.0	17.0	19.0	16.0	21.0
Max	48.0	54.0	60.0	50.0	64.0	67.0	43.0	56.0	58.0
Range	13.0	20.0	30.0	34.0	45.0	50.0	24.0	40.0	37.0
Mean	40.5	41.1	41.7	35.6	37.2	37.6	33.3	34.3	35.9
SD	3.82	4.30	5.96	6.93	8.86	7.07	6.75	7.98	6.64

A box-and-whisker plot of the 144 individual measurements combined from the four plots on an annual basis is provided in Figure 45. While the overall trend of increasing ALT was observable in all vegetation classes, one potential class-specific trend suggested by the scatterplot is a slightly smaller increase in ALT in the dry vegetation class (~0.04 cm/year) when compared to the mesic and wet classes (~0.07 and

~0.06 cm/year respectively). However, the magnitude of this difference is so small relative to the interannual and interclass variability of the data that definitive relationships are tenuous. A summary of the rate of increase in ALT for each class is presented in Table 20.

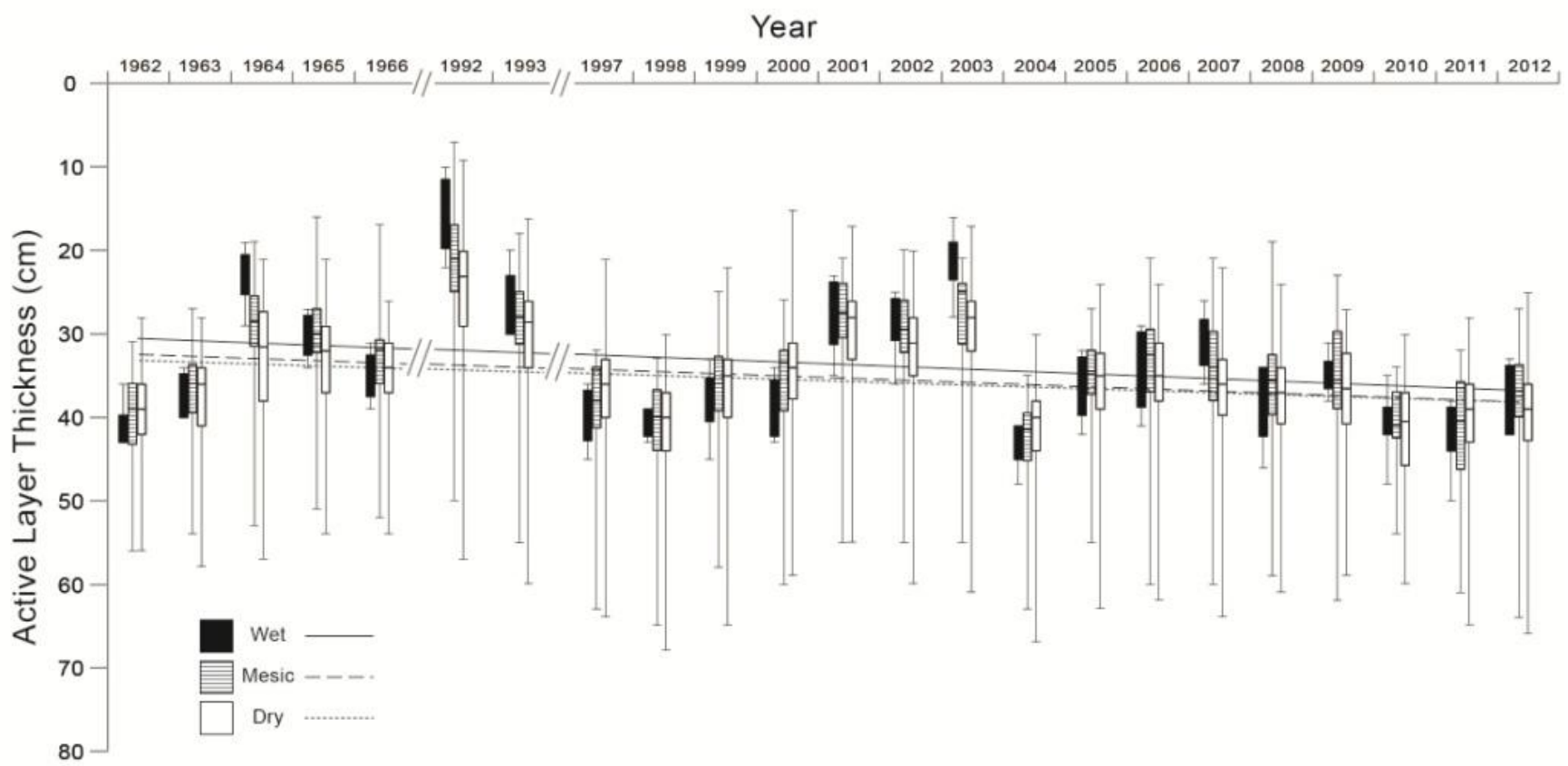

Figure 45. Box-and-whisker plot for ALT based upon vegetation class. Lines represent the general trend from 1962-2012 with the two breaks in the x-axis and trend lines signifying the lack of available data for the years 1967-1991 and 1994-1996.

Table 20. Rate of increase in ALT for each vegetation class.

	Wet	*Mesic*	*Dry*
Rate of increase in ALT (cm/year)	0.04	0.07	0.06

5.6.2 DGPS

The 10-year DGPS record is summarized by plot in Figure 46, which illustrates the interannual variability in elevation within and between the plots. All plots showed some degree of subsidence over the ten-year period, most perceptibly in plot C44 (~ -3.1 cm/year) and the least in plot C40 (~ -0.5 cm/year). A summary of the linear regressions for each plot is presented in Table 21.

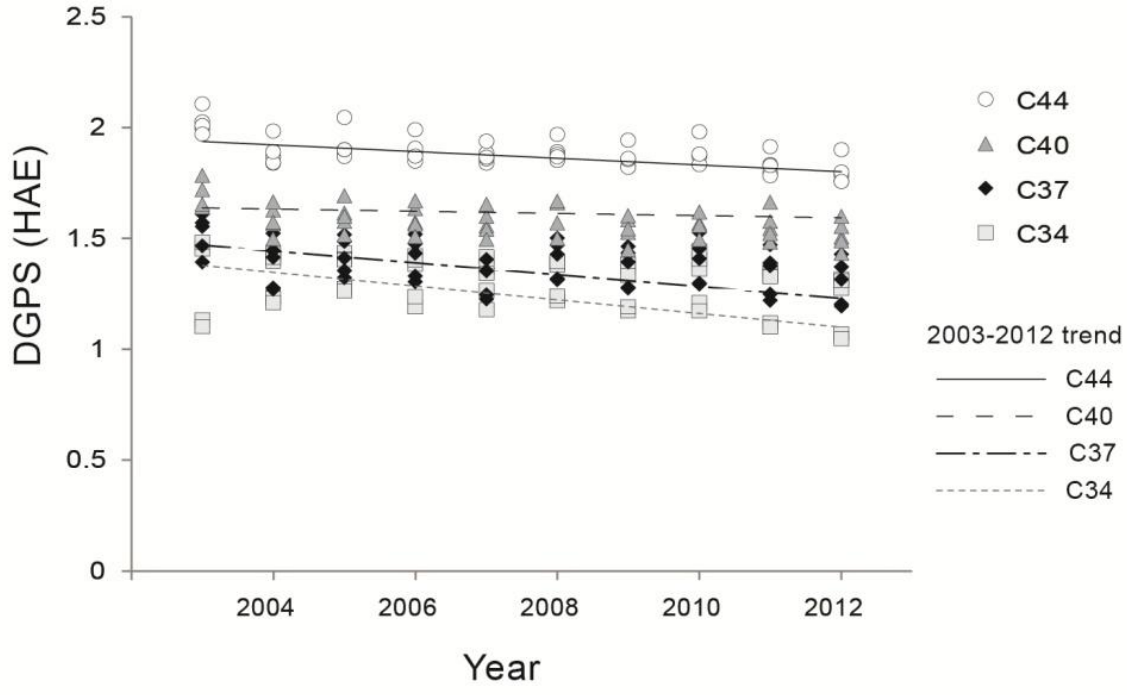

Figure 46. Scatterplot of DGPS measured heights from 2003-2012 grouped by plot. Lines indicate the general 10-year trend of subsidence at each plot.

Table 21. Summary of linear regressions for DGPS points by plot.

	C34	*C37*	*C40*	*C44*
Rate of subsidence (cm/year)	-3.1	-2.7	-0.5	-1.5
R^2	0.49	0.42	0.08	0.72

No substantial differences were found between the DGPS points when analyzed in the context of microtopography (Figure 47). As expected, mean elevations of polygon centers were greater than those of the troughs, while the polygon sides were lower than both of the other two classes, but polygon sides were represented by only 2 points, both of which are in plot C34. The general trend in subsidence was slightly greater in the troughs (-2.2 cm/year) than the centers (-1.5 cm/year), but given the variability within each class the difference was not tested for statistical significance. Plot C44 was, on average, 49 cm higher in elevation than the other three plots, and the presence of a trough sampling point in that plot raised the mean elevation for that class in all years by 12.6 cm, potentially skewing the overall trend in subsidence based on class means. However, exclusion of this point only changed the mean rate of subsidence in the troughs by approximately 0.2 cm (to -2.4 cm/year).

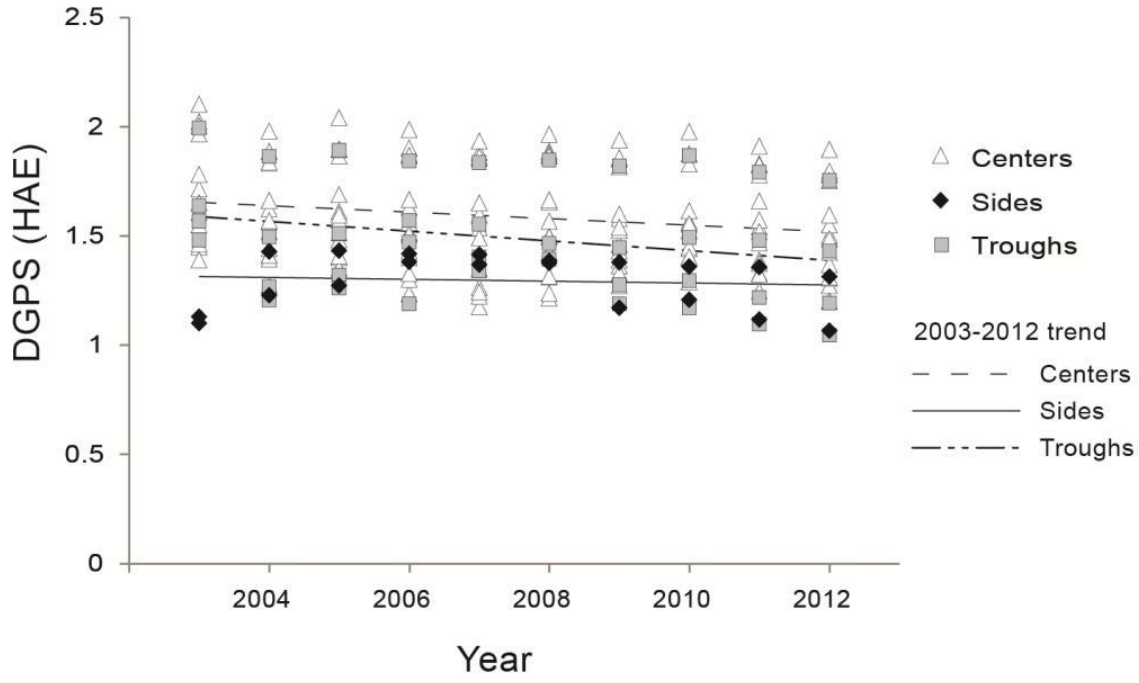

Figure 47. Scatterplot of DGPS measured heights from 2003-2012 grouped by microtopography class. Lines indicate the general 10-year trend of subsidence for each class.

In the context of the entire 10-year record, subsidence of the two sampling points on the polygon sides was much less (-0.4 cm/year) than for the centers and troughs. Closer examination of these points in Figure 47 showed the elevations for those two points in 2003 anomalously low compared to all other years, and when the 2003 data was omitted from analysis, the subsidence trend for the polygon sides aligned with that of the centers and troughs at a mean rate of -2.1 cm/year. Exclusion of the 2003 data also significantly improved the R^2 value, from 0.02 to 0.60. Table 22 contains a summary of all linear regression results for the microtopography classes.

Table 22. Summary of linear regressions for DGPS points by microtopography class.

	Troughs	*Sides*	*Centers*	*Troughs* *C441 excluded*	*Sides* *2003 excluded*
Rate of subsidence (cm/year)	-2.2	-0.4	-1.5	-2.4	-2.1
R^2	0.56	0.02	0.62	0.56	0.60

The vegetation classification of the DGPS points resulted in the representation of only two classes in the final analysis (dry graminoid tundra and mesic graminoid tundra), with only three points falling in the mesic class: two in plot C34 and one in C40. Mean rates of subsidence between the two vegetation classes differed by 0.7 cm, with mean subsidence rates of points in the drier vegetation of -1.4 cm/year, and those in the mesic averaging -2.1 cm/year, with no obviously outliers (R^2 of 0.712 and 0.542, respectively). These rates of subsidence roughly correspond to those observed on the polygon centers and troughs (Table 22), suggesting that locally higher, drier areas (usually polygon centers) are subsiding at a slightly lesser rate than the lower, wetter areas (usually in the troughs). Figure 48 illustrates the trends in subsidence based on vegetation classification. The results of the linear regressions for each class are presented in Table 23.

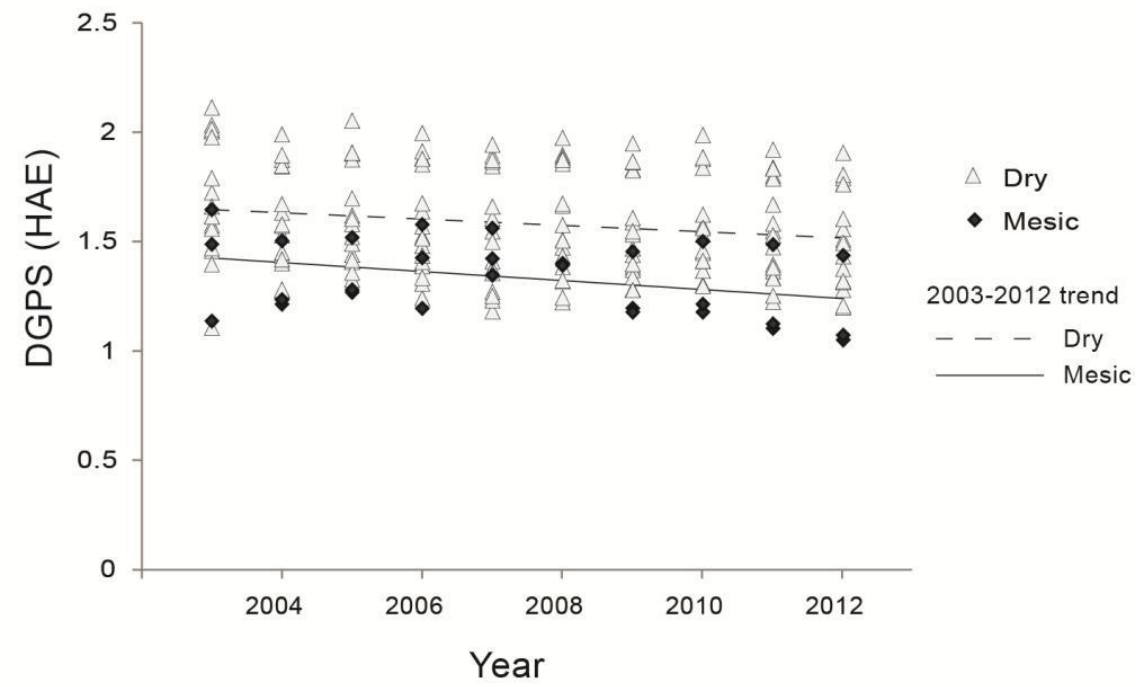

Figure 48. Scatterplot of DGPS measured heights from 2003-2012 grouped by vegetation class. Lines indicate the general 10-year trend of subsidence for each class.

Table 23. Summary of linear regressions for DGPS points by vegetation class.

	Mesic	*Dry*
Rate of subsidence (cm/year)	-2.1	-1.4
R^2	0.54	0.71

6 CONCLUSIONS AND RECOMMENDATIONS

Detailed analysis of the terrestrial LIDAR data collected on the CRREL transect near Barrow in 2010 produced four high-resolution DEMs, along with analysis of the errors inherent in the data, which can be used to advise and inform future high-resolution data collection and interpretation at these sites and in similar settings. Interpretation of ALT and DGPS records in the context of microtopography and vegetation classifications derived from such high resolution data revealed substantial variability in both datasets and little differentiation within classes at this fine resolution.

6.1 Terrestrial LIDAR Data

When terrestrial LIDAR is used to produce multiple scans of a very small area, the result is datasets that are so dense that, in the absence of large spatial voids due to occlusions, small relative differences in data density do not greatly influence the quality of the data or its derivatives. Analysis of the original LIDAR point cloud demonstrated that the spatial distribution of errors in the derived DEMs was unaffected by the density of the original data within the study plots, probably because the point densities were larger than a threshold above which additional data points no longer contribute to the vertical accuracy of the point cloud as a whole. Considering that only ~0.3% of the original point cloud was used to generate the DEMs, this finding is not all that surprising. On two of the four plots (C37 and C40), even those areas with minimum point density (16 and 24 points/100 cm^2, respectively) still contained ~20× more data than was utilized for accurate DEM interpolation. However, this additional data may contain information

about the vegetation layer that could be useful for studies focused more on details in vegetation cover rather than details in ground surface.

While the additional points were not analyzed further in this study, future research focused on environments with greater vertical dimensionality in the context of either landscape or vegetation, such as erosion monitoring (Rosser et al. 2005) or forest inventory (Hopkinson et al. 2004), may benefit more from the high density (over 100 points/10 cm^2) of terrestrial LIDAR collections. Studies in environments with limited vertical dimensionality that are looking only to derive a high resolution surface model may be better served by aerial LIDAR collections, although logistical constraints often dictate the type, quality, and quantity of data the can be collected.

Intensity images for the plots were not useful in this study because the values had not been calibrated. For future LIDAR collections, it would be worth investigating to see if the calibration of intensity values aided in interpretation of the point cloud. While intensity images tend to be most successful at discriminating ground cover in built environments where surfaces are highly variable, carefully calibrated intensity values can detect changes in the vegetation distribution within some landscapes (Song et al. 2002). This kind of information collected at high resolutions and in combination with the fine-scale elevation data derived from the same LIDAR point cloud could generate a powerful tool for micro-scale analysis that would be impossible to develop with the current labor-intensive ground-based methods.

The cause of the streaking that was present in the LIDAR point cloud and in all of the DEMs at resolutions <10 cm remains unknown. The good performance of the interpolated DEM when compared to the withheld LIDAR control points (RMSE

<0.3 cm against 50 cm resolution lowest-point-withheld control data) suggests that the streaking is not an artifact of the interpolation but is intrinsic within the point cloud itself. Removal of these anomalies would be critical for accurate representation of ground surface at resolutions finer than 10 cm. The data used in this study was delivered as single-return data, even though the full waveform was recorded at the time of collection. It is possible that the information contained in multiple and last returns could be used to systematically filter out these irregularities. When interpolated onto a DEM, the streaks formed ridges that ranged from ~2-5 cm in height, which is approximately the magnitude of the differences between the DGPS measurements and the raw LIDAR point cloud. If last returns were used to filter the single returns, the accuracy of the LIDAR compared to the ground truth DGPS data might increase substantially. This would also affect the resolution at which a DEM could be interpolated. Creation of a 10 cm resolution DEM from data that was delivered at an original resolution on the scale of millimeters represents an incomplete and inefficient use of the available technology. For all future LIDAR collections, if the full waveform is recorded at the time of collection, it should be included in the exported data products and analyzed in its entirety.

Preliminary investigations into the potential role of atmospheric conditions and vegetation cover (Section 5.2) found no confirmed explanation for the streaking pattern. Variations in scanner speed could have introduced small but repetitive errors into the point cloud (John Gale, pers. comm., 14 December 2012), but this information was not documented during acquisition and the theory cannot be tested without repetitive scanning. A literature review unearthed no other hypotheses or documented cases of these patterns in terrestrial LIDAR data, however, it is important to note that terrestrial

LIDAR is are still fairly new technology to many researchers. Exploratory research and analysis is ongoing and it seems unlikely that the phenomena observed in this data are unique to this particular LIDAR collection. It is possible that these issues are being addressed and results just have yet to be published; however, at the time of writing no practical solutions could be found.

Apart from the streaking artifacts, one other anomaly uncovered in analysis of the LIDAR point cloud and the DEM compared to the ground truth DGPS data was the two outlier DGPS points (344 and 345). The differences at these points between the interpolated DEM elevation and the DGPS elevation were over 20 cm, while the mean differences at all other points were ~3 cm. Discrepancies at these two points occurred in all of the DEMs tested in this study, confirming that they were not an artifact of any one interpolation model. What is most puzzling is that the difference between the raw LIDAR point cloud and the DGPS measurements at those points was only 2.7 cm. The data used to interpolate the DEMs had been thinned to a resolution of one point (the lowest) every 10 cm, so even if there were anomalously high data points present in the original point cloud at these locations, they should have been filtered out in the presence of lower points. Therefore, it is unclear what characteristics of the point cloud data structure caused all of the DEM generation methods to interpolate these points with such consistently high errors, especially since the overall performance of the DEM compared to the LIDAR control points was quite good.

These findings suggest that there may be instances where it is more appropriate to conduct analysis with elevations extracted directly from individual points in a LIDAR point cloud rather than from an interpolated digital elevation model. DEMs are essential

tools in calculations where a continuous surface is necessary, such as in hydrological modeling, floodplain mapping, or other surface-based predictions. They also provide high-quality, informative visual references for the display of other layers of information. However, in situations where the objective is to monitor changes at discrete points on the ground, rather than model the surface as a whole, direct analysis of the LIDAR point cloud may provide a more accurate means of assessing slight variations in topography at ultra-fine resolutions.

One attribute of the LIDAR point cloud that was not investigated in this study were the RGB values, which were delivered in the original data files for each LIDAR point and made it possible to render the raw point cloud as if it were a photograph of the scanned area (Figure 15). The vegetation classification component of this study demonstrated the effectiveness of visible-band indices, specifically the VVI, in describing the vegetation distribution at the four study plots. The VVI classifications were limited in descriptive capability by the ~10 cm resolution of the original photograph upon which they were based. Since only RGB values are needed for those index calculations, it should be feasible to derive a much higher-resolution classification directly from the LIDAR point cloud. If repeat scans were carried out, this analysis could make it possible to track subtle changes in the vegetation community over time at sub-centimeter resolutions.

6.2 ALT and DGPS Analysis

The classification of active layer and DGPS monitoring sites based upon microtopography and vegetation proved largely uninformative. Previous studies of the active layer near Barrow (Brown & Johnson 1965; Brown et al. 2000; Hinkel & Nelson

2003), have suggested that microtopography plays an important role in the determination of ALT and other physical properties on the landscape; however, the results of this study did not find clear correlations with either ALT or subsidence within these four study plots. While subtle differences could be perceived at very fine (mm) scales of analyses, such as a slightly greater increase in ALT in the troughs or a slightly lesser increase in ALT in the dry graminoid tundra, the small magnitude of these trends coupled with the high interannual and interclass variability, made it impossible to draw any significant conclusions about spatial or temporal trends. The standard deviations of ALT when classified by microtopography or vegetation class were just as large as when points were grouped by plot, possibly due to the diameter of the area within which each ALT point observations were taken compared to the 10 × 10 cm pixels of the DEM and aerial photographs used to create the microtopographic and vegetation classifications.

The active layer near Barrow has previously been described as exhibiting Markovian-like behavior on a roughly decadal scale (Brown et al. 2000, Hinkel & Nelson 2003, Nelson et al. 1998), meaning that the active layer will remain fairly constant for a number of years and then "reset" to a significantly greater or lesser depth in response to climatic thawing of the transient layer, which will then gradually thicken over subsequent years until another "reset". This kind of behavior explains the lack of any linear trends in the data when examined on a time scale greater than a few years, particularly when the data from the early 1990's (which exhibited particularly shallow ALT) was included in the analysis. All microtopography and vegetation classes appeared affected equally in these general trends of ALT and subsidence.

While Markovian behavior may explain the temporal differences in ALT, it does not account for the lack of patterns within the spatial variability in any given year. Environmental variables such as high soil moisture and snow accumulation tend to dampen thermal fluctuation and have been shown to coincide with areas of maximum thaw (Hinkel & Hurd 2006; Nelson et al. 1998), and should theoretically coincide, at least in part, with the microtopography and vegetation classes outlined in this study. This may be due to the size of the area within which ALT observations were taken compared to the size of the area depicted by the microtopographic and vegetation classifications used here and underlines the importance of metadata on exactly how precisely observations were taken as part of a monitoring program when later studies may take place at a scale unavailable at the onset of a long-term initiative.

However, since no significant differences were found between these classes, it may be that the fine scale enabled by the terrestrial LIDAR is simply too fine to be the appropriate scale of observation for monitoring the active layer and ground subsidence. Nelson et al. (1998) concluded that "the close covariance between plots with dissimilar ground cover, microtopography and soil characteristics indicates that continuation of intensive sample at all of the CRREL plots may not increase the yield of information on geographic variation substantially" and suggests that the scale of maximum variability may be coarser than what is covered by the transect. Hinkel & Nelson (2003) found that most variation occurs at sample separation distances of 100-300 m at CALM monitoring sites on the coastal plain. Focusing on data at cm-resolution when the most important changes are happening on the scale of tens or hundreds of meters could put researchers at risk of losing sight of the bigger picture of changes in the permafrost landscape.

This discussion then begs the question – how fine of a scale is too fine for monitoring and mapping purposes? This study suggests that terrestrial LIDAR scans provide exponentially more information than can be feasibly processed or sufficiently interpreted for mapping purposes. Rather than enhancing analysis, this surfeit of data only complicates it. Technology is constantly evolving and may very well be able to cope with this kind of high density data in the not-too-distant future. But the ability to detect changes on the scale of millimeters may not yield substantial improvements in understanding of the most important processes for the general landscape. It becomes more and more important for researchers to carefully consider and investigate the most appropriate scale at which to collect and analyze data, particularly as finer and finer scale data becomes available with increasing technology.

7 FURTHER RESEARCH OPPORTUNITIES

7.1 Historical Elevation Data

In comprehensive monitoring of permafrost landscapes, decadal trends are often much more meaningful than interannual variations (Hinkel & Nelson 2003). Since data exists for the CRREL plots dating back to the 1960's, they provide a valuable opportunity to monitor change on a temporal scale not possible at other sites. While comparison of absolute elevations from the 1960's was not possible at this time, the elevation data collected on the CRREL plots from that time period still hold valuable information that can be used to detect relative changes in the microtopography at the plot level. These changes can be quantified and mapped and may provide insight into which features on the landscape (troughs, centers, frost boils, etc.) are expanding or shrinking or heaving or subsiding over time. Such investigations may also reveal differences in rate of change between the plots. Exploratory research into this kind of analysis produced a series of basic maps for plot C34 (Figure 49) that could be enhanced by more quantitative analysis and done for other plots. If a reliable method could be established for converting the 1960's elevation to the present-day geoid model, the dataset would become even more valuable in the context of modern observations. One suggestion if comparing the historic elevations to modern LIDAR data would be to use the information contained in the raw point cloud rather than the interpolated DEM. Since the elevation measurements involve a relative small number of discrete points (total of 144 points within the four plots), the point cloud could be clipped to those areas and elevation derived directly from the lowest point for a more true representation of ground surface. This would improve accuracy and consistency by avoiding the errors introduced by interpolation.

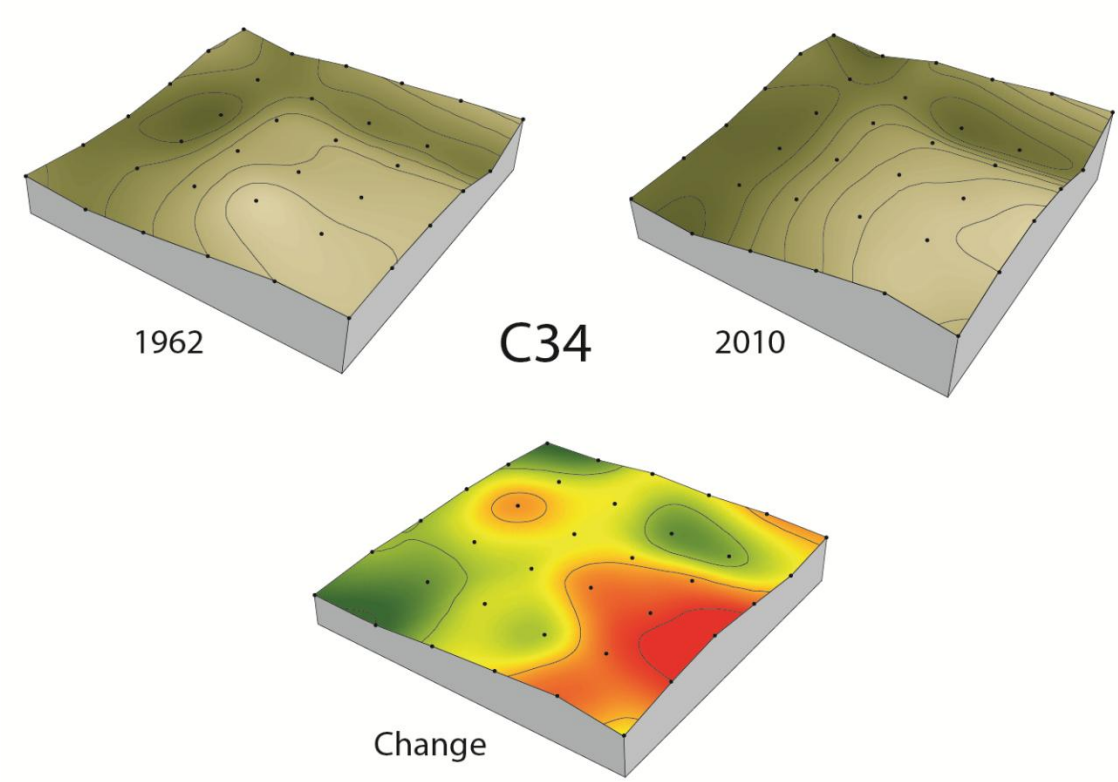

Figure 49. Experimental elevation diagrams for plot C34, comparing elevations recorded in the 1960s (upper-left) to those in 2010 (upper-right). Elevations for 2010 were calculated from the DEM heights using the GEOID99 conversion model. Due to an undocumented datum in the early data, absolute values for change could not be determined, but the bottom diagram reflects the relative amount of change between two dates (areas in red represent the most change).

7.2 Other LIDAR-based Initiatives

In the summer of 2011, terrestrial LIDAR data was collected for a 20 × 50 m grid in the southwestern portion of the BEO, ~2 km south of the CRREL study sites. Once fully analyzed, this dataset could provide an informative comparison for data analyzed in this study – both the original LIDAR point clouds as well as the derived DEMs. An quick visual analysis of the raw point cloud from 2011 rendered by RGB values (Figure 50) reveals some of the same accuracy and error issues (data voids, flagging, etc.) observed in the LIDAR data collected in 2010.

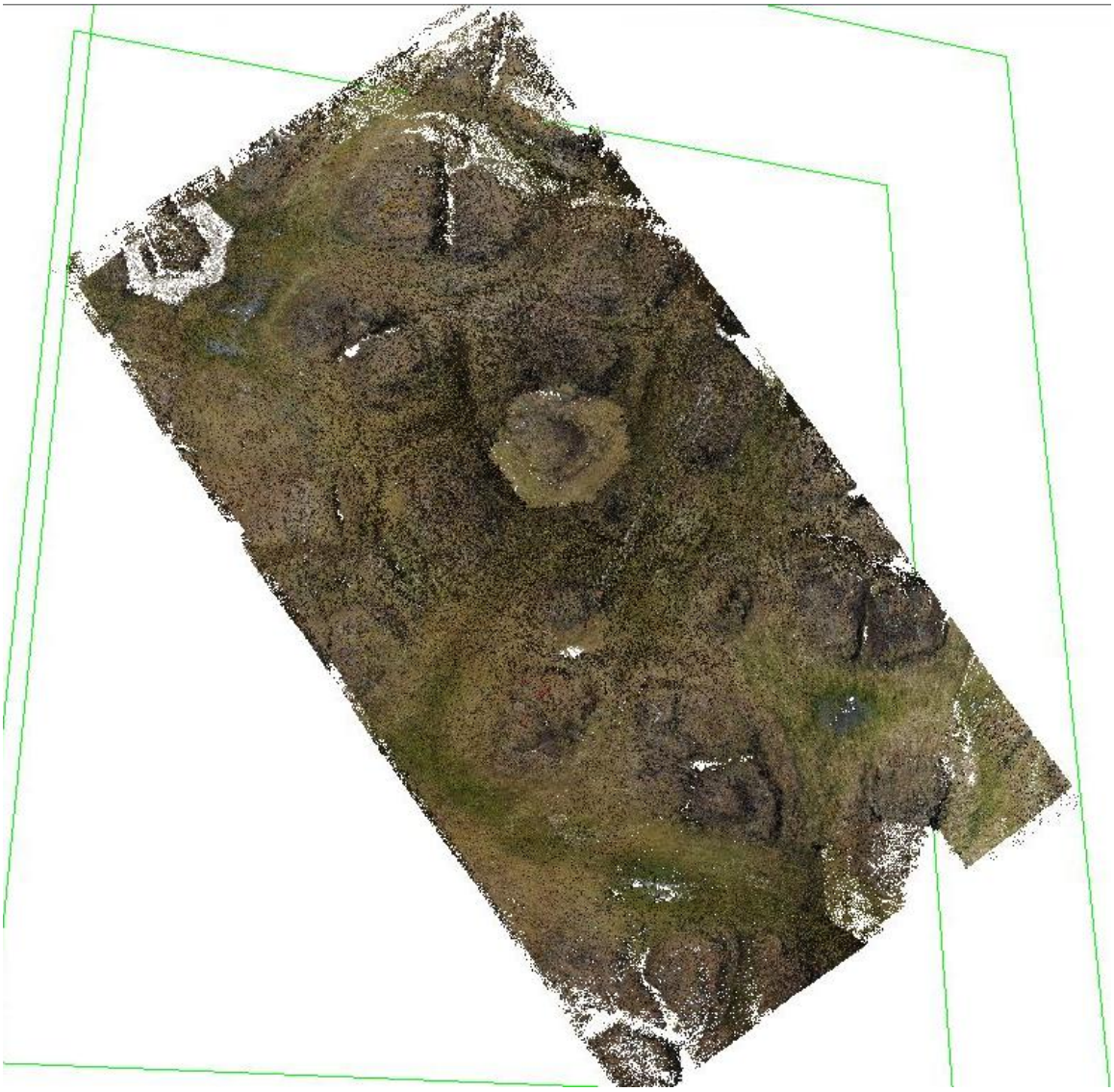

Figure 50. Terrestrial LIDAR point cloud from summer 2011 collection, ~2 km south of the CRREL sites. Points are rendered by RGB value but not projected or classified.

In addition to providing a comparison dataset for the 2010 terrestrial LIDAR, the 2011 data also offers a unique opportunity for comparison with aerial LIDAR data. The 2011 terrestrial data was collected in an area as previously covered by a 2005 airborne LIDAR collection. This airborne data has already been processed into a DEM, with a resulting RMSE of ~4.3 cm (Figure 51, Tweedie 2005), which is roughly equivalent to the results achieved by terrestrial data in this study.

If airborne LIDAR could be just as accurate as terrestrial LIDAR in detecting microtopographical variations in the landscape at 10 × 10 cm scale, but without the streaking in the point cloud, then perhaps it is a better methodology for future monitoring of sites in this area. A comparison of the 2011 terrestrial data to the 2005 airborne data for the same study area could provide important insights into what is the most effective method and resolution for detecting changes in permafrost features on the landscape.

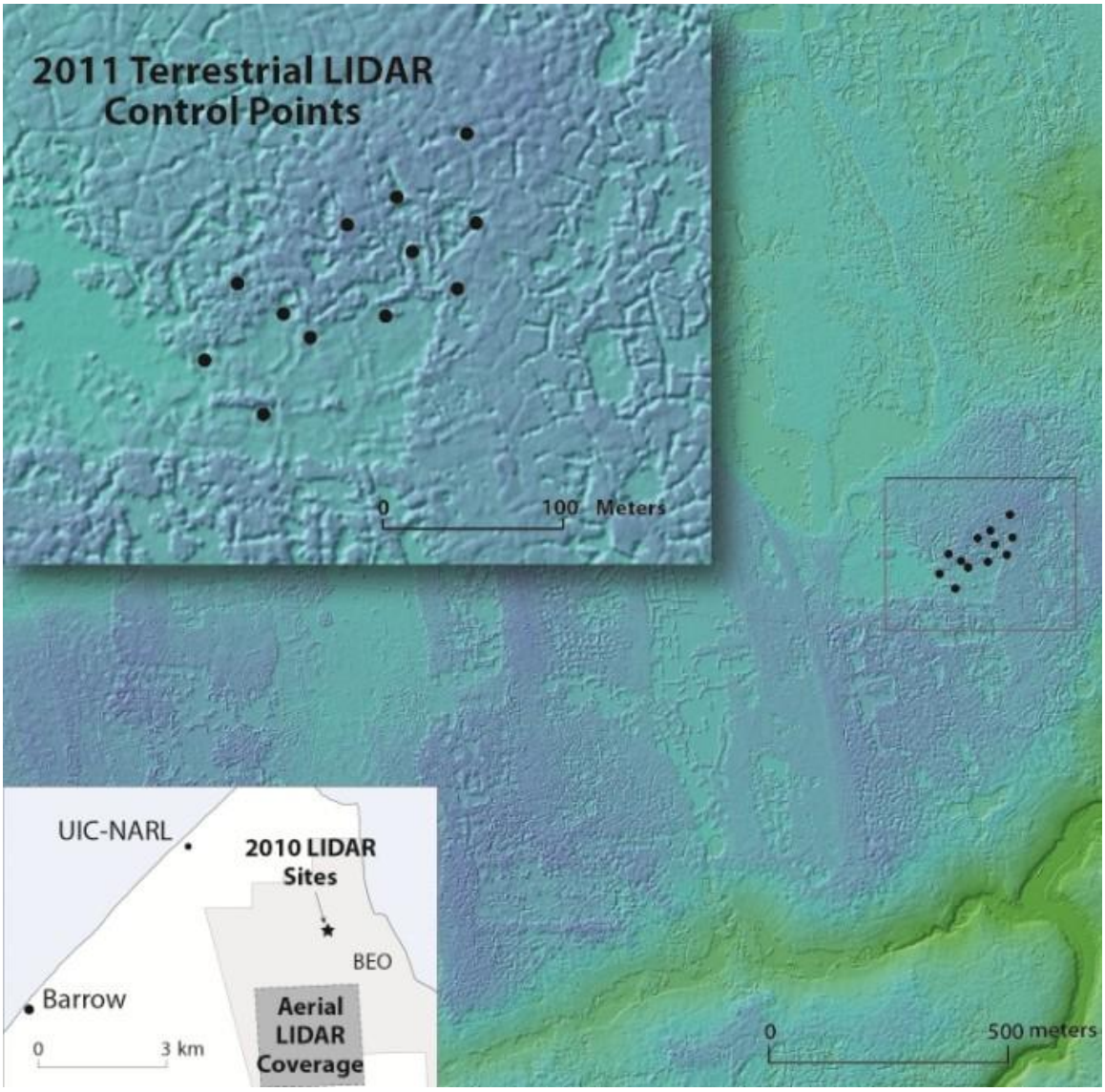

Figure 51. High-resolution DEM and hillshade generated from airborne LIDAR scans of an area ~2 km S-SW of the CRREL sites. Data was acquired by AeroMetric on October 4, 2005. The horizontal and vertical accuracies of the DEM are 0.30 m and 0.15 m, respectively. The small scale inset map shows the location of the aerial DEM coverage relative to the site of the 2010 terrestrial LIDAR acquisition (CRREL plots). The larger scale inset map shows the locations of the 2011 terrestrial LIDAR acquisition control points, as well as the landscape detail captured in the aerial LIDAR DEM. Data provided by NCAR/EOL under sponsorship of the National Science Foundation: http://data.eol.ucar.edu.

7.3 RADAR-based Initiatives

Another interesting investigation would be to compare the LIDAR-derived DEMs to those derived from RADAR data. RADAR-based DEMs also hold promise for detecting heave and subsidence in the cryosphere and are often compared to LIDAR DEMs in terms of their ability to achieve high-resolution (cm-scale) vertical accuracy (Short et al. 2011; Rykhus & Lu 2008). Effective evaluation of the accuracy of the RADAR-derived DEMs requires reference data "of accuracy at least an order of magnitude better than the system being tested" (Barber et al. 2008). Until the development of LIDAR DEMs, there were few products that were of high enough resolution to test the accuracy claims of the RADAR DEMs. A comparison of RADAR DEMs to high resolution LIDAR DEMs like those developed in this study could help to inform the feasibility of using satellite-based remote-sensing data in permafrost monitoring.

REFERENCES

ACIA (Arctic Climate Impact Assessment). 2004. *Impacts of a warming Arctic: Climate impact assessment*. Cambridge: Cambridge University Press.

Arnold, N.S., W.G. Rees, B.J. Devereux, and G.S. Amable. 2006. Evaluating the potential of high-resolution airborne LIDAR data in glaciology. *International Journal of Remote Sensing* 27, no. 6: 1233-1251.

Ascione, A, A. Cinque, E. Miccadei, F. Villani, and C. Berti. 2008. The plio-quaternary uplift of the Apenine chain: New data from the analysis of topography and river valleys in Central Italy. *Geomorphology* 102, no. 1: 105-18.

Barber, D. J. Mills, and S. Smith-Voysey. 2008. Geometric validation of a ground-based mobile laser scanning system. *ISPRS Journal of Photogrammetry & Remote Sensing* 63, no. 1: 128-141.

Besl, P.J. and N.D. McKay. 1992. A method for registration of 3-d shapes. *IEEE Transactions on Pattern Analysis and Machine Intelligence* 14, no. 2: 239-256.

Böhm, J. and N. Haala. 2005. Efficient integration of aerial and terrestrial laser data for virtual city modeling using lasermaps. Paper presented at ISPRS WG III/3, III/4, V/3 Workshop "Laser scanning 2005", Enschede, the Netherlands, September 12-14, 2005.

Bonnaffe, F., D. Jennette, and J. Andrews. 2007. A method for acquiring and processing ground-based LIDAR data in difficult-to-access outcrops for use in three-dimensional, virtual-reality models. *Geosphere* 3, no. 6: 501-510.

Briese, C., N. Pfeifer, and P. Dorninger. 2002. Application of the robust interpolation for DTM determination. Paper presented at ISPRS Commission III Symposium, Photogrammetric Computer Vision, Graz, Austria, September 9-13, 2002.

Brown, J. and P.L. Johnson. 1965. *Pedo-ecological investigations, Barrow, Alaska*. Hanover, New Hampshire: Corps of Engineers U.S. Army Cold Regions Research & Engineering Laboratory.

Brown, J., W. Rickard, and J. Przybyla. 1970. *USA CRREL study area Barrow, Alaska soil data, 1962-1966*. Hanover, New Hampshire: Corps of Engineers U.S. Army Cold Regions Research & Engineering Laboratory.

Brown, J., K.M. Hinkel, and F.E. Nelson. 2000. The circumpolar active layer monitoring (CALM) program: Research design and initial results. *Polar Geography* 24, no. 3: 166-258.

Buckley, A. 2010. Understanding curvature rasters. In *Imagery, Mapping*, ed. ESRI, 2013. ArcGIS Online: ESRI.

Burrough, P.A. and R.A. McDonnell. 1998. *Principles of geographical information systems*. New York: Oxford University Press Inc.

Burtch, R. 2002. LIDAR principles and applications. Paper presented at 2002 IMAGIN Conference, Traverse City, MI.

Dailey, S.W. 2008. An accuracy assessment of 3-dimensional measurements derived from LIDAR and pictometry data when compared with in situ survey measurements. Master of Science, University of South Carolina.

Engstrom, R., A. Hope, H. Kwon, D. Stow, and D. Zamoldchikov. 2005. Spatial distribution of near surface soil moisture and its relationship to microtopography in the Alaskan arctic coastal plain. *Nordic Hydrology* 36, no. 3: 219-234.

Evans, J., A. Hudak, R. Faux, and A.M.S. Smith. 2009. Discrete return LIDAR in natural resources: Recommendations for project planning, data processing, and deliverables. *Remote Sensing* 1, no. 4: 776-94.

Evans, J. Compound topographic index Apr 22 2004. ESRI, ArcGIS Online. http://arcscripts.esri.com/details.asp?dbid=11863 (accessed April 9, 2013).

Fowler, A. and V. Kadatskiy. 2012. Accuracy and error assessment of terrestrial, mobile, and airborne LIDAR. Paper presented at Specialty Conference - "Ground to Cloud (R)Evolution - Emerging Technologies Supporting Geospatial Application", Tampa, FL, Oct. 29 – Nov. 1 2012.

Gitelson, A, Y. Kaufman, R. Stark, and D. Rundquist. 2002. Novel algorithms for remote estimation of vegetation fraction. *Remote Sensing of Environment* 80, no. 1: 76-87.

Grohmann, C.H., M.J. Smith, and C. Riccomini. 2011. Multiscale analysis of topographic surface roughness in the Midland Valley, Scotland. *IEEE Transactions on Geoscience and Remote Sensing* 49, no. 4: 1200-13.

Haugerud, R.A. and D.J. Harding. 2001. Some algorithms for virtual deforestation (VDF) of LIDAR topographic survey data. *International Archives of Photogrammetry and Remote Sensing* XXXIV, no. 3: 211-16.

Harris, S.A., H.M. French, J.A. Heginbottom, G.H. Johnston, B. Ladanyi, D.C. Sego, and R.O. van Everdingen. 1988. *Glossary of permafrost and related ground-ice terms*. Ottawa, Ontario, Canada: National Research Council of Canada.

Hassol, S.J. 2004. *Impacts of a warming arctic*. Cambridge, UK: Arctic Council.

Hinkel, K.M. and F.E. Nelson. 2003. Spatial and temporal patterns of active layer thickness at circumpolar active layer monitoring (CALM) sites in northern Alaska, 1995-2000. *Journal of Geophysical Research* 108, no. 8168: 1-13.

Hinkel, K.M. and J.K. Hurd. 2006. "Permafrost destabilization and thermokarst following snow fence installation, Barrow, Alaska, U.S.A." *Arctic, Antarctic, and Alpine Research* 38, no. 4: 530-539.

Hofton, M.A., L.E. Rocchio, J.B. Blair, and R. Dubayah. 2002. Validation of vegetation canopy LIDAR sub-canopy topography measurements for a dense tropical forest. *Journal of Geodynamics* 34, no. 3-4: 491-502.

Hopkinson, C., L. Chasmer, C. Young-Pow, and P. Treitz. 2004. Assessing forest metrics with a ground-based scanning LIDAR. *Canadian Journal of Forest Research* 34, no. 3: 573-83.

Hunt, E.R., P.C. Doraiswamy, J.E. McMurtrey, C.S.T. Daughtry, E. Perry, and B. Akhmedov. 2013. A visible band index for remote sensing leaf chlorophyll content at the canopy scale. *International Journal of Applied Earth Observation and Geoinformation* 21: 103-12.

Hussey, K.M. and R.W. Michelson. 1966. Tundra relief features near point Barrow, Alaska. *Arctic* 19, no. 2: 162-184.

Isenburg, M. 2011. Lasclassify - finding ground points for bare-earth extraction. In *LAStools - efficient tools for LiDAR processing*, ed. Martin Isenburg, 2013. Google Groups: Google.

Lefsky, M., W.B. Cohen, and G.G. Parker. 2002. LIDAR remote sensing for ecosystem studies. *BioScience* 52, no. 1: 19-30.

Little, J.. 2006. Frost heave and thaw settlement in tundra environments: application of differential global positioning system technology. Master of Science. University of Delaware.

Little, J.D., H. Sandall, M.T. Walegur, and F.E. Nelson. 2003. Application of differential global positioning systems to monitor frost heave and thaw settlement in tundra environments. *Permafrost and Periglacial Processes* 14, no. 4: 349-357.

Louhaichi, M., M.M. Borman, and D.E. Johnson. 2001. Spatially located platform and aerial photography for documentation of grazing impacts on wheat. *Geocarto International* 16, no. 1: 65-70.

Melton, M.A. 1965. The geomorphic and paleoclimatic significance of alluvial deposits in Southern Arizona. *The Journal of Geology* 73, no. 1: 1-38.

Motohka, T., K.N. Nasahara, H. Oguma, and S. Tsuchida. 2010. Applicability of green-red vegetation index for remote sensing of vegetation phenology. *Remote Sensing* 2, no. 10: 2369-87.

Muller, S.W. 1947. Permafrost, or, permanently frozen ground and related engineering problems. Ann Arbor, Michigan: J.W. Edwards, Inc.

Nelson, F.E., S.I. Outcalt, J. Brown, N.I. Shiklomanov, and K.M. Hinkel. 1998. Spatial and temporal attributes of the active layer thickness record, Barrow, Alaska, U.S.A. In *PERMAFROST - Seventh International Conference*: 797-802. Yellowknife (Canada).

Norton, D.W. "Down through time: Editor's introduction" *Fifty More Years Below Zero*, Arctic Institute of North America, 2001, pp. 1-6.

Olivas, P.C., S.F. Oberbauer, C.Tweedie, W. Oechel, D. Lin, and A. Kuchy. 2011. Effects of fine-scale topography on CO_2 flux components of Alaskan coastal plain tundra: Response to contrasting growing seasons. *Arctic, Antarctic, and Alpine Research* 43, no. 2: 256-266.

Peterson, R.A. 1999. Differential frost heave manifest as patterned ground - modeling, laboratory and field studies. Doctor of Philosophy, University of Colorado.

Pike, R. and S. Wilson. 1971. Elevation-relief ration, hypsometric integral, and geomorphic area-altitude analysis. *Geological Society of America Bulletin* 82, no. 4: 1079-84.

Ponti, M.P. 2012. Segmentation of low-cost remote sensing images combining vegetation indices and mean-shift. *IEEE Geoscience and Remote Sensing Letters* 10, no. 1: 67-70.

Rosser, N.J., D.N. Petley, M. Lim, S.A. Dunning, and R.J. Allison. 2005. Terrestrial laser scanning for monitoring the process of hard rock coastal cliff erosion. *Quarterly Journal of Engineering Geology and Hydrogeology* 38: 363-75.

Rykhus, R.P., and Z. Lu. 2008. INSAR detects possible thaw settlement in the Alaskan arctic coastal plain. *Canadian Journal of Remote Sensing* 34, no. 2: 100-12.

Riley, S.J., S.D. DeGloria, and R. Elliot. 1999. A terrain ruggedness index that quantifies topographic heterogeneity *Intermountain Journal of Sciences* 5, no. 1-4: 23-27.

Romanovsky, V.E. and T.E. Osterkamp. 1997. Thawing of the active layer on the coastal plain of the Alaskan arctic. *Permafrost and Periglacial Processes* 8, no. 1: 1-22.

Ruszkiczay-Rüdiger, Z., L. Fodor, E. Horváth, and T. Telbisz. 2009. Discrimination of fluvial, eolian and neotectonic features in a low hilly landscape: A DEM-based morphotectonic analysis in the Central Pannonian Basin, Hungary. *Geomorphology* 104, no. 3: 203-17.

Schuur, E.A.G. and B. Abbott. 2011. Climate change: High risk of permafrost thaw. *Nature* 480, no. 7375: 32-33.

Sellmann, P.V., J. Brown, R. I. Lewellen, H. McKim, and C. Merry. 1975. *The classification and geomorphic implications of thaw lakes on the arctic coastal plain, Alaska*. Hanover, New Hampshire: Cold Regions Research and Engineering Laboratory.

Shiklomanov, N.I., D.A. Streletskiy, F.E. Nelson, R.D. Hollister, V.E. Romanovsky, C.E. Tweedie, J.G. Bockheim, and J. Brown. 2010. Decadal variations of active-layer thickness in moisture-controlled landscapes, Barrow, Alaska. *Journal of Geophysical Research* 115, no. G00I04: 1-14.

Shiklomanov, N.I., F.E. Nelson, D.A. Streletskiy and A.E. Klene. 2011. Long-term active-layer trends: 20 years of circumpolar active layer monitoring (CALM) observations. *American Geophysical Union, Fall Meeting* December: abstract #GC511-04.

Short, N., B. Brisco, N. Couture, W. Pollard, K. Murnaghan, and P. Budkewitsch. 2011. A comparison of TerraSAR-X, RADARSAT-2 and ALOS-PALSAR interferometry for monitoring permafrost environments, case study from Herschel Island, Canada. *Remote Sensing of Environment* 115, no. 12: 3491-506.

Shur. Y.L. 1988. The upper horizon of permafrost soils. In *Fifth International Conference on Permafrost* ed. Kaare Senneset, 1:867-71. Trondheirn, Norway: Tapir Publishers.

Song, J., S. Han, K. Yu, and Y. Kim. 2002. Assessing the possibility of land-cover classification using LIDAR intensity data. *International Archives of Photogrammetry and Remote Sensing* 34, no. 3: 259-62.

Streletskiy, D.A. 2010. Spatial and temporal variability of the active-layer thickness at regional and global scales. Doctor of Philosophy, University of Delaware.

Sturm, M., D. Scott, and S.A. Vargas. 2011. Lidar (DEM) Barrow experimental (be) grid Barrow, Alaska. Dataset available from: Advanced Cooperative Arctic Data & Information Service (ACADIS).

Tweedie, C. 2005. Begrid (digital elevation model). Dataset available from: NCAR Earth Observing Laboratory (EOL).

---. 2010. Brwpeninsulalandcover2002. Dataset available from: NCAR Earth Observing Laborator (EOL).

Viereck, L.A., C.T. Dyrness, A.R. Batten, and K.J. Wenzlick. 1992. *The Alaska vegetation classification*. Portland, OR Forest Service, Pacific Northwest Research Station.

Wahr, J., L. Liu, and T. Zhang. 2008. InSAR measurements of ground surface deformation due to thaw settlement and frost heave over permafrost on the North Slope of Alaska. *American Geophysical Union, Fall Meeting* December: B2.

Wang, C. and N.F. Glenn. 2009. Integrating LIDAR intensity and elevation data for terrain characterization in a forested area. *IEEE Geoscience and Remote Sensing Letters* 6, no. 3: 463-66.

Washburn, A.L. 1973. *Periglacial processes and environments*. New York: St. Martin's Press.

Weiss, A.D. 2001. Topographic position and landforms analysis: poster presentation. *ESRI User Conference*. San Diego, CA: The Nature Conservancy.

Vosselmar, G. and H. Maas. 2010. *Airborne and terrestrial laser scanning*. Dunbeath: Whittles Publishing.

Zhu, M. 2006. Modeling and simulation of frost heave in frost-susceptible soils. Doctor of Philosophy, The University of Michigan.